


Doctoral Dissertation
Doctoral Program in Physics (31.th cycle)

Microbridge resonators with embedded nanochannels for attogram resolution in liquid

Davide Scaiola

* * * * * *

Supervisor
Prof. Carlo Ricciardi, Supervisor

Doctoral Examination Committee:
Prof. Thomas Burg, Referee, Max Plank Institute, Germany
Prof. Massimo De Vittorio, Referee, Università del Salento, Italy
Prof. Paolo Olivero, Università di Torino, Italy
Prof. Sergio Ferrero, Politecnico di Torino, Italy
Prof. Fabrizio Giorgis, Politecnico di Torino, Italy

Politecnico di Torino
July 05, 2019

I hereby declare that, the contents and organization of this dissertation constitute my own original work and does not compromise in any way the rights of third parties, including those relating to the security of personal data.

. . . . . .

Davide Scaiola

Turin, July 05, 2019

Summary

The purpose of this thesis is to investigate the realization of microbridge resonators with embedded nanochannels used as mass sensors with attogram resolution in liquid. The attogram resolution in liquid has been taken as target because the aim of this work is to fabricate a sensor able to perform real-time detection of buoyant nanoparticles (NPs).
Natural or engineered nanoparticles, with diameters below 100 nm and so with mass of the order of some femtogram ($1\,\mathrm{fg} = 1 \times 10^{-15}\,\mathrm{g}$), are extremely used in many fields, such as medicine [1], energy [2], environment [3], cosmetics [4] and food [5]. A tool for real-time and accurate identification of cell-secreted nano-vesicles (such as exosomes) in liquid media would for sure open new perspectives in comprehension and treatments of cancer and neurodegenerative diseases. Similarly, an instrument able to routinely identify and quantify the number and particle size distribution of objects in the 1 nm–100 nm range would be essential to accurately monitor the degradation and fate of nanoparticles after their use, a topic that every day is growing in interest, since evidence of toxicology of many nano-objects ("nanotoxicology") [6].
Determination of nanoparticles in liquid is, in fact, a major challenge for the scientific community, because it presents extremely serious analytical difficulties for definition of identity (whether a certain substance is in the sample, i.e. size and chemical composition), as well as quantification (how much of the substance is in the sample, i.e. mass). Currently used techniques such as Transmission Electron Microscope (TEM) [7], Dynamic Light Scattering (DLS) [8] and Inductively Coupled Plasma Mass Spectroscopy (ICP-MS) [9] pose severe limitations in sample preparation, cost and data interpretation.

The here proposed sensing platform is based on a resonating microbeam on which a nanochannel is integrated, such kind of sensor is called suspended nanochannel resonator (SNR) [10]. When a NP is passing through the vibrating nanochannel it will produce a variation of the effective mass of the device, changing its resonating frequency [11]. Thanks to this approach (proposed in [12] for suspended microchannel resonator - SMR), it is possible to circumvent the main drawback of cantilever-based mass sensors that consists of the complexity to operate directly

in liquid phase, where the viscous friction decreases the frequency and the quality factor, making the sensor unstable and poorly sensitive.

Chapter number one reports the state of the art of SMR/SNR devices, chapter number two explains the working principles and the theory of the mechanical resonators as mass sensors and the third one deals with the design of the devices in order to reach the target sensitivity. In this thesis three different devices are presented: nanoslit, in which the only nanometric dimension is the height of the hollow channel; nanochannel, in which both height and width are at the nanoscale; and the so called "two-step" nanoslit in which the height of the hollow channel is not constant along the extension of the device. The fabrication, done in the Centre of Micro and Nanotechnologies at the École polytechnique fédérale de Lausanne (CMi@EPFL), is deeply described in the fourth chapter. The process flow was based on a sacrificial layer approach that allows to easily tailor the dimensions of the channel by changing the thickness of the sacrificial layer or its patterning during the lithographic step. Then the fabrication process was applicable to the three types of devices designed only carrying punctual modification at some step. With this approach, devices with channel dimension of 50 nm was successfully fabricated. In the fifth chapter it is illustrated the experimental setup used to get the result analyzed in the sixth chapter. The characterization activity has been focused on the nanoslit devices with the mass sensitivity of the resonators assessed to be up to 256.4 ag/Hz. Finally, in the seventh chapter a resume of the work is disclosed as conclusion of the thesis. To the best of our knowledge, the devices presented here are the first SNR reported with a channel height as low as 50 nm that are fabricated with a top-down approach.

Acknowledgements

Firstly, I want to thank my advisor Prof. Carlo Ricciardi for the continuous support of my Ph.D. study and related research, for his patience, motivation, and knowledge. His guidance helped me in all the time of research and writing of this thesis.

Besides my advisor, I would like to thank my thesis referees Prof. Thomas Burg and Prof. Massimo De Vittorio for their insightful comments.

My sincere thank also go to Prof. Philippe Renaud who provided me an opportunity to join to his research team as visiting Ph.D. and who gave access to the laboratory and research facilities of the EPFL. Without him precious support it would not be possible to conduct this research. My acknowledgment goes to all the LMIS4@EPFL team and especially to Prof. Arnaud Bertsch and Prof. Harald Van Lintel, Stefano S. G. Varricchio, Jonathan Cottet and Benoît Desbiolles for their support and useful discussions for the fabrication process of my devices.
My recognition goes also to all the CMi@EPFL staff for the technical support received in the fabrication part.

I want also to thank all the NEMS@EPFL group for stimulating consultations and the help they gave me for the characterization set-up, especially Prof. Guillermo Villanueva, Annalisa De Pastina, Tom Larsen and Damien Maillard.

The periods and the research done at EPFL were partially supported by the Compagnia di San Paolo with the Project for internationalization of research.

I thank my fellow labmates from NaMeS@PoliTO group for the stimulating discussions, for the infinite afternoons in which we were working together and for all the fun we have had in the last years... Thanks to Stefano, Roberta, Daniele, Cecilia, Gianluca and Vittorio.

Also, I thank all the other friends from DISAT and Politecnico di Torino that helped me during these years, in the lab, in the office, in the cafè: Erik, Ugo,

Alessandro, Federico, Gianluca, Davide... and all the others!

Last but not least, I would like to thank my girlfriend Federica, my family and all my friends for putting up with me during all these years.

Contents

List of Tables

List of Figures

Chapter 1

Introduction

1.1 Suspended Micro- and Nanochannel resonators for bio-sensing

In the last decades micro- and nano-mechanical resonators, such as cantilevers or clamped-clamped beams, have been adopted as mass sensors in many fields [13] like life-science, biotechnology, chemistry, biology [14], drug discovery [15], food engineering [16], and so on. The reasons of this spreading are their intrinsic sensing capability of very small masses and the affordable costs in terms of fabrication. These peculiarities fit very well with the requirements needed for the biomedical analysis and biochemical detection [17–19]. In fact, thanks to their high sensitivity micro and nano sized resonators have been used to detect, for example, viruses [20], individual cells [21], proteins [22], DNA [23] and single molecules [24]. Some research groups pushed the mass resolution limit even lower and succeeded in detecting nanoparticles [25] or in reaching the yoctogram resolution [26] ($1\,\mathrm{yg} = 1 \times 10^{-24}\,\mathrm{g}$), which corresponds to the mass of one proton.

It has to be noticed that in each case reported above, the detection has been done in a vacuum chamber, while most of the biological and biochemical essays have to be performed directly in a liquid solution. This because surrounding fluid has a huge detrimental effect on the performance of classical mechanical resonator and so usually a pumping system is activated during the characterization to overcome to this drawback. Furthermore, real time measurement on the kinetic of biological or chemical reactions, usually occurring liquid solutions, cannot be executed imposing a further limitation in the usage of mechanical resonator as mass sensor.

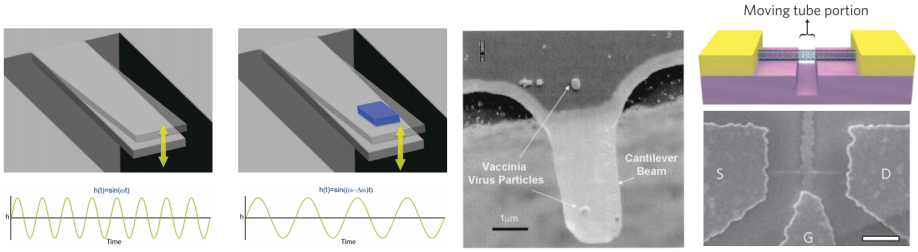

(a) (b) (c)

Figure 1.1: (a) Sketch of the working principle of a mechanical resonator used as mass sensor, the theory will be explained later in chapter 2. [27] (b) Scanning electron microscopy picture showing a cantilever beam with a single vaccinia virus particle. Work by Gupta et al. [18]. (c) Schematic and Scanning electron microscope image of a suspended carbon nanotube resonator. This device reached the yoctogram resolution. Work by Chaste et al. [26].

To bypass these problems the Manalis' research group had the idea to embedded a fluidic microchannel in a cantilever [12] and to operate it in vacuum, thus constraining the liquid inside the device and being able to flux it. They demonstrated that the quality factor of the resonator, and thus the maximum mass sensitivity achievable by the sensor, was not affected by the presence of the liquid inside the channel because the viscous damping was almost suppressed [28]. In this work, published by Burg et al. in 2003, the target probe was a biomolecule and the device consisted of a cantilever beam 300 µm long with an embedded microchannel of height 1.2 µm. First, they checked the mass resolution of the sensor flowing different fluids and evaluating the frequency shift due to the different densities obtaining a result of 9 pg/Hz. Then the inner channel was functionalized with avidin protein to obtain binding with biotinylated bovine serum albumin bBSA, the real-time measurement confirmed the ability of this sensor to weight biomolecules. The fabrication of these suspended microchannel resonator (SMR) was performed with a process flow based on sacrificial layer approach: the channel is modeled using a

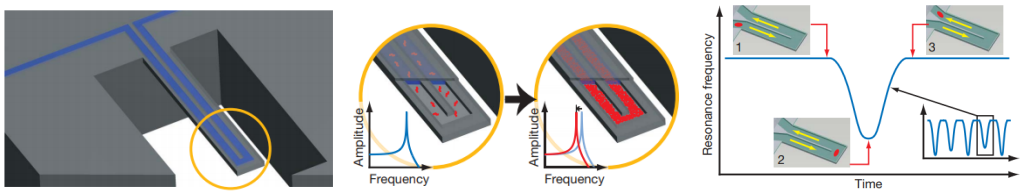

(a) (b) (c)

Figure 1.2: (a)-(c) Sketch of the working principle of the suspended microchannel resonator developed by Burg et al. in 2007 [29].

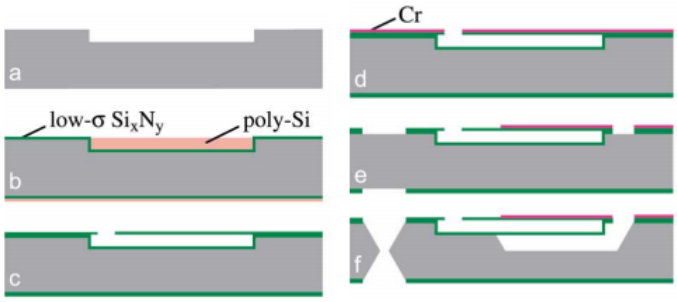

(a) (b)

Figure 1.3: (a)-(b) Sketch of fabrication process proposed by the Burg et al. in 2006 for SMR devices based on sacrificial layer approach [30].

polysilicon layer encapsulated between two layers of Silicon Nitride, then the sacrificial layer is removed proceeding with a wet etching based on potassium hydroxide, e.i. Fig. 1.3. In 2007 Burg et al. [29] showed nanoparticles characterization using a SMR based on a cantilever 200 µm × 33 µm × 7 µm (length x width x thickness) containing a 3 µm × 8 µm (height x width) channel, sketched in Figure 1.2. The fabrication process is innovative compared to the previous publications [12, 30] and is based on the creation of buried channels in silicon-on-insulator (SOI) wafers, followed by wafer thinning, dry etching and bonding to form suspended microchannels. Basically, the "silicon direct-bonded wafer technology" process works by first etching into an SOI wafer, without reaching the buried oxide. Then buried cavities are created exploiting silicon direct bonding. The bonded top wafer is later thinned down (or etched back) to make the channel lid. For very thin resonators, the top wafer is also an SOI to get the thickness control. After making the buried cavities, the resonator is etched out from top and bottom and packaged [31]. This process draws inspiration from the works published by Corman et al. [32, 33], reported in figure 1.4. Gold nanoparticles (100 nm), with a mean weight of 10 fg, produced a frequency shift of 36 mHz, so a mass sensitivity of 280 fg/Hz could be computed for that device. This step was relevant because the determination of nanoparticles (NPs) in liquid is a major challenge for the scientific community, because it presents extremely serious analytical difficulties for definition of identity (whether a certain substance is in the sample, i.e. size and chemical composition), as well as quantification (how much of the substance is in the sample, i.e. mass). The usual performed techniques such as Transmission Electron Microscope (TEM) [7], Dynamic Light Scattering (DLS) [8] and Inductively Coupled Plasma Mass Spectroscopy (ICP-MS) pose severe limitations in sample preparation, cost and data interpretation, so being able to detect them in liquid in real-time opened a new way for the characterization. The challenge thus became to have a sensitivity high enough to sense also smaller nanoparticles, one by one.

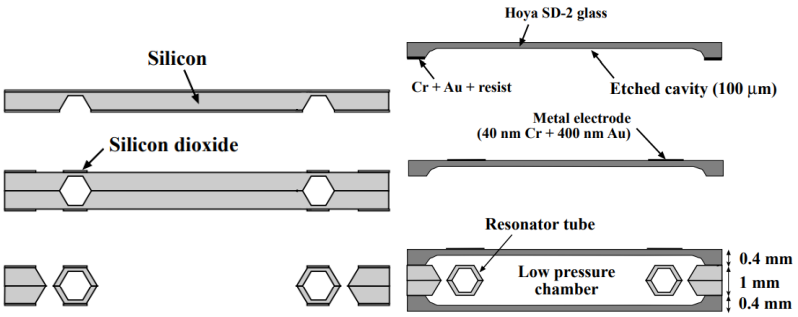

(a) (b)

Figure 1.4: (a)-(b) Sketch of fabrication process proposed by the Corman et al. in 2000 based on Silicon direct bonding [32].

The same group in 2010 [10] was able to improve their performance in terms of sensitivity exploiting the same idea of the previous publications but scaling down the dimensions of the device. In fact, the cantilever was of the following dimensions 50 µm × 10 µm × 1.3 µm (length x width x thickness) with a channel at the nanometric scale (height 700 nm and 2 µm). With this first implementation of a Suspended nanochannel resonator (SNR) a mass sensitivity of 1.12 fg/Hz was reached.

On the same year another research group headed by Craighead reached the same goal of fabricating a SNR [34] with a channel of the height of only 70 nm, reported in Fig. 1.5. They were able to determine a mass sensitivity of 9.71 ag/Hz.
To fabricate their devices this group still used a process flow based on sacrificial layer approach, although they changed the reagent for the releasing of the silicon: from a wet etching with KOH to gas etchant, the XeF_2. The wet etching, in fact, is no more suitable when the dimensions reach the nanometric scale because stiction can arise and the time necessary for the etching process considerably increase.

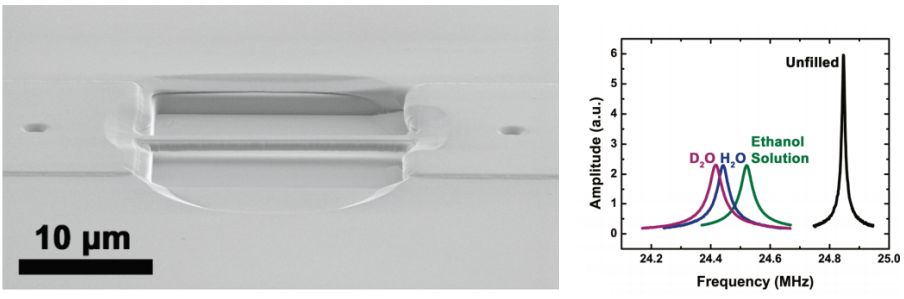

(a) (b)

Figure 1.5: (a) Scanning electon microscope image of the SNR by [34]. (b) Resonance frequency of the device, filled by liquids with different density

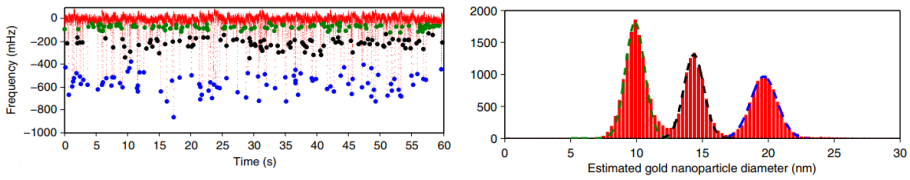

(a) (b)

Figure 1.6: (a) Frequency shift produced by a mixture of nanoparticles with size of 10,15 and 20 nm. (b) Estimated diameter histogram (calculated under the assumption that particles were perfect spheres of density 19.3 g/cm^3. Particle peaks are the ones reported in (a). [35]

In 2014 the Manalis' research group improved another time the results regarding the sensing of nanoparticles with a SNR [35]. In this work they were able to reach a resolution of 62.5 ag/Hz using a cantilever 22.5 µm × 7.5 µm × 1 µm (length x width x height) with a channel 400 nm x 1 µm (height x width). Gold nanoparticles of different size (10,15 and 20 nm) were suspended in ultrapure deionized water and flown in the fluidic system. Measuring in real time the resonance frequency of the resonator was possible to see a decreasing peak each time that one (or more) nanoparticle was passing through the channel, see Fig. 1.6a. In this way, starting from the mass measurement, they were able to extrapolate a distribution of the estimated diameter of the gold nanoparticles, reported in Fig. 1.6b.

The sacrificial layer approach [12, 30, 34, 36–39] and the "silicon direct-bonded wafer technology" [10, 29, 31, 35, 40] are the most used techniques by the scientific community to fabricate SMR and SNR, but they are not the only ones that have been proposed: in 2016 a suggestive self-assembly process has been developed [41]. The process, reported in figure 1.7a, is based on the silicon-on-nothing (SON) technique [42] and consist mainly in three steps: self-assembled cavity formation (Deep Reactive Ion etching of pores followed by a Surface mitigation), cavity internal oxidation, and device release via surface micromachining; in this way they achieved to fabricate channel thick 120 nm. The best performance obtained in this work correspond to a sensitivity of 48.92 ag/Hz get by a cantilever device of dimensions 18 µm × 16.5 µm × 2 µm having a resonance frequency of 5.7876 MHz and a quality factor of 6960. Starting from the Allan deviation, it has been calculated a theoretical resolution of 0.19 ag, reaching the sub-attogram scale.

Another fabrication process, for this family of devices, has been proposed in 2019 [43] and consists in an etching of monolithic glass using a femtosecond laser micromachining technique [44]. In this work a theoretical mass sensitivity of 11.67 pg/Hz has been achieved with a clamped-clamped beam of dimensions 500 µm × 75 µm x 30 µm (length x width x height). There are some limitations for the minimum achievable dimensions of the channels (and so of the devices) and so it has been used only for the fabrication of suspended microchannel resonators.

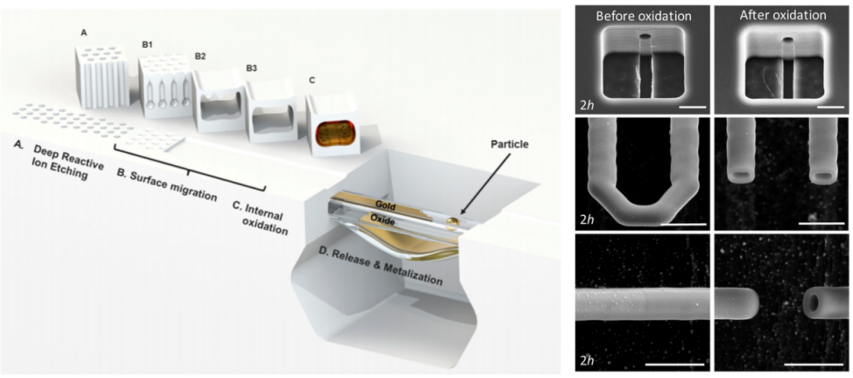

(a) (b)

Figure 1.7: (a) Key fabrication steps and application concept for SNR fabricated with self-assembly approach. (b) Scanning electron microscopy pictures around a port before and after the thermal oxidation (top), before and after a focused ion beam milling of a cantilever device (middle) and of a clamped-clamped beam device (bottom). [41]. All scale bars are 5 µm.

A sketch of the fabrication process and pictures of fabricated devices are reported in Fig. 1.8.

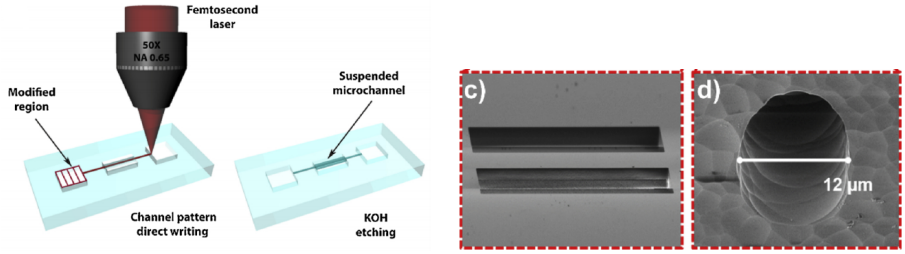

(a) (b)

Figure 1.8: (a) Sketch of fabrication process based on femtosecond laser milling for SMR. (b) SEM picture details of the released SMR c) and of the embedded microchannel d) [43]

The work presented in this thesis follows the path traced to reach the attogram (or lower) resolution in liquid, the limit to detect a single nanoparticle: scale down the dimensions of the channel to the nanometric scale using a process based on the sacrificial layer approach.

In Table 1.1 are reported some examples of SMR/SNR devices present in literature with the dimensions of the devices, the channel smallest dimension and the respective sensitivities.

Reference	Dimensions (l x w x t) µm	Channel c.d.	Mass sensitivity
Burg2003 [12]	$300 \times 100 \times 3$	1.2 µm	9 pg/Hz
Burg2007 [29]	$200 \times 33 \times 7$	3 µm	280 fg/Hz
Lee2010 [10]	$50 \times 10 \times 1.3$	700 nm	1.12 fg/Hz
Barton2010 [34]	$20 \times 2.5 \times 0.700$	70 nm	62.5 ag/Hz
Lee2011 [40]	$210 \times 28.5 \times 12$	8 µm	184.5 fg/Hz
Khan2011 [36]	$200 \times 5 \times 5$	4 µm	441.3 fg/Hz
Olcum2013 [35]	$22.5 \times 7.5 \times 1$	400 nm	62.5 ag/Hz
Vidal-Álvarez2016 [37]	$15 \times 1.47 \times 2.145$	470 nm	25 ag/Hz
Thundat2016 [41]	$18 \times 16.5 \times 2$	120 nm	48.92 ag/Hz
Marquez2017 [38]	$1300 \times 20 \times 6$	1 µm	135.5 fg/Hz
DePastina2018 [39]	$250 \times 30 \times 8$	5 µm	890 fg/Hz
Calmo2019 [43]	$500 \times 75 \times 30$	10 µm	11.67 pg/Hz

Table 1.1: Literature examples (ordered by year) of SMR/SNR and associated mass sensing capabilities. "Channel c.d." stays for the critical (minimum) dimension of the channel.

Chapter 2

Theory and working principles

2.1 Euler-Bernoulli Beam Theory

The model that describes the motion of a bending beam is called "Euler-Bernoulli beam theory", from the names of the two mathematicians that finalized it in the the eighteenth century. The eigenmode problem described in this model is one of the prominent cases that can be solved exactly, under some assumptions. First, the beam has to be slender (L/h > 10) (see Fig 2.1 then the rotational inertia and the shear deformation must be negligible. Assuming a linear elastic material and small deflections u(x,t), the equation of motion of a thin beam described by the model is [11, 45]:

$$\rho A \frac{\partial^2 u(x,t)}{\partial t^2} + EI_y \frac{\partial^4 u(x,t)}{\partial x^4} = 0, \tag{2.1}$$

where ρ is the mass density, A the cross-sectional area, E is the Young's modulus and I_y is the geometric moment of inertia. To solve this differential equation a superposition of normal modes can be introduced, one position dependent and one time-dependent, thus exploiting the separation of variables:

$$u(x,t) = \sum_{n=1}^{\infty} U_n(x) cos(\omega t), \tag{2.2}$$

where ω is the angular frequency of motion and n indicates the modal number. The angular frequency has unit of measurement radians per second, in this thesis the frequency will be normally reported as ordinary frequency, measured in Hertz. The relation between the two is the following:

$$\omega = 2\pi f. \tag{2.3}$$

The displacement function of the beam $U_n(x)$ can be formulated as:

$$U_n(x) = a_n cos\beta_n x + b_n sin\beta_n x + c_n cosh\beta_n x + d_n sinh\beta_n x \tag{2.4}$$

in which β_n is the wavenumber. The function can be divided in two parts: the first two terms describing the standing wave in the beam center, while the last two (the hyperbolic ones) representing the influence of the clamping. Looking at the equation 2.4 is easy to understand that the beam will vibrate only in certain vibrational modes, each with a distinct spatial shape, identified with the correspondent wavenumber β_n.

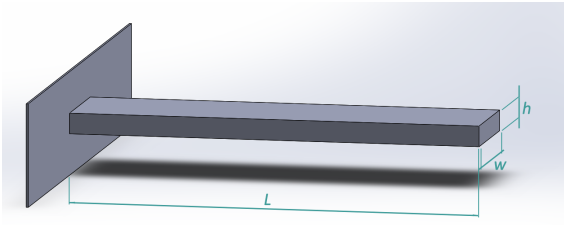

Figure 2.1: Schematic drawing of a single-clamped beam with quotes

Inserting the superposition of normal modes used to describe $U(x,t)$ (Eq. 2.2) into the Euler-Bernoulli model (Eq. 2.1), we can write the last equation as:

$$-\rho A\omega^2 u(x,t) + EI_y\beta_n^4 u(x,t) = 0. \tag{2.5}$$

The above equation 2.5 represent the dispersion relationship and so the eigenfrequency Ω can be obtained as function of the wavenumber β_n:

$$\Omega = \omega = \beta_n^2\sqrt{\frac{EI_y}{\rho A}}. \tag{2.6}$$

Now, to fully describe the motion of a vibrating beam, the wavenumber specific of each eigenmode has to be found. This is done deriving the unknown coefficients a_n, b_n, c_n, d_n in the Eq. 2.4 via the specific boundary conditions of the beam.

In my thesis I will discuss about the clamped-clamped beam, or bridge, that is a beam with both ends fixed. The boundary conditions are hence described by:

$$U_n(0) = U_n(L) = \frac{\partial}{\partial x}U_n(0) = \frac{\partial}{\partial x}U_n(L) = 0. \tag{2.7}$$

Writing down the Eq. 2.4 for each of these four boundary conditions, a system of fourth order is built that can be written as:

$$\begin{bmatrix} 1 & 0 & 1 & 0 \\ 0 & 1 & 0 & 1 \\ sin(\beta_n L) & -cos(\beta_n L) & sinh(\beta_n L) & cosh(\beta_n L) \\ cos(\beta_n L) & +sin(\beta_n L) & cosh(\beta_n L) & sinh(\beta_n L) \end{bmatrix} \begin{Bmatrix} a \\ b \\ c \\ d \end{Bmatrix} = \begin{Bmatrix} 0 \\ 0 \\ 0 \\ 0 \end{Bmatrix}. \tag{2.8}$$

Posing the determinant zero, we get the frequency equation:

$$cos(\beta_n L)cosh(\beta_n L) - 1 = 0. \tag{2.9}$$

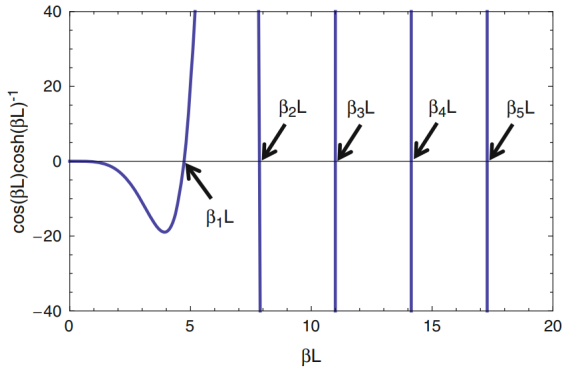

Figure 2.2: Plot of the solutions of the frequency equation (2.9) for a bridge, courtesy of [11]

The solutions for $n = 1,2,3, n > 3$ are $\lambda_n = \beta_n L = 4.7300, 7.8532, 10.9956, (2n + 1)\pi/2$, respectively. In Fig 2.2 is plotted the frequency equations (Eq. 2.9) for a bridge.

The unknown coefficients of the function describing the mode shape for a bridge (2.4) can be obtained using the boundary conditions (2.7). In fact, from the boundary conditions we get:

$$U_n(0) = 0 : a + c = 0 \rightarrow a = -c \tag{2.10}$$

$$\frac{\partial U_n(0)}{\partial x} = 0 : b + d = 0 \rightarrow b = -d \tag{2.11}$$

and so 2.4 becomes:

$$U_n(x) = a_n(cos\beta_n x - cosh\beta_n x) + b(sin\beta_n x - sinh\beta_n x). \tag{2.12}$$

Then, from the other ones we can obtain the ratio between the coefficient a_n and b_n:

$$\frac{\partial^2}{\partial x^2} U_n(L) = 0 : \frac{b_n}{a_n} = -\frac{cos\beta_n L - cosh\beta_n L}{sin\beta_n L - sinh\beta_n L}. \tag{2.13}$$

Finally Eq. 2.4 can be write as:

$$U_n(x) = a_n \left[cos\beta_n x - cosh\beta_n x - \frac{cos\beta_n L - cosh\beta_n}{sin\beta_n L - sinh\beta_n L}(sin\beta_n x - sinh\beta_n x) \right]. \tag{2.14}$$

The first four mode shapes of a cantilever are shown in Fig. 2.3.

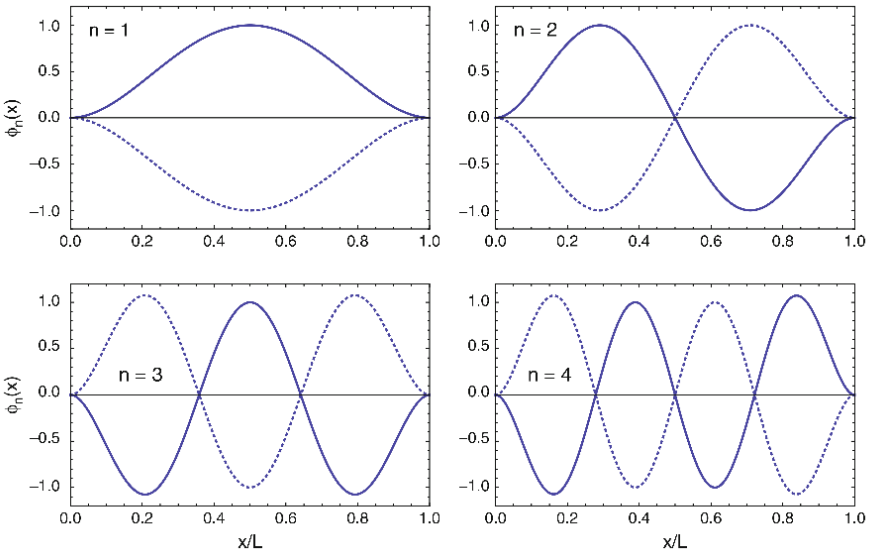

Figure 2.3: Schematics of the first four bending modes of a clamped-clamped beam seen from the side. The amplitude is in units of a_n and the position is in units of the length L, where 0 indicates one of the clamping of the beam. Courtesy of [11], from [46].

2.1.1 Effect of residual stress on frequency

Some residual stress is often present in the thin films typically used to fabricate the microresonator and its practical effect is to affect the resonance frequency. There are two types of stress: compressive or tensile, the first tends to decrease the resonance frequency while the tensile the opposite. Here we will consider the case of a tensile stress. Thus, to take it into account we have to add a term representing the tensile force $N = \sigma A$ in the Euler-Bernoulli model reported above 2.1, applying the Newton's third law we have:

$$\rho A \frac{\partial^2 u(x,t)}{\partial t^2} + EI_y \frac{\partial^4 u(x,t)}{\partial x^4} - N \frac{\partial^2 u(x,t)}{\partial x^2} = 0. \tag{2.15}$$

We can solve this equation using the same method used above 2.2 for the unstressed model [11] and using a sinusoidal mode shape with wavenumber β_n:

$$U_n(x) = U_{0,n} sin(\beta_n x). \tag{2.16}$$

As boundary conditions, for a simply supported doubly clamped beam, we can assume:

$$U_n(0) = U_n(L) = \frac{\partial^2}{\partial x^2} U_n(0) = \frac{\partial^2}{\partial x^2} U_n(L) = 0. \tag{2.17}$$

Substituting 2.16 in the superposition of modes previously used 2.2, the equation of motion (2.15) bring to a dispersion relation in which we can write the eigenfrequency Ω_n as function of the wavenumber β_n:

$$\Omega = \omega = \sqrt{\frac{\sigma}{\rho}\beta_n^2 + \frac{EI_y}{\rho A}\beta_n^4} = \beta_n^2 \sqrt{\frac{EI_y}{\rho A}} \sqrt{1 + \frac{\sigma A}{EI_y \beta_n^2}}. \tag{2.18}$$

The last equation 2.17 clearly shows that the eigenfrequency of a stressed beam is basically the unstressed one multiplied by a term which increases with stress.

2.2 Lumped-Element Model Resonator

The analytical model is very powerful, but very often the "Lumped-Element Model Resonator" is preferred due to its simplicity. This model simplifies the dynamics of an individual resonance mode to a linear harmonic oscillator. It can be considered valid as long as the resonator is driven in the linear regime, which is usually the case for appropriately small vibrational amplitudes. The system can hence be modeled with a one-dimensional resonator oscillator based on a linear zero mass spring, a linear damping element, and a mass, as reported in figure 2.4.

If we consider a periodic driving force $F(t) = F_0 cos(\omega t)$, the model is described by the following second order differential equation:

$$m\ddot{z} + c\dot{z} + kz = F(t), \tag{2.19}$$

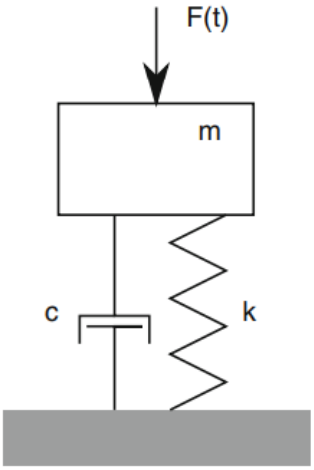

Figure 2.4: Damped one-dimensional oscillator with one degree of freedom. Courtesy of [11].

where m is the mass, k is the spring constant, and c is the damping coefficient.

As first case we can consider a non-driven lumped-element resonator with zero damping c. In this specific case the total energy of the system remains constant and the resonator turns into an harmonic oscillator with the oscillation motion described by $z(t) = z_0 cos(\omega t)$. Considering the fact that, during the motion, the total energy is fully transferred between kinetic and potential energy at the zero crossing and back at the reversal point. We can say, because there is no energy loss or creation in the system, that the two energies have to be equal

$$\frac{1}{2}m\ddot{z} = \frac{1}{2}kz^2. \tag{2.20}$$

From this equation (2.20) we can find the eigenfrequency Ω of the undamped free mechanical system, also called an "oscillator"

$$\Omega = \omega = \sqrt{\frac{k}{m}}. \tag{2.21}$$

It is commonly used to adopt this approach of "harmonic punctual oscillator" also with continuous structures.
In this case the above equation 2.21 is rewrite as:

$$\Omega_n = \sqrt{\frac{k_{eff,n}}{m_{eff,n}}} \tag{2.22}$$

where $k_{eff,n}$ and $m_{eff,n}$ denote effective spring constant and effective mass of the particular normal mode. These effective parameters are specific for each mode and

shape of the resonator can be normally found in tables where the shape of the resonator is reported, the position of the clamping, the interested mode and so on. e.g. for the fundamental-mode of a simple clamped-clamped beam, the effective mass and the effective spring constant, to be used in Eq. 2.22, are given as [28]:

$$m_{eff} = 0.735\rho Lhw, \tag{2.23}$$

$$k_{eff} = 32\frac{Eh^3w}{L^3}. \tag{2.24}$$

Here L, h, w are the dimensions of the beam, E is Young's modulus, and ρ is the mass density of the beam.

2.2.1 Damped vibration with lumped-element model

In the previous chapter for the calculation of the eigenfrequency the dissipative forces were neglected, thus assuming the total energy as a constant at any time. In a real vibrational system energy is always dissipated by viscous damping, acoustic transmission, surface losses, internal dissipation, etc. Dissipative forces are approximately proportional to the velocity of the vibrational movement [11] and are often modeled as a dashpot, as shown in Fig. 2.4.

Considering an undriven system, the equation of motion 2.19 reduces to the homogeneous differential equation:

$$\ddot{z} + 2n_c\dot{z} + \Omega z = 0 \tag{2.25}$$

with the damping coefficient

$$n_c = \frac{c}{2m}. \tag{2.26}$$

Introducing as trial solution $z = z_0e^{\gamma t}$ and inserting it in 2.25, we obtain solutions that satisfy

$$\gamma_{1,2} = -n_c \pm \sqrt{n_c^2 - \Omega^2}. \tag{2.27}$$

The ratio between n_c and Ω is defined as the "damping ratio", a parameter that gives information about the system performance:

$$\zeta = \frac{n_c}{\Omega}. \tag{2.28}$$

In fact, if $\zeta \geq 1$, γ is real and the solution of 2.25 is an exponential decay. In this situation the system is defined as heavily damped (over-damped case). For a slightly damped system (under-damped case) $\zeta < 1$, 2.27 becomes imaginary:

$$\gamma_{1,2} = -n_c \pm i\sqrt{n_c^2 - \Omega^2}. \tag{2.29}$$

For a linear homogeneous ordinary differential equation the linear sum of linearly independent solutions (real and imaginary) are valid solutions, thus we can rewrite the trial solution proposed for 2.25 applying the Euler's formula:

$$z(t) = z_0 e^{-\Omega\zeta t} cos\left(\Omega\sqrt{1-\zeta^2 t}\right). \tag{2.30}$$

The above equation 2.30 indicates that the system has an exponentially decaying oscillation with a, so-called, "natural frequency" $\omega_{nat} = \Omega\sqrt{1-\zeta^2} = \sqrt{\Omega^2 - n_c^2}$. The solution 2.30 is plotted in Fig. 2.5.

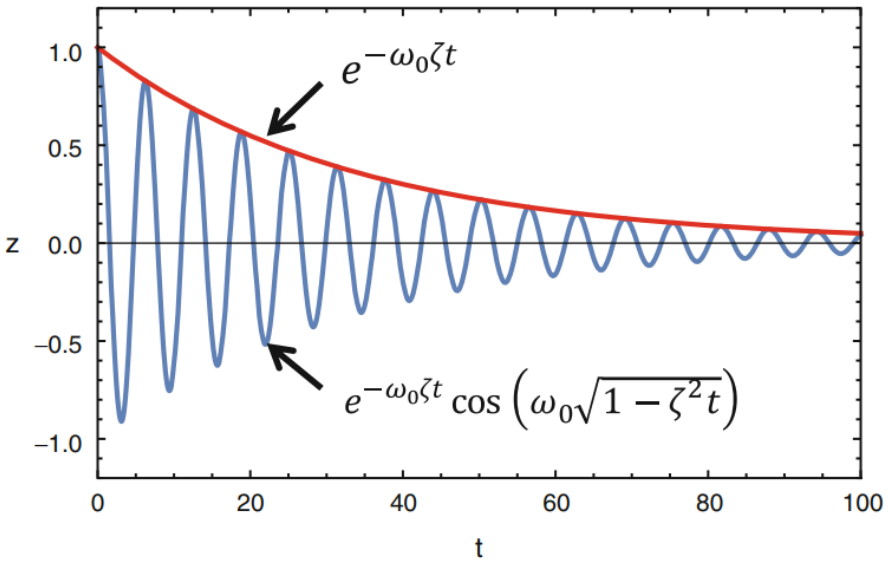

Figure 2.5: Plot of 2.30 for $z_0 = 1$, $\Omega = 1$, and $\zeta = 0.03$. Courtesy of [11].

2.2.2 Driven and damped vibration with lumped-element model

Considering also an external driving force (a schematic drawing of the system is reported in 2.6), the solution of the equation of motion 2.19 is the sum of the transient solution of the homogeneous differential equation of the damped case 2.30 and a specific steady solution that is described by:

$$z(t) = z_0 e^{i\omega t} \tag{2.31}$$

where z_0 is the amplitude of the resulting vibration.

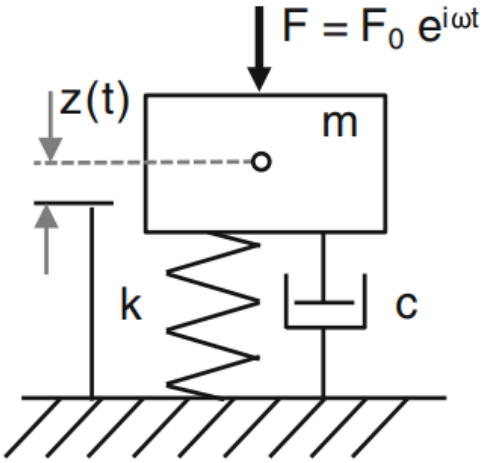

Figure 2.6: Schematic drawings of a driven damped vibration of a lumped system. Courtesy of [11].

Inserting the described solution 2.31 in the equation of motion 2.19 returns:

$$z_0 = \frac{F_0/m}{(\Omega^2 - \omega^2) + 2i\zeta\Omega\omega}. \tag{2.32}$$

This complex amplitude can be converted to the polar form, with the norm:

$$|z_0| = \frac{F_0/m}{\sqrt{(\Omega^2 - \omega^2)^2 + 4\zeta^2\Omega^2\omega^2}} \tag{2.33}$$

and the phase:

$$arg(z_0) = \varphi = arctan\frac{2\zeta\Omega\omega}{\omega^2 - \Omega^2}. \tag{2.34}$$

Thus, the real specific solution described above 2.31 then becomes:

$$z(t) = \frac{F_0/m}{\sqrt{(\Omega^2 - \omega^2)^2 + 4\zeta^2\Omega^2\omega^2}} cos(\omega t + \varphi). \tag{2.35}$$

Both the amplitude 2.33 and phase response 2.34 can be rewritten as a function of the relative frequency ω/Ω:

$$|z_0| = \frac{F_0/k}{\sqrt{\left(1-\left(\frac{\omega}{\Omega}\right)^2\right)^2 + 4\zeta^2\left(\frac{\omega}{\Omega}\right)^2}} \tag{2.36}$$

$$arg(z_0) = \varphi = arctan\frac{2\zeta\left(\frac{\omega}{\Omega}\right)}{\left(\frac{\omega}{\Omega}\right)^2 - 1} \tag{2.37}$$

The numerator of the amplitude 2.36 represents the static deflection. Hence, the relative amplitude response (also called "dynamic amplification" or "gain") is then obtained insulating the rest of the amplitude equation:

$$\delta z_0 = \frac{1}{\sqrt{\left(1-\left(\frac{\omega}{\Omega}\right)^2\right)^2 + 4\zeta^2\left(\frac{\omega}{\Omega}\right)^2}} \tag{2.38}$$

Both amplitude and phase response of a linear resonator are plotted respectively in 2.7a an 2.7b.

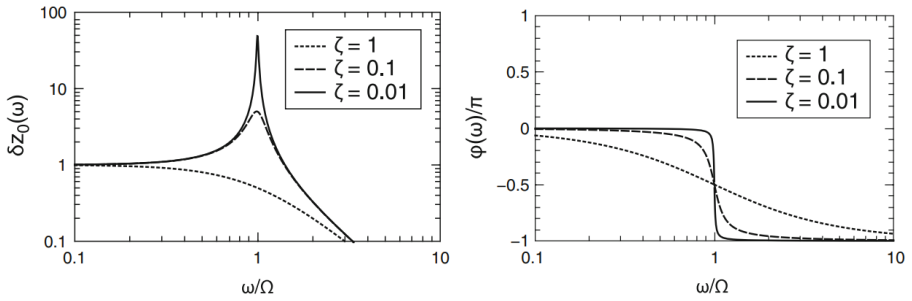

(a) (b)

Figure 2.7: (a) Amplitude (2.38) and (b) phase (2.37) responses for a damped resonator driven by a force. Courtesy of [11].

Considering a slightly damped system ($\zeta < 1$), it can be seen from 2.38 that the amplitude has a maximum near the eigenfrequency Ω, the so-called resonance peak. The frequency of the highest amplitude is called "resonance frequency" ω_r, given by:

$$\omega_r = \Omega\sqrt{1-2\zeta^2}. \tag{2.39}$$

For slight damping, the resonance frequency is very close to the eigenfrequency of the system $\omega_r \approx \Omega$.

2.3 Mass Responsivity

One of the most widespread applications of the micro- and nanomechanical resonator is the detection of small masses, also topic of my thesis.
From equation 2.22 it is clear that the resonant frequency depends on the vibrating mass. One of the most important indicators of whatever mass sensor is the mass responsivity ($\Re_m$). The responsivity is defined as the slope of the sensor output as a function of the input parameter to be measured. The responsivity is constant over the linear range of the sensor. So, for a resonant mass sensor, the responsivity is defined by the variation of resonance frequency due to a change in mass.
In a first approximation, we can assume the resonator as slightly damped and so consider it as a linear lumped-element oscillator, thus its mass responsivity is given by:

$$\Re_m = \frac{\partial \Omega(m_{eff})}{\partial m_{eff}} = -\frac{1}{2}\frac{\Omega(m_{eff})}{2m_{eff}}. \tag{2.40}$$

It is easy to understand that to have a high responsivity the resonator should have a little mass and a high resonance frequency. The responsivity is usually expressed in Hz/g or in some of their multiples, in this thesis will be reported in mHz/ag (and positive).

2.4 Quality Factor

The Quality factor (usually indicates as Q-factor) is a quantity that plays a key role for understanding the behavior of a mechanical resonator. It is defined as the ratio of stored energy versus lost energy during one circle of vibration. A high quality factor is typical of a resonance peak with an enhanced vibrational amplitude and a reduced peak width. The total quality factor of a resonator is the sum of different dissipation mechanisms[11]

$$\frac{1}{Q} = \frac{1}{Q_{medium}} + \frac{1}{Q_{clamping}} + \frac{1}{Q_{intrinsic}} + \frac{1}{Q_{other}}. \tag{2.41}$$

Q_{medium} sums up all the losses due to the interaction of the mechanical structure with a fluidic medium, $Q_{clamping}$ are losses from energy radiating into the environment over the physical clamping sites of the resonator, and $Q_{intrinsic}$ summarized all dissipation mechanisms happening within the resonator. Q_{other} stands for all loss mechanisms that are not covered by the first three. An example of the effects of the fluidic medium surrounding the resonators is reported in fig 2.8. Another way to define the Q-factor is the frequency-to-bandwidth ratio of the resonator [48]:

$$Q = \frac{f_r}{\Delta f} \tag{2.42}$$

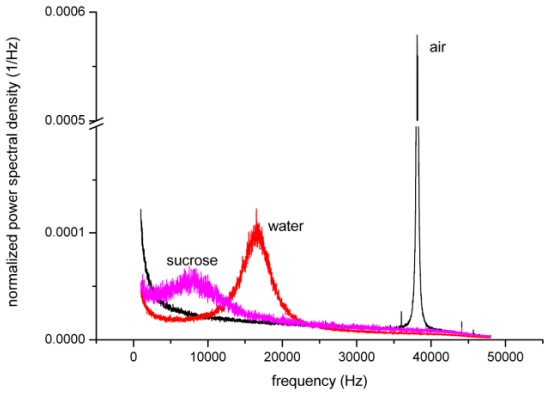

Figure 2.8: Experimental curves obtained in different conditions, in which the effects of the environment surrounding the resonators is evident. From [47]

where f_r is the resonant frequency and Δf is the resonance width or full width at half maximum (FWHM), i.e. the bandwidth over which the power of vibration is greater than half (or equivalently the amplitude at -3dB) the power at the resonant frequency. There two ways to define the Q-factor are not exactly equivalent, but they become approximately equivalent as Q becomes larger, meaning the resonator becomes less damped [48].
As already said, the mass detection is based on the frequency shift measurement and so it is easy to understand that spectra with narrower and well-determined peaks (and so with a high Q-Factor) are better for this purpose. In fact, the minimum detectable mass Δm_{min} of a resonance sensor depends on the minimum detectable frequency shift Δf_{min}, that is strictly related with the Q-factor.
There are many noise contributions that may affect the detection, but the most impacting one is the "thermomechanical fluctuations" one. These fluctuations are due to the temperature T of the environment in which the resonator works. As a result, a thermal random motion is induced and the resonance frequency can be shifted. Thus, we can consider as minimum measurable frequency shift Δf_{min} the one which is equal to the temperature-induced fluctuations. We can formulate is as [28, 49]

$$\Delta f_{min} = \frac{1}{\sqrt{\langle z^2 \rangle}} \sqrt{\frac{f_0 k_B T B}{2\pi k_{eff} Q}}, \tag{2.43}$$

where $\langle z^2 \rangle$ is the mean square amplitude of vibration of the resonator, k_B is the Boltzmann constant, T is the absolute temperature and B is the bandwidth in which the measurement is performed. To define the minimum detectable mass it is standard practice to take the mass related to a frequency shift Δf three equal to three times the noise [50]. Thus substituting $\Delta f = 3\Delta f_{min}$ in the equation of the mass responsivity 2.40 and using the previous expression for the thermomechanical

frequency fluctuation 2.43 (neglecting the minus) we have:

$$\Delta m_{min} = \frac{2m_{eff}}{f_0} \frac{3}{\sqrt{\langle z^2 \rangle}} \sqrt{\frac{f_0 k_B T B}{2\pi k_{eff} Q}}, \tag{2.44}$$

or writing it in a clearer way, highlighting only the most important quantities:

$$\Delta m_{min} \propto \frac{m_{eff}}{\sqrt{f_0 Q}}. \tag{2.45}$$

Looking at the last equation it is easy to see that to detect a small mass it is crucial to have a resonator of reduced dimensions (and so with a small effective mass and a high resonance frequency), but also to have a high quality factor becomes necessary. Moreover, since the principle of working of a mass sensor, based on mechanical resonance, relies on a shift of the resonance frequency (and so a difference between these two values), it is easy to understand that the shift may be more and more accurate (and small) if the two peaks are very sharp and narrow: thus to have a high Q-factor.

Chapter 3

Design

The concept behind the realization of this suspended nanochannel resonators is to fabricate devices with a sensitivity high enough to be able to detect and characterize nanoparticles. To give an idea of the order of magnitude of mass to be detected we can consider silver nanoparticles. The silver has a density of 9.320 g/cm^3. If we consider the particles as perfect spheres with the diameter going from 20 nm to 50 nm we obtain a mass that covers a range from 45 ag to 700 ag.

Defined the target mass we can start to think about the dimensions of the sensor. The theoretical mass responsivity of a mass resonator, as seen in the previous section (2.3) can be defined as:

$$\Re_m = \frac{1}{2}\frac{f_r}{m} \approx \frac{\Delta f_{min}}{\Delta m_{max}} \tag{3.1}$$

where f_r is the resonance frequency and m the mass of the resonator. In order to maximize the mass responsivity, a beam should thus have both high resonance frequency and small mass. To find the target responsivity one of the approximations that can be done is to consider the ratio between the minimum appreciable (by the characterization tool) shift in frequency resonance and the maximum mass to be characterized.

$$\Re_m = -\frac{1}{2}\frac{f_r}{m} \tag{3.2}$$

The characterization (that will be deeply explained later in sections 5 and 6) is done with a laser Doppler vibrometer that has a sampling resolution of 5Hz on a 2 MHz range, with the settings used in this thesis. A periodic chirp is used as exciting signal for the actuators, with this setting the spectra of the frequency start always from 0 Hz. The tool performs a FFT (fast Fourier transform) to convert the measured signal from the time domain toward the frequency one. One of the parameters of the FFT is the "FFT Size" (or "FFT line") that represents the number of equally-spaced samples used in the discrete Fourier transform algorithm.

The selected FFT size directly affects the resolution of the resulting spectra, in fact the frequency resolution of each spectral line is equal to the bandwidth of sampling divided by the FFT size. Larger FFT sizes provide higher spectral resolution but take longer to compute. In this thesis a range between 102400 and 409600 lines are used. The frequency resolution of 5 Hz is thus obtained from the ratio between the 2 MHz bandwidth of characterization and the maximum of lines. The target resolution, considering the above assumptions, has to be comprised in a range of 110 mHz/ag ÷ 7 mHz/ag in order to be able to see a shift, for a single nanoparticle, in the measured signal.

In this work three different kinds of devices have been designed, in order to fulfill the requirements and, meanwhile, deal with the technological constraints of the fabrication lab (CMi@EPFL).

The first one is the nanoslit devices, characterized by the channel with only one nanometric dimension (the thickness) while the other two are at the micrometric scale, designed mainly to optimize the fabrication process but with a enough good sensitivity to be used anyway as mass sensor for nanoparticles detection.

Then, I scaled the width of the channel to the nanometric scale, thus designing the nanochannel devices, to reduce the overall dimension and mass of the resonator, increasing its mass sensitivity.

In the last design, I fabricate a channel with a height enlargement in the middle of the channel to exploit a localized change in the electrostatic charge to immobilize the nanoparticles flowing through it.

The height of the channel has been designed considering mainly the nanochannel design. The idea was to build a channel of the same order of magnitude with respect to the nanoparticles to analyze. In this way is possible to have a diffusion of particles in a narrow channel where mutual passage is forbidden, this situation is typical of diffusion in unidimensional channel structures and it is known as single-file diffusion (SFD) [51]. The target nanoparticles have a diameter range of 20 nm to 50 nm, thus also the channel should have a comparable size. 30 nm would be too challenging as first attempt with a top-down approach with the available technologies in the CMi@EPFL, so the final choice was use in the design a 50 nm dimension.

The three families of devices have similar dimensions to have comparable results in resonance frequency and to use the same fabrication process, with only some variations where needed. An overview on the resonators dimension is reported on figure 3.1.

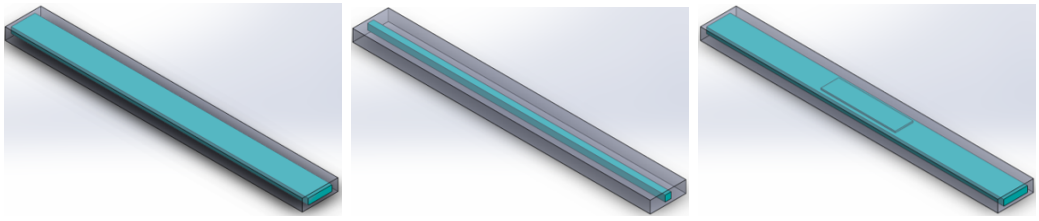

(a) Nanoslit device
Height: 450 nm
Width: 6-9 µm
Length: 50 µm

(b) Nanochannel device
Height: 450 nm
Width: 6-5 µm
Length: 20-40 µm

(c) 2 step channel device
Height: 450 nm
Width: 6-9 µm
Length: 50 µm

Figure 3.1: The sketches of the three different devices are here reported, with the quotes for the bridge. The blue part is representing the channel (not in scale)

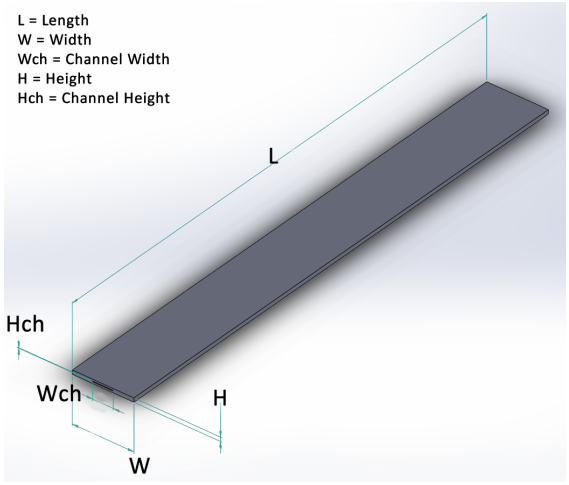

Figure 3.2: Sketch of the symbols used to name the quotes

3.1 Nanoslit devices

The nanoslit device has been designed with a double purpose: to optimize the process and to have a mass sensitivity good enough to reach the attogram scale. Furthermore, I had to deal with the technological constraints of the fabrication and characterization tools available.

In the end, the best compromise I found was to use the following dimensions:

- length of the bridge: 50 µm;
- width of the bridge: 6-9 µm;
- height of the bridge: 450 nm;
- length of the channel: 80 µm;

- width of the channel: 2-5 µm;
- height of the channel: 50 nm;

All the in-plane sizes are at the micrometer scale to allow the use of the optical microscope for the inspection during the fabrication process. Scaling down the sizes would have required the use of the scanning electron microscope, with a consequent increasing of times and costs.
The channel is 30 µm longer compared to the bridge to allow the connection with the external microfluidic and the insulation of the vibrational cavity.
The channels are 2 µm narrower with respect to its relative bridge, to have space for the alignment tolerance between the different photolithographic masks. Furthermore, different widths of the channel have been tested to find the optimal one considering both the fabrication process and the characterization. So, two different generations of chips have been produced: a first one with a series bridges with channels of increasing width and a second one with only one bridge. The idea behind the solution with only one suspended bridge is to be sure, when injecting nanoparticles, where to perform the measurement.

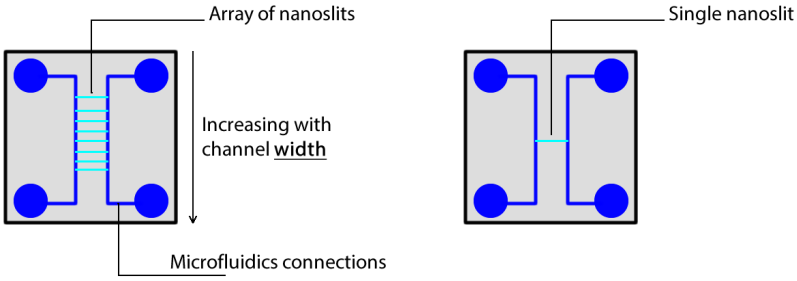

(a) 1st generation of chip (b) 2nd generation of chip

Figure 3.3: The sketches of the two generations of chips. The blue part represents the microfluidic connection between the inlets/outlets and the channels. The cyan lines represent the suspended bridges. Not in scale

The expected resonance frequency for this kind of devices is, in a first analysis, calculated using the following equation [11]:

$$f_n = \frac{L_n^2}{2\pi L}\sqrt{\frac{EI_y}{\rho A}} \tag{3.3}$$

where L_n represent the modal coefficient, L is the length of the resonator, E, I_y, A, ρ are respectively the Young's modulus, the geometric moment of inertia, the cross-section area and the density. Since the geometric moment of inertia for a clamped-clamped resonator is $I_y = (A * h^2)/12$, where A is the cross area and h the height of the resonator, can be easily seen that (theoretically) the resonance frequency is depending only on length and thickness of the resonator, not on the width. This mean that in the chips of the 1st generation the theoretical resonance frequency will be the same for each bridge. The same does not occurs when we will consider the experimental measurements. To calculate the resonance frequency we can proceed substituting the parameters of the equation 3.3 with their actual value. For density and Young's modulus have been used the values for the chosen material in the devices: Silicon Oxide (the motivations behind this choice will be explained later in this thesis, in section 4).

- L_n=4.7300: the modal coefficient for the first resonance mode[11];
- L = 50 µm;
- $A = w * h$: h = 450nm and w = 6-9 µm
- E = 56 GPa [52];
- ρ = 2180 kg/m^3 [52];

The estimated resonance frequencies and the relative mass responsivities are reported in Table 3.1. As said above, the length and the thickness are in common among all the devices, here is reported only the width.

Width	Channel Width	Resonance Frequency	Mass	Sensitivity
2 µm	6 µm	937.76 kHz	141.7 pg	3.309 mHz/ag
3 µm	7 µm	937.76 kHz	163.5 pg	2.867 mHz/ag
4 µm	8 µm	937.76 kHz	185.3 pg	2.530 mHz/ag
5 µm	9 µm	937.76 kHz	207.1 pg	2.264 mHz/ag

Table 3.1: Estimated resonance frequencies and sensitivities for nanochannel devices with analytical equation

3.1.1 Finite Element Method (FEM) Simulation

To have a further confirmation (and a better approximation) of the expected resonance frequencies of the devices, a finite element method (FEM) simulation has been done in support of the analytical analyses. The idea behind the FEM is to subdivide the object under analysis into smaller, simpler parts that are called finite elements. Then solve the physical equations describing the behaviors under study with numerical methods in a system that takes in account every single finite elements. The advantage of this kind of simulation is that gives a result closer to the real case with respect to the analytical equations, since the equations are not approximated.
The program I used to accomplish this kind of calculation is Comsol Multiphysics®, it includes a cross-platform for finite element analysis, a solver for the equations and a multiphysics simulation software. It allows to analyze conventional physics-based user interfaces and coupled systems of partial differential equations (PDEs).

The model has been set up exploiting the Structural Mechanics Module, with a study looking for the eigenfrequencies of the solid as result. The 3D solid model, a simplified structure representing the beam can be seen in figure 3.4, it has been built directly with the Comsol CAD.

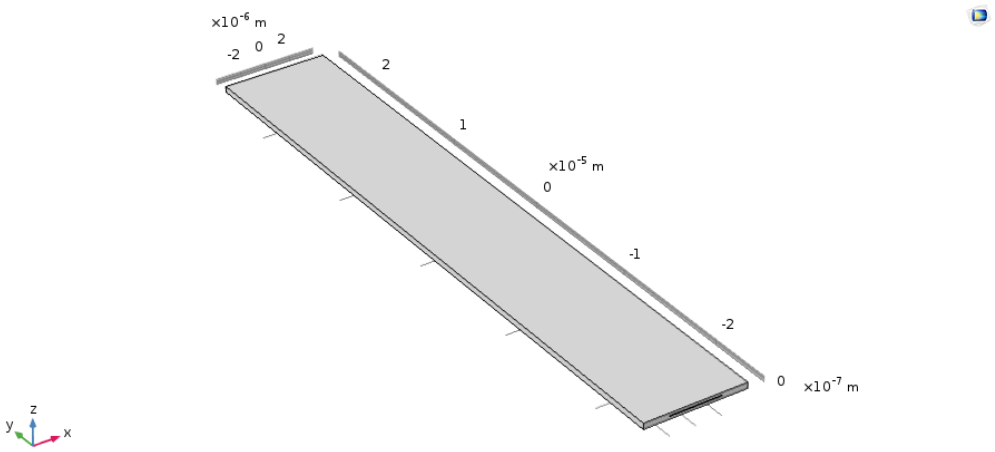

Figure 3.4: 3D solid model of the simplified structure representing the beam used for the FEM simulation.

A physics-controlled mesh has been used. This kind of mesh is built to be denser (and so with smaller elements) on the crucial points of the structural model, as the boundaries of the channel in my device.
The mesh has been built with tetrahedral elements, with the following definitions:

- Maximum element size: 1.75 µm;

- Minimum element size: 75 nm;
- Maximum element growth rate: 135;
- Curvature factor: 0.3;
- Resolution of narrow region: 0.85;

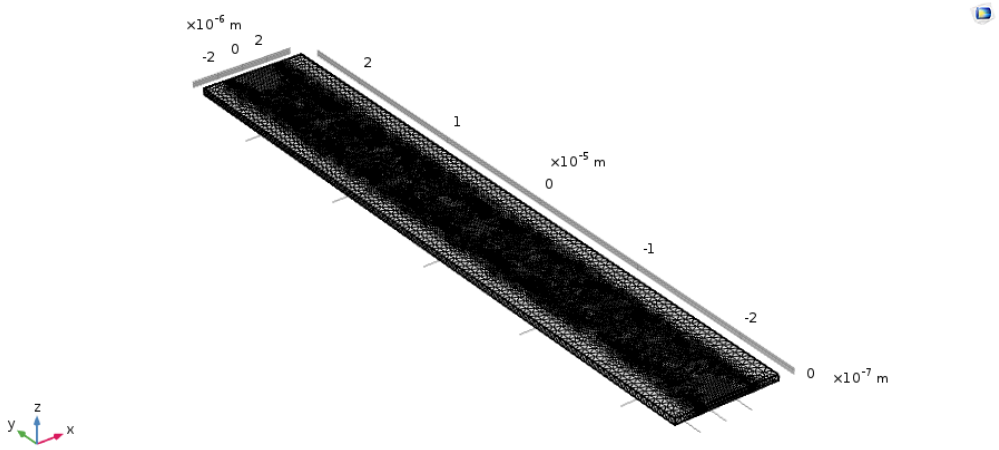

Figure 3.5: 3D model reporting the extrafine mesh used for the FEM simulation

The physical proprieties used for the material are the same specified and used above for the analytical analyses. To mimic the clamping of the edges of the beam a fixed constraint to the two extremities has been added. The fixed constraint is nothing but a boundary condition that imposes a null displacement on that face.

The resonance frequencies are thus calculated and the obtained results, for the first mode, are reported in the Table 3.2. A picture representing the first modal eigenmode for the model under analyses is below reported 3.6.

Width	Channel Width	Resonance Frequency	Mass	Sensitivity
2 µm	6 µm	1.0647 MHz	141.7 pg	3.757 mHz/ag
3 µm	7 µm	1.0668 MHz	163.5 pg	3.262 mHz/ag
4 µm	8 µm	1.0654 MHz	185.3 pg	2.875 mHz/ag
5 µm	9 µm	1.0609 MHz	207.1 pg	2.561 mHz/ag

Table 3.2: Estimated resonance frequencies and sensitivities for nanoslit devices with FEM calculation

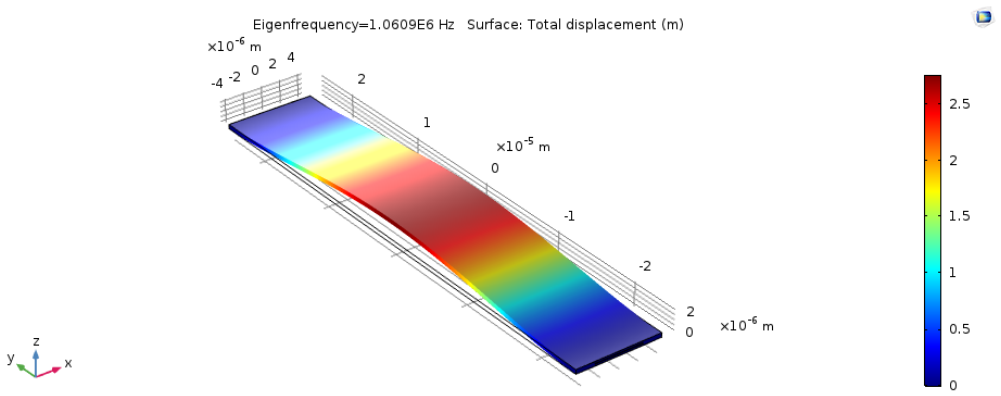

Figure 3.6: First modal eigenmode for a clamped-clamped beam (width = 5 µm) simulated with Comsol.

Comparing the results obtained from the FEM calculation and from the analytical equation can be noticed that:

- the resonance frequencies are now varying with the width;
- there is an increasing of the values of the resonance frequencies of about 13%.

The both differences with respect to the analytical case can be explained by the fact that, with the FEM simulation, the inner channel is now taken in account in the elastic proprieties of the material and in the geometry of the device. The mass of the device is lower and the fact that there is a hollow channel inside the beam affects the way which it can sustain and respond to the stress and the strain.
The obtained results from both the analyses confirm the goodness of the proposed design because the estimated sensitivities reach the sufficient range to detect a group of nanoparticles flowing in the bidimensional channel, although the main purpose of this devices is to do a proof of concept for the fabrication process towards the nanochannel devices.

3.2 Nanochannel devices

The nanochannel devices have been designed to have a higher mass responsivity with respect to the nanoslit ones. In fact, regarding at the formula 4.3 smaller is the mass of the resonator, higher is the capability to sense small masses as nanoparticles. Here, the reduction will occur mainly on the dimensions of the channel, being nano also in width, and in the length of the resonator. So, from a point of view of fabrication process, only the step defining the lateral dimension of the channel will be highly changed passing from a photolithography toward an electron beam lithography.

The dimensions designed to these devices are:

- length of the bridge: 20/30/40 µm;
- width of the bridge: 4-6 µm;
- height of the bridge: 450 nm;
- length of the channel: 80 µm;
- width of the channel: 20-100 nm;
- height of the channel: 50 nm;

In these devices a tapering has been added between the inlets and the extremities of the channel to help the liquid to flow from a microfluidic regime toward a nanofluidic ones.

Using the above equation 3.3 the resonance frequencies of the different devices can be estimated, and thus their theoretical mass responsivity. The results, only for the 100 nm wide channel, are reported in table 3.3; the devices with a narrower channel will have a higher effective mass but the variation is, in a first approximation of design, negligible. The material used is the same of the nanoslit devices, thus also the material proprieties used in the formula 3.3.

Length	Width	Channel Width	Resonance Frequency	Mass	Sensitivity
20 µm	4 µm	100 nm	5.861 MHz	39.1 pg	74.889 mHz/ag
20 µm	5 µm	100 nm	5.861 MHz	48.9 pg	59.878 mHz/ag
20 µm	6 µm	100 nm	5.861 MHz	58.7 pg	49.880 mHz/ag
30 µm	4 µm	100 nm	2.605 MHz	58.6 pg	22.189 mHz/ag
30 µm	5 µm	100 nm	2.605 MHz	73.4 pg	17.742 mHz/ag
30 µm	6 µm	100 nm	2.605 MHz	88.1 pg	14.779 mHz/ag
40 µm	4 µm	100 nm	1.465 MHz	78.2 pg	9.361 mHz/ag
40 µm	5 µm	100 nm	1.465 MHz	97.9 pg	7.485 mHz/ag
40 µm	6 µm	100 nm	1.465 MHz	111.8 pg	6.235 mHz/ag

Table 3.3: Calculated resonance frequencies and sensitivities for nanochannel devices with analytical equation

As can we see in the table 3.3, the estimated sensibility of these devices is slightly lower than the optimal one calculated for the 20 nm diameter nanoparticles. Anyway, the obtained results for the 20 µm long devices (≈ 60 mHz/ag) are valuable for single nanoparticles detection considering a little larger diameter, about 25 nm. For the 30 µm long devices the predicted sensitivity (≈ 18 mHz/ag) would be enough to

detect nanoparticles with diameter starting from 35 nm. The 40 µm have the worst responsivity, but they can be used as benchmark for the vibrational proprieties of the resonator: smaller is the devices, harder it is its characterization and, so, for a first analysis to understand the output of the process can be useful to have a bigger resonator.

3.3 2-Step Nanoslit devices

The devices described above have the capability to sense the nanoparticles when these are flowing through the channel but do not offer the possibility to stop them in a determinate position and let the solution flow on and around them. The situation just described is the typical one used to study the kinetic of dissolution of a particle in liquid. Madhavi Krishnan in a work published on Nature in 2010 offer an elegant solution, compatible with ours devices, to overcome this issues: she exploited a geometry-induced electrostatic trapping to immobilize nanometric objects in a fluid [53].
To understand the working principle, we have to go back: when a liquid is put in contact with a solid a charged layer occurs at the surface of both. More specifically, in the liquid an electrical double layer (EDL) is formed: a first layer consists of ions adsorbed onto the object due to chemical interactions, while the second one is composed of ions attracted to the surface charge via the Coulomb force, electrically screening the first layer. For a better understanding a schematic of the process is reported in figure 3.7. The characteristic thickness of the EDL is the Debye length that is normally of the order of some nanometers (with thickness decreasing with the increasing concentration of the electrolyte of the liquid solution). On macro and micro scale, the effect of the EDL is negligible, but when dealing with the nanoscale the thickness of the channel become comparable with the Debye length and so the EDL can have an influence on the fluidics.

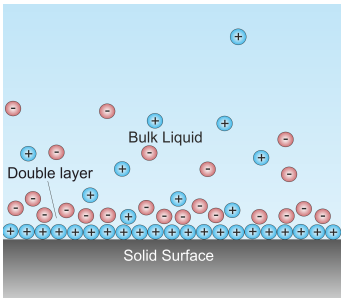

Figure 3.7: Schematic of an EDL in a liquid at contact with a negatively-charged solid. Depending on the nature of the solids, there may be another double layer (not reported on the drawing) inside the solid. [54]

Indeed, changing locally the height of the nanochannel can bring to a different

profile in the electrostatic of the EDL, thus making an electrostatic trap.
This trap can be exploited to stop nanometric masses, as nanoparticles, also for several hours with the liquid solution flowing around them [53].

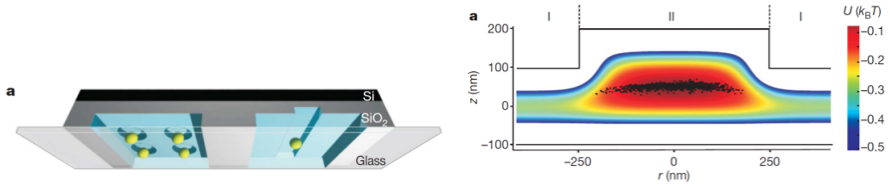

(a) (b)

Figure 3.8: Illustration of the geometry-induced electrostatic trapping. Pictures courtesy of [53]. (a) Skecth of the fluidic device with nanostructured slit surfaces. (b) Two-dimensional electrostatic potential achieved by solving the Poisson–Boltzmann equation for a pocket with cylindrical symmetry. The black symbols overlaid on the calculated potential distribution represent particles confined by the trap.

This kind of trapping could be useful to have a further degree of freedom for the characterizations, knowing the site of immobilization of the nanoparticles. In the devices, as reported in figure 3.7, the channel have two heights: 50 nm along the channel and 100 nm right in the middle, making a groove long 10 µm and 50 nm high. As I will explain better in the fabrication section 4.3, making this additional machining to the devices, it costs only the repetition of some steps, without upsetting the entire process. This variation has been applied only on the "nanoslit device" process since the alignment of the subsequent masks is very challenging. The expected analytical frequencies and mass responsivity are, thus, the same as the ones reported in the above table 3.1.

Chapter 4

Fabrication

In this chapter the processes developed and optimized to fabricate the three different versions of device (Nanoslit, Nanochannel and 2-Step Nanoslit) will be explained step by step. The aim was to set up a very flexible process in order to do only punctual modifications to fabricate the different devices.
The chapter is divided in three parts:

- a detailed description of the process flow developed for the Nanoslit devices;
- the modifications needed to fabricate the Nanochannel and the 2-Step Nanoslit devices;
- the optimization done to get the final process flow, to which the first point refers.

The fabrication part has been carried out at Centre of Micro and Nanotechnologies at the École polytechnique fédérale de Lausanne (CMi@EPFL). The process is based on a sacrificial layer approach using a 50 nm thick layer of silicon as removal part, removed subsequently with a dry etching done with XeF_2. Using the Xenon Difluoride as gas etching has many advantage: it allows very long etching thanks to the very high selectivity with respect to the silicon oxide (almost 1:1000) and, furthermore, being a dry etching, it avoids issues as stiction and it does not suffer of slow removal of the byproduct of the etching reaction.
The entire process consists in three lithographic steps (in which one can be done with electron beam lithography to pattern the nanochannel design) alternated with deposition and etching steps. Then, the sealing of the chip, with the creation of the microfluidic interface, is done bonding the device wafer with a patterned glass one.
The process flow to can be shortly described in this way:

- RCA Clean;
- silicon oxide deposition: TEOS LPCVD;

- sacrificial layer deposition;
- patterning of the sacrificial layer;
- burying of sacrificial layer: silicon oxide deposition;
- opening of the inlets;
- releasing the channel;
- structuring and releasing the bridge;

Every point of the above list will be deeply detailed in this chapter, starting with the description of the process flow for the nanoslit devices. Then, since the processes used for the three different devices are very similar, for the other processes it will be reported only the steps in which there are the variations at the main process.

Figure 4.1: Fabrication process in cross section. Yellow = Bulk silicon. Gray = SiO_2 deposited layer. Light Green = Si sacrificial layer.
a) 200 nm of TEOS LPCVD SiO_2 and 50 nm of amorphous silicon are deposited. b) The Si is patterned in lines 2-5 µm wide and 120 µm long. c) 200 nm of TEOS LPCVD SiO_2 is deposited to encapsulate the Si sacrificial layer. d) Two openings are etched to allow access to sacrificial layer. e) Sacrificial layer is etched with XeF_2. f) Beams are defined and released.

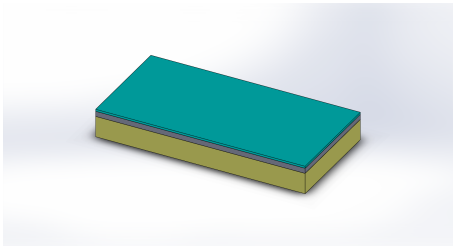

(a) 1st step

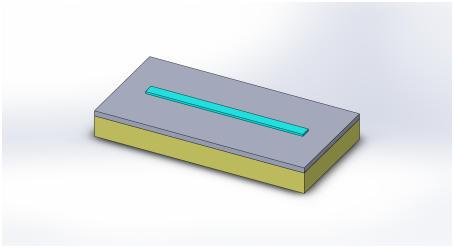

(b) 2nd step

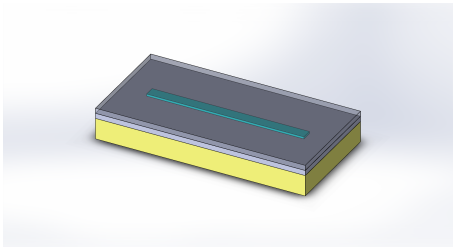

(c) 3rd step

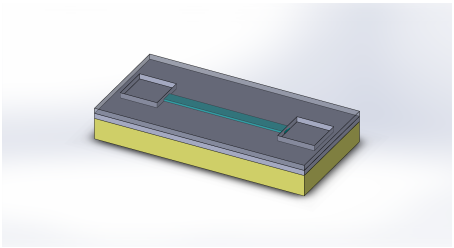

(d) 4th step

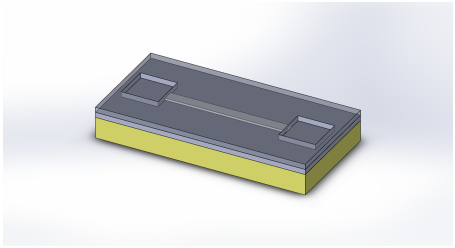

(e) 5th step

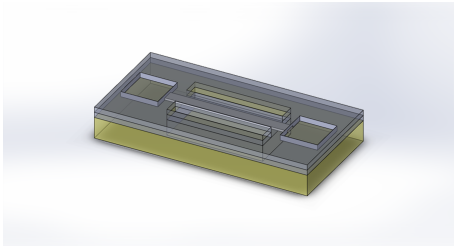

(f) 6th step

4.1 Nanoslit Device

The fabrication process starts with a deposition of 200 nm of SiO_2 on a pristine wafer. After several tests, reported later in this thesis, it has been found that the optimal structural oxide for this device is the one obtained with a Chemical Vapor Deposition (CVD) using TEOS (Tetraethyl orthosilicate) as precursor of the reaction at high temperature (710 °C).
The pristine wafer, before entering in the furnace, must be well cleaned to improve the adhesion of the oxide layer, reduce (or nullify) the impurity and avoid contamination to the deposition tools. In order to clean the wafer a RCA cleaning step has been done.

4.1.1 RCA Clean

The RCA cleaning is a standard protocol in the semiconductor manufacturing before high-temperature processing steps. It consists in four steps:

- First step (Standard Clean 1 - SC1): Organic and particle clean. The wafers are dipped in a solution containing 5 parts of deionized water, 1 part of ammonia water (29% by weight of NH_3) and 1 part of hydrogen peroxide (H_2O_2) at 75-80 °C for 10 minutes;

- Second step (optional): Oxide strip. silicon natively get oxidized when exposed to air, furthermore, the first step causes the growth of some nanometers of oxide that contain also ionic contaminants. To remove the oxide (and the contaminants) a short immersion in a 1:100 solution of aqueous hydrofluoridric acid (HF) at 25 °C is done to the wafers.

- Third step (SC2): Ionic clean. In this step the remaining contaminants (mainly metallic ions) are removed, the process is performed with a solution of 1 part of hydrochloric acid (HCl, 37% by weight), 1 part of hydrogen peroxide (H_2O_2, 30% by weight) and 6 parts of deionized water at 75-80 °C for 10 minutes. This step leaves a thin passivizing layer on silicon surface that prevents from subsequent contamination.

- Fourth step: SRD (Spin Rinsing and Drying). The wafers are then rinsed and dried to remove all the traces of the used chemicals.

4.1.2 Silicon Oxide Deposition: TEOS LPCVD

The cleaned wafer is now ready for the deposition. The choice of using the LPCVD TEOS to depositing silicon oxide has come after several trial (reported in the Optimization chapter 4.5.1) on the other available methods in the CMi@EPFL cleanroom showing that this was the best one for this process. The structural

layer of the device is deposited in two different steps, to allow the deposition of an interstitial sacrificial layer. In the optimized process the silicon oxide is deposited in the same way in both the steps to avoid as much as possible mismatching in the residual stress induced by the stacking of the different layers. For the second deposition a very conformal process was necessary (to completely bury the sacrificial layer) and so the TEOS silicon oxide LPCVD is indicated, thanks to its excellent proprieties of conformal coverage [55]. Furthermore the deposited layers are dense and pure (if deposited at high temperature - around 700 °C) and presents a smooth surface. The drawbacks to pay are a low deposition rate (5.5 nm/min at 710 °C) and a long purge sequences during the process. The deposition in my process was of 200 nm and lasts about 5 hours in total with a subsequent annealing at the same temperature.

The reaction occurring during the deposition (valid only for temperature higher than 600 °C) can be schematized as following 4.1:

$$Si(OC_2H_5)_4 \longrightarrow SiO_2 + 2\,(C_2H_5)_2O \tag{4.1}$$

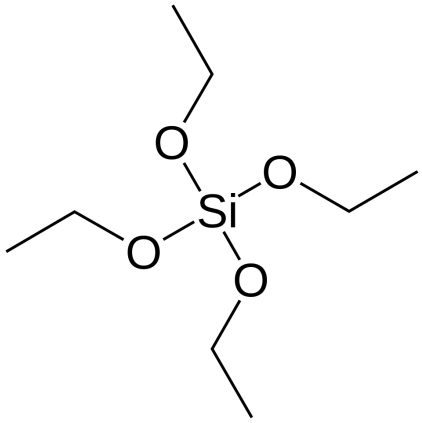

Figure 4.2: Skeletal formula of tetraethyl orthosilicate.

The optimization steps done for this part of the process are reported later in this thesis, in chapter 4.5.1.

4.1.3 Sacrificial layer deposition

The sacrificial layer is deposited by Sputtering, specifically it has been deposited with a Pfeiffer SPIDER 600 with a DC Maris signal generator. The recipe used for this deposition can be seen in the table 4.1. The deposition time used in my process was 27 s. This tool, unfortunately, does not have a shutter to inhibit the

deposition during the powering up of the plasma (the 20 s of ramp time in the recipe) and so a source of uncertainty on the real height of the sacrificial layer is present. Characterizations with Bruker Dektak XT (surface profiler) and a FilMetrics F20-UV (spectroscopic reflectometer and transmissometer) have returned results in a range between 40 - 50 nm of thickness for the layers deposited with this deposition time.
An example of these characterizations is below reported in Figure 4.3 showing a step of 51.709 nm between the silicon oxide surface and the patterned silicon sacrificial layer. Furthermore, also a characterization of the deposited layers has been done by a cross section image, obtained by SEM inspection after a Focused Ion Beam (FIB) milling, that show a 50 nm thick sacrificial layer, as can be seen in figure 4.4.

Power	Voltage	Ar	Deposition Rate	Ramp	Deposition time
800 W	460 V	29 sccm	105 nm/min	20 s	27 s

Table 4.1: Parameters of Si Sputtering deposition

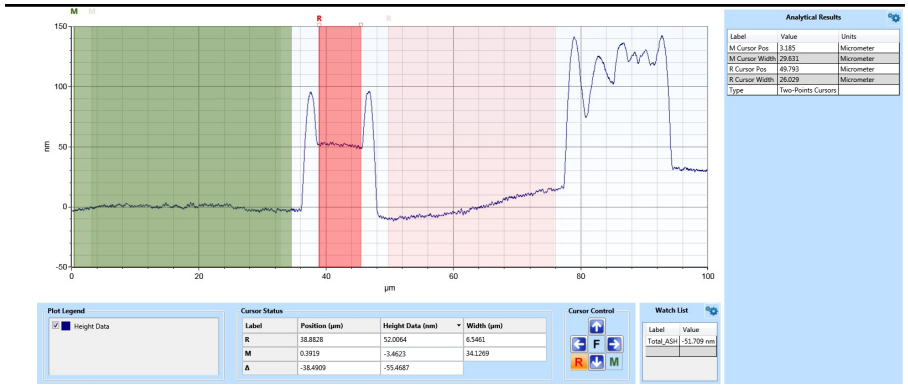

Figure 4.3: Characterization done with Bruker Dektak XT (surface profiler) on the thickness of the silicon sacrificial layer. The red box highlights the sacrificial layer, while the green one is on the silicon oxide. The result is given from the difference between the mean height of these two regions. The spikes on the edges are due to the movement of the tool tip.

We are now at the end of the first step of the process flow, as reported in Figure 4.1.

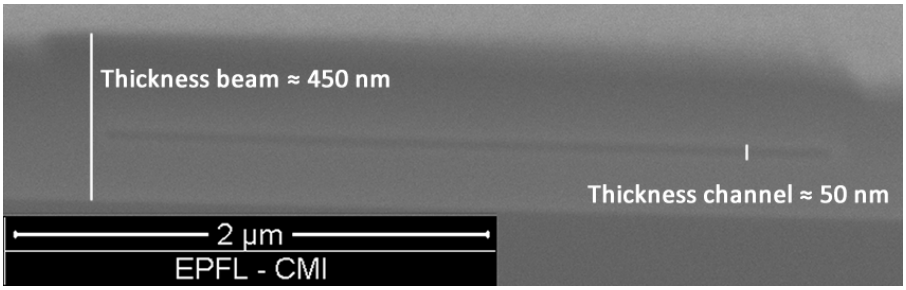

Figure 4.4: Cross section obtained with a FIB cut in the middle of an unreleased bridge: the darker layer is the silicon sacrificial layer surrounded by silicon oxide

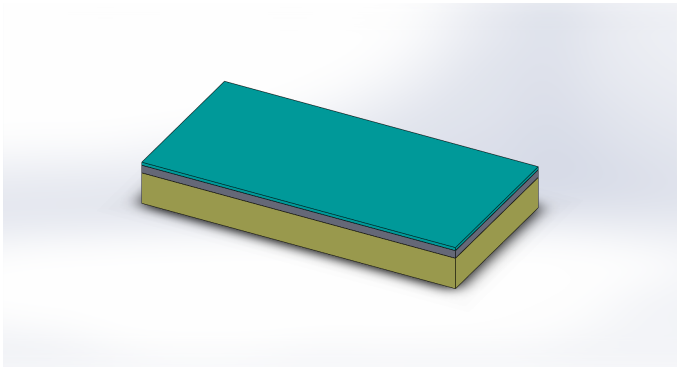

Figure 4.5: 1st step: 200 nm of TEOS LPCVD SiO_2 and 50 nm of amorphous silicon are deposited.

4.1.4 Patterning of the sacrificial layer

In this step the shape of the channel is developed through the lithographic step: it is one of the steps that vary according to the device-types under fabrication. In the case under explanation (the nanoslit) the critical dimension of the lithographic process is of the order of the micrometers and so an optical-based tools can be used. The nanochannel device case and the 2-step nanoslit will be explained better later in this thesis, respectively in section 4.2 and 4.3.

The lithographic step begins with the spinning of the photoresist on the wafer in the ACS200-GEN3 coater and developer tool, an automated machine that do all the steps necessary: from the spinning until the bake of the resist.
The chosen photoresist is the MicroChemicals AZ 1512 HS, a positive resist indicated for surface protection during the etching and with a lateral resolution that could go down to 1 µm depending on the resist film thickness. Thus, to minimize the critical patternable feature, the minimum (reproducible) thickness available between the collection of available recipes has been used: 1.1µm. To improve the adhesion of the polymer to the wafer, first, a surface preparation with vapor of HMDS is done. The spincoating, to obtain the target thickness, is then performed at 6000 rpm with a subsequent softbake at 112 °C for 90 s.

The exposure is executed with the Heidelberg MLA150, a direct laser writer with a system of maskless alignment. This system allows users to quickly print a design, without the need to order or produce a mask, by exposing the photoresist with a UV laser (375 or 405 nm) focused and scanned over the wafer.

The features that has to be transferred on the sacrificial layer are, practically, a series of rods with the dimensions showed in the table 4.2 and squares to indicate the inlet. An example of these features, taken from the mask used, can be seen in the Figure 4.6.

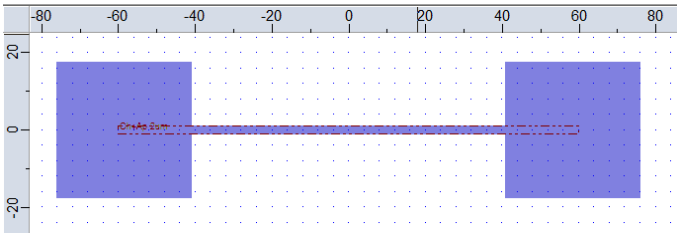

Figure 4.6: Part of the first lithographic mask

Length	Width	Thickness
82 µm	2 µm to 5 µm	50 nm

Table 4.2: Dimensions of channel features

The parameters used for the exposure, obtained after a "dose test exposure", are:

- Laser wavelength: 405 nm
- Dose: 40 mJ/cm^2
- Defoc: -2

After that, the wafer should return to the ACS200 to develop the resist. The recommended developer for AZ 1512 HS is MFCD26, an organic solution based upon TMAH. For a thickness of 1.1µm the ideal process time is 30 s, with a subsequent hardbake at 112 °C for 2 min.
After development, a spin-rinse-dryer (SRD) step with DI-water is highly recommended to avoid cross contamination and damage on instruments (chuck in etcher) in further processing steps.

To transfer the pattern from the resist to the sacrificial layer an etching step is required, to do that the Alcatel AMS 200 SE tool has been used. This etcher is an optimized Deep Reactive Ion Etching (DRIE) system for silicon (Si) and Silicon On Insulator (SOI) wafers with fluorine chemistry process. Its process chamber is equipped with a ICP (Inductive Coupled Plasma) source, a fine temperature controller and two possible wafer voltage biasing: RF (13.56 MHz) and pulsed Low Frequency (LF).
In my case, I needed a recipe with a very slow etching rate since I had to remove 50 nm of silicon without damaging the underlying oxide layer, the best one was the one called "Si Opto HR" (with RF biasing), whose parameters could be seen in the table 4.3; the etching rate was very difficult to be estimated since the small amount of mass removed.

Power coil	SF_6	C_4F_8	Power plate
1500 W	26 sccm	55 sccm	15 W
Chamber pressure		Time	Temperature
30 mbar		22 s	20 °C

Table 4.3: Parameters of "Si Opto HR" recipe

The resist is then removed with a plasma oxygen. We are now at the end of the second step of the process flow, as reported in Figure 4.1. An optical picture of the obtained result after this step is reported in figure 4.8. The shape of the inlets has been changed during the optimization of the process from rounded to squared to make easier the alignment.

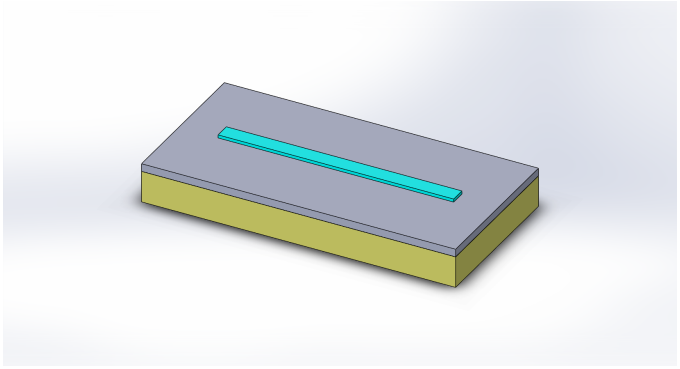

Figure 4.7: 2nd step: the Si is patterned in lines 2-5 µm wide and 120 µm long.

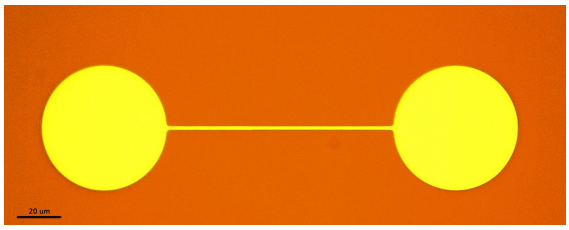

Figure 4.8: Optical image of the patterned sacrificial layer

4.1.5 Burying of sacrificial layer: silicon oxide deposition

The preparation of the wafer for the deposition is the same as described above in the "RCA clean" paragraph 4.1.1, except for the oxide strip step that now is avoided. Thereafter, another 200 nm layer of SiO_2 is deposited using the same process as the first step, in order to limit as much as possible, the internal stress that could buckle the clamped-clamped beam after the release step. In this deposition the conformality of the TEOS-based deposition is very useful to fully cover the rods made by during the patterning of the sacrificial layer. We are now at the end of the third step of the process flow, as reported in Figure 4.1.

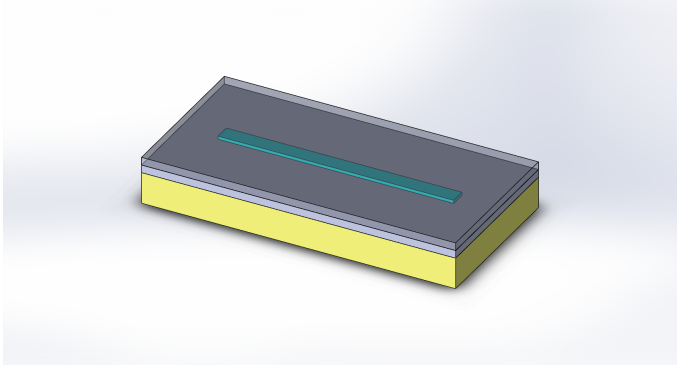

Figure 4.9: 3rd step: 200 nm of TEOS LPCVD SiO_2 is deposited to encapsulate the Si sacrificial layer.

4.1.6 Opening of the inlets

The wafer now undergoes to another lithographic step in which are patterned the openings for the sacrificial layer. The process for this step is analogous as the previous lithographic one: ACS200 coating with 1.1 µm AZ 1512 HS resist, exposure with MLA150 and then developing again in ACS200. In this case, the mask is no more "inverted" by the tool since there is only few polymer to remove. The aim, here, is to protect all the wafer except where I want the opening. The exposure dose is higher than before: 55 mJ/cm^2. Here is reported a part of the mask used in this lithographic step 4.10:

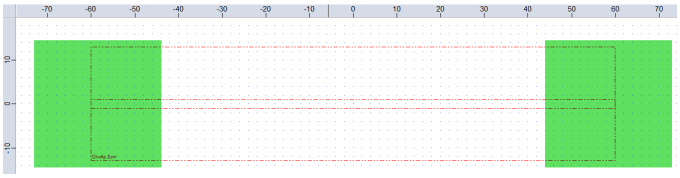

Figure 4.10: Part of the second lithographic mask.

To etch the silicon dioxide the SPTS Advanced Plasma System (APS) has been used. This instrument is similar to the AMS200 previously used, but it is devoted to the etching of insulators (SiO_2, Si_3N_4 and SiC), metals (Al Alloys, Pt, Ti) and some polymers. The characteristics are mainly the same: ICP plasma source and fine temperature control while the gas chemistry here is different. Here I need to etch the top layer of 200 nm of silicon oxide without overetch the underlying oxide structural layer to prevent overetching problems during the subsequent XeF_2 releasing step. In fact, if the bottom oxide layer is damaged, also the bulk silicon could be removed by the xenon difluoride etching step. The chosen recipe, "SiO_2 PR 5:1", has a slow etching rate to better control the depth of the etching and a good selectivity upon the silicon and the photoresist; the main parameters could be seen in the table 4.4.

Power coil	Power plate	Substrate temperature
1200 W	300 W	10 °C
CHF_3	H_2	C_4F_8
175 sccm	30 sccm	10 sccm
SiO_2 Etching rate	Si Etching rate	Time
260 nm/m	30 nm/m	60 s

Table 4.4: Parameters of "SiO_2 PR 5:1" recipe

To control the deep of etching is critical, otherwise it is very easy to damage the underlying layer of oxide, as in the example reported in Figure 4.11.

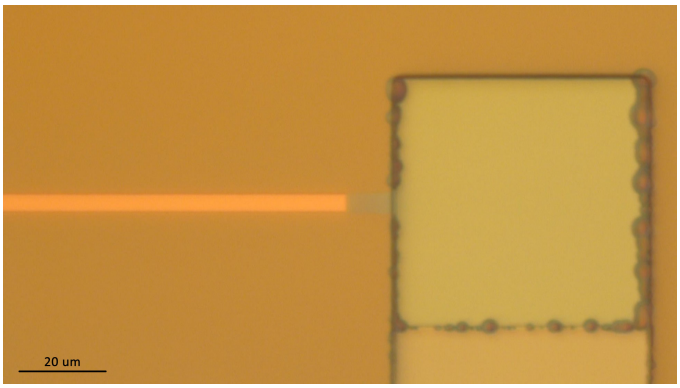

Figure 4.11: Optical image of a patterned oxide layer damaged over the border of the etch.

We are now at the end of the fourth step of the process flow, as reported in Figure 4.1.

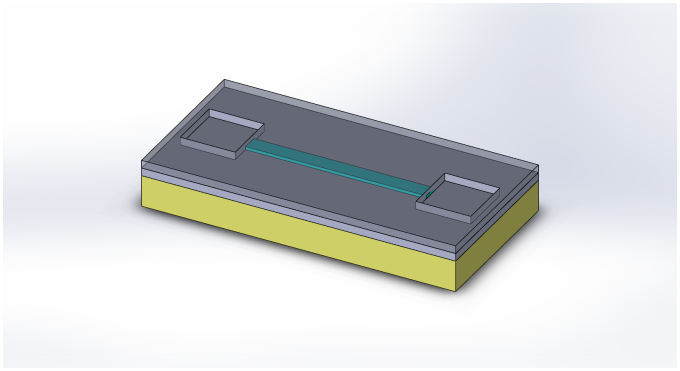

Figure 4.12: 4th step: Two openings are etched to allow access to sacrificial layer.

4.1.7 Releasing the channel

At this step, the opening of the nanochannel is available and the sacrificial layer can be released. Before proceed with the xenon difluoride etching step, a short etching with SF_6 is performed because it has been noticed that helps to have a faster and uniform etching in all regions of the wafers, very likely acting on the superficial layer of native oxide presents on the silicon. An example could be seen in picture 4.13 showing two devices of the same length undergone at the same etching in XeF_2 of 5 pulses of 30 s: can be clearly seen that for the same process the device treated with the fluorine etching before experiences an etching more than twice faster.

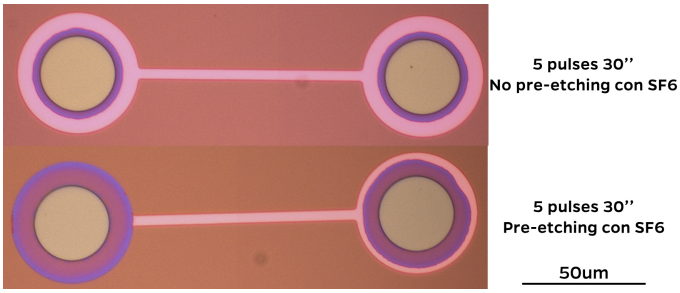

Figure 4.13: Difference in etching rate depending the SF_6 treatment.
Purple: etched Si - Pink: remaining Si

The tool used is the AMS200 with the recipe "Si Release", whose parameters can be seen in table 4.5. In this step the photoresist is still present on the wafer to preserve the oxide, anyway thanks to the high selectivity of SF_6 gas and the short duration of this step, the etching of the exposed oxide (the inlets region) is negligible.

The xenon difluoride (XeF_2) is a white crystalline solid with a vapor pressure at room temperature of about ~4.5 Torr, which means that, under vacuum conditions,

Power coil	Power plate	Substrate temperature
2000 W	0 W	30 °C
SF_6	C_4F_8	Pressure
300 sccm	0 sccm	100 mbar
Si Etching rate	SiO_2 Selectivity	Time
4 µm	200:1	45 s

Table 4.5: Parameters of "Si Release" recipe

it sublimates [56]. When the gas meets the surface of silicon it is first absorbed and then dissociates to xenon (Xe) and fluorine (F); the last one represents the main etchant agent in the process. The reaction happening is the following 4.2:

$$2\,XeF_2 + Si \longrightarrow 2\,Xe + SiF_4 \tag{4.2}$$

The etching happens without needing ion bombardment or external energy sources with a quite high etching rate and a very good selectivity with respect to silicon oxide [57]. The main limiting agent of the etching rate is the contact area between the etchant and the silicon, since all the other sub-reactions are spontaneous at room temperature [58].

To release the nanochannels/nanoslits this kind of procedure has been adopted because:

- The selectivity to the silicon oxide (structural layer) is over 1000:1 [59]. This is critical since the process takes very long time, especially to allow the molecules of gaseous XeF_2 reaching the silicon through the nano-opening.
- The silicon etching rate is high, making the diffusion of the gas the limiting step.
- The problems caused by wet etching, like the channel collapse due to the final drying or channel clogging because of by the byproduct of the etchant, are not present.

The tool is composed by a series of valves and pipes that link three chambers: an etching chamber, a pulsing chamber and a XeF_2 chamber. In addition is present a pump to remove the gases and a line of nitrogen gas. The etching process is composed by three steps:

1. An initial purging: a series of pulses of N_2 (normally 50) is first injected in the etching chamber and then pumped out. This is needed to remove all the humidity from the reactor; the presence of H_2O can bring to formation of HF vapor: hazardous for the users and unwanted because etchant of the oxide.

2. The pulsed injection of sublimated XeF_2. Here the user can play on three parameters: number of pulses, pressure of the chamber and duration of the pulses.

3. To finish the process another purging is done to completely remove all the XeF_2 and its byproducts that are hazardous for the users.

Unfortunately, the etching rate of this process is deeply variable and also in literature it is not present an established etching rate for the silicon. Furthermore, in my case, the limiting step was the diffusion of the gas reaching the silicon and so find the right recipe took to me some supplementary time. The parameters used can be seen in the table below 4.6.

Number of Pulses	Pressure	Duration
27	2700 mtorr	180 s

Table 4.6: Recipe for XeF_2 etching

To allow the exposed area to enter in contact with the XeF_2, the duration of the pulses has been elongated of six times compared to the standard one in CMi Lab (about 30 s). The inspection, to understand if the etching has worked (or not), with the nanoslit devices is easily done with an optical microscope looking for differences in color (and refractive index) along the channel as can be seen in figure 4.15. The scanning electron microscope has a too much low contrast between the etched and unetched parts to be used as check, as can be seen in figure 4.16. The case of nanochannel is more complex, because the features are too small to be inspected by optical microscope, so some expedients have been used that will be explained later in section 4.2.2.

When the channel releasing is complete, the photoresist is removed with a plasma oxygen treatment. We are now at the end of the fifth step of the process flow, as reported in Figure 4.1.

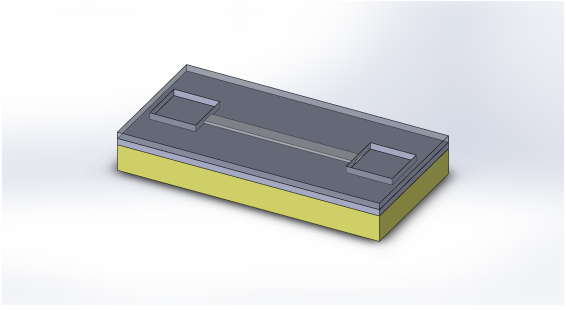

Figure 4.14: 5^{th} step: Sacrificial layer is etched with XeF_2.

The optimization steps done for this part of the process are reported later in this thesis, in chapter 4.5.2.

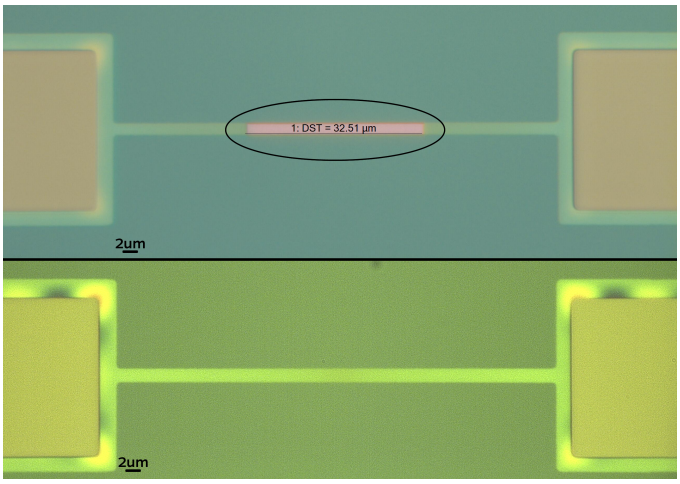

Figure 4.15: Optical inspection for the releasing of the channel: the top one has still 32 µm to be released, while the other is fully released.

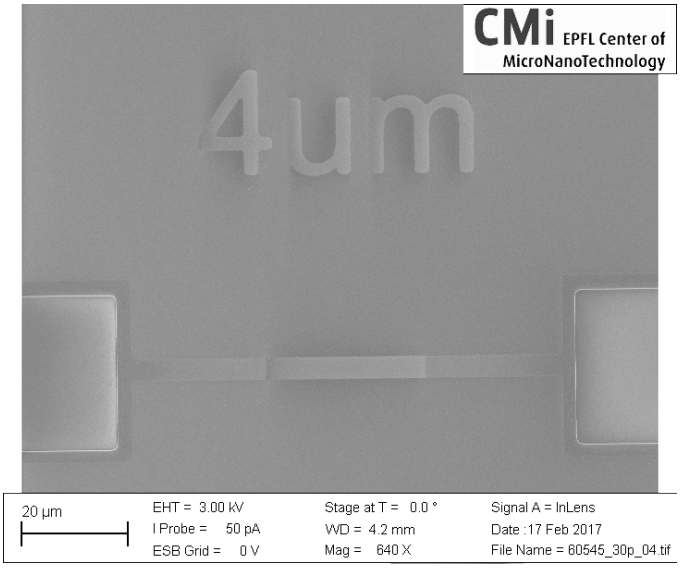

Figure 4.16: SEM picture of an unreleased channel of 4 µm width.

4.1.8 Structuring and releasing the bridge

To structure the bridge is necessary to open two lateral openings in the oxide and then remove the underlying bulk silicon to suspend the beam. A photolithography is done, with the standard steps: coating (ACS200 - AZ 1512 HS 1.1 µm), exposure (MLA150 - Dose 55 mJ/cm^2) and developing (ACS200). Part of the mask used is reported in figure 4.17.

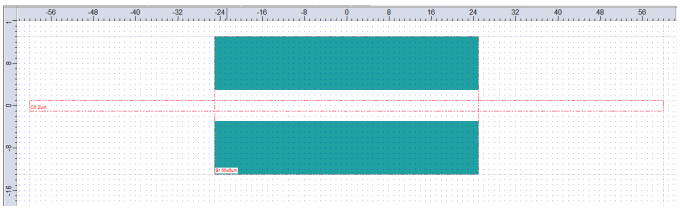

Figure 4.17: Part of the third lithographic mask.

The openings in the structural layer are done with the SPTS Advanced Plasma System (APS). The etch has to fully remove the 400 nm of silicon oxide. In this case, differently to the previous etchings, we are not worried in possible damages the underlying silicon because it will be anyway removed in the subsequent step. Thus, a non-selective recipe has been used: "SiO_2 PR 1:1". Parameters in table 4.7.

Power coil	Power plate	Substrate temperature
1200 W	300 W	10 °C
CHF_3	H_2	C_4F_8
15 sccm	0 sccm	0 sccm
SiO_2 Etching rate	Si Etching rate	Time
200 nm/m	95 nm/m	150 s

Table 4.7: Parameters of "SiO_2 PR 1:1" recipe

The distance between the apertures and their lengths define the dimensions of the single bridge, while the height is defined by the thickness of the double-deposited oxide layer. The width of the bridge is 2 µm larger, per side, than the internal channel to fit the tolerance of the photolithographic resolution and alignment error: from 6 µm to 9 µm. The length, instead, is the same for every device: 50 µm.

To finally suspend the bridge, the isotropic proprieties of the SF_6 etching are used. The XeF_2 was also an option to accomplish this step, but a more governable process has been preferred to avoid bigger underetch than required. The etching, in fact, occurs in all directions and thus, also towards the silicon under the zone of

clamping of the beams that, if removed, would add non-idealities to their behavior (and this is unwanted).

The critical dimension that determine the etching time, in this step, is the largest width of the bridges: 9 µm. The recipe used is again the "Si Release" (parameters in table 4.5); a calibration disclosed that the etching rate in lateral is about ~100 nm/s. Considering that the etching happens from the both sides of the bridges, an etching time of T = 45 s was adequate.

A final oxygen plasma etching is useful to remove the photoresist and clean the surface to get it ready to be bonded. We are now at the end of the third step of the process flow, as reported in Figure 4.1.

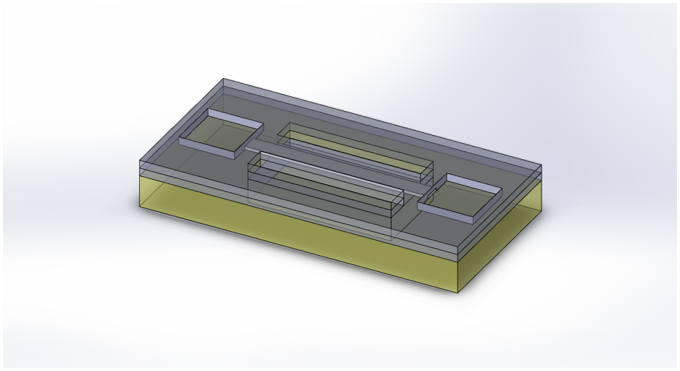

Figure 4.18: 6th step: Beams are defined and released.

Below is reported a picture of a released devices 4.19, other ones are reported in appendix A.

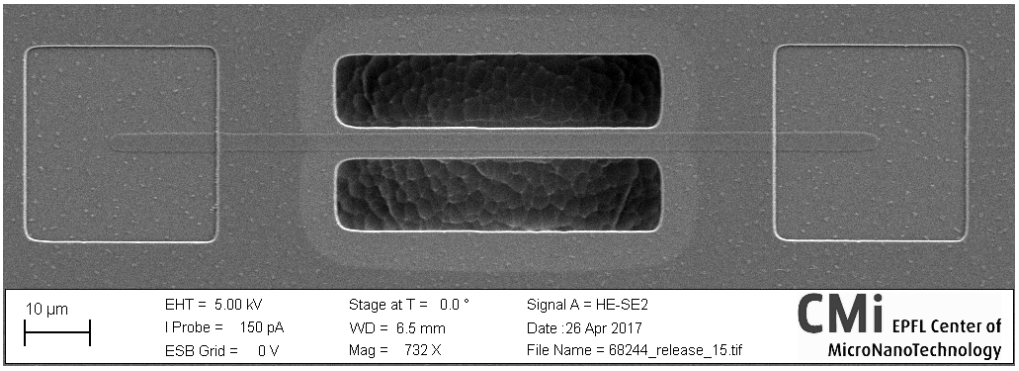

Figure 4.19: SEM picture of a released clamped-clamped beam

4.2 Nanochannel Device

The process flow for the Nanochannel devices is practically the same as the one explained so far for the Nanoslit, in section 4.1. The only step that changes is the photolithographic process, described in the paragraph 4.1.4. Here, since the dimensions of the channel go down to the nanometric scale a tool with more resolution is needed: an electron beam lithographic system.

4.2.1 E-Beam patterning of the sacrificial layer

To get features having the critical dimension down to the nanometer, in the patterning of sacrificial layer, the electron beam lithography has to be used: the Raith EBPG5000+. The concept of the e-beam lithography is the same of the optical-based one: a resist is spun on the wafer, patterned with the wanted geometry and then developed. In this case, the resist used is the Dow Corning HSQ (hydrogen silsesquioxane) XR1541 002, it is a negative resist with the highest resolution available on the market. Chemically, once exposed to the electron beam, it turns in SiO_2-like material which is highly appropriate as etch mask for Si etching.

To improve the adhesion of the HSQ, a surface oxygen plasma treatment (3 minutes - 600 watt) is done to remove impurities and water molecules. Then the resist is spun on the wafer using a spin coater at 5000 rpm to get a 30 nm thick layer of resist.

Before starting the exposure, two parameters have to be decided: the beam current and the dose. Those depend on the size of the features to draw, a common strategy to save time is to find two combinations: a high resolution one for the fine geometries (nanometric scale) and a low resolution one for the others (micrometric scale). In the table 4.8 are reported the combinations I used, decided after a dose test to check the most appropriate. In figure 4.20 is reported a sample of the features wrote for this process.

	Low Resolution	High Resolution
Dose	3000 µC/cm^2	6500 µC/cm^2
Beam Current	10 nA	0.2 nA

Table 4.8: E-beam parameters

The HSQ is then developed for 2 minutes in MF-CD 26, a TMAH based developer. Before continuing with the etching, an additional oxygen plasma is done to harden the SiO_2 created mask. After the patterning of the sacrificial layer, the mask will not be removed because there is no way to remove it without damaging the first structural oxide layer and an additional layer of less than 30 nm (since a

part of it has been anyway etched) over 400 nm is negligible in the total evaluation of the structure.

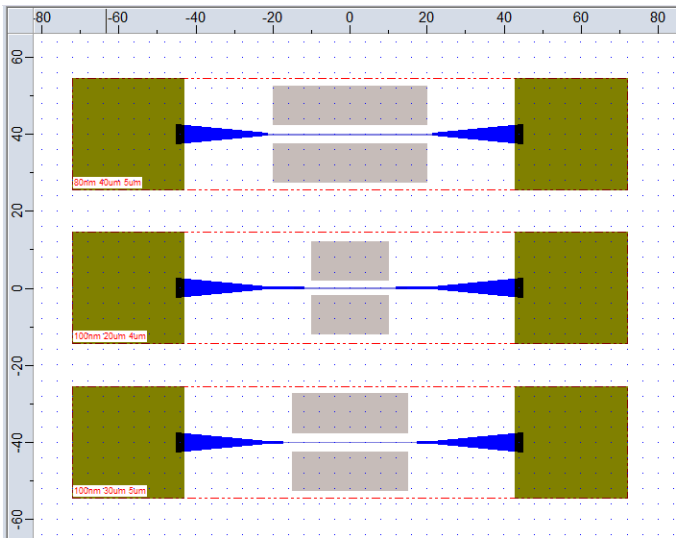

Figure 4.20: Part of the mask used for the nanochannel devices.

4.2.2 Releasing the nanochannels

The process adopted to release the nanochannel is based on the same principle (XeF_2 etching) of those used for nanoslit, explained in paragraph 4.1.7, with some differences. The first one is the duration of each pulse, increased from 180 second to 270 second since the conductance of the apertures to overcome is smaller with respect to the nanoslit case.

The second one is more a trick to facilitate the understating on the outcome of the etching process. In this case, since the channels are at the nanometric scale both in height than in width, thus is no more possible to inspect them by the use of an optical microscope to see the variation in contrast between the etched silicon and the unetched one. To overcome the issue, some trials with the EDX (Energy Dispersive X-ray) analysis were performed with a Zeiss Merlin SEM (scanning electron microscopy), but were impossible to discern the signal coming from the silicon sacrificial layer from the one originating from the bulk silicon making this technique not reliable to the purpose. To solve this problem some micrometric rectangles, playing as test structures, have been inserted in the middle of the channel. The mask used can be seen in Figure 4.21. The silicon of the pads was only accessible through the nanochannel and so, if they result etched, it means that all the nanochannels have been released.

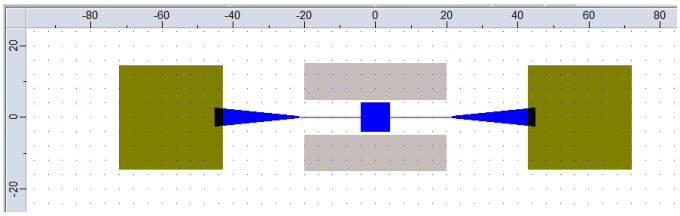

Figure 4.21: Mask used for the test structure in the nanochannel process.

Since the pads are at the micrometrics scale, it was again possible the optical inspection with the microscope to discern the result of the etch. At the end, increasing the time of the pulse duration, some pads resulted etched. In Figure 4.22 is reported the smallest channel in which is clearly visible an etching in the testing pad.

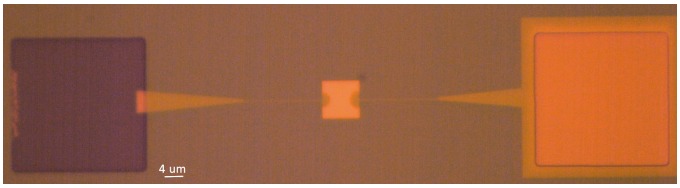

Figure 4.22: Smallest channel in which is clearly visible an etching in the testing pad for the nanochannel devices

.

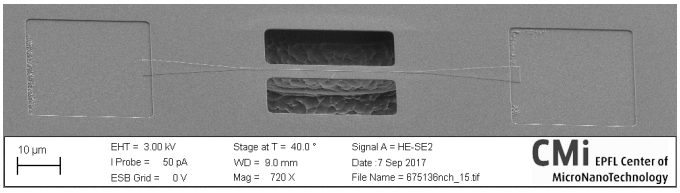

Figure 4.23: SEM image of a successful released nanochannel device.

4.3 2-Step Nanoslit Device

The changes of the process flow for the 2-step nanoslit devices consists in a repetition of the steps of deposition/patterning/etching of the sacrificial layer before been buried in the oxide, with the aim to have a feature with two different heights in silicon. All the other steps remain the same as the ones described for the normal nanoslit in section 4.1.
First is shaped the additional step in the sacrificial layer, right in the middle of where there will be the channel, with a normal photolithographic process (coating ACS200 - Exposure MLA150 - development ACS200).

The sizes drawn are:

- length: 10 µm;
- width: the width of the channel diminished of 500 nm by side.

The shrinking in width has been thought to avoid misalignments in the subsequent lithography: in this way this layer should be totally covered by the second one if the alignment is good.

So, the etching of the first sacrificial layer is carried out, with the same recipe "Si Opto HR" with 22 seconds of process, as done in 4.1.4, with the following plasma oxygen for the resist cleaning.

All the steps of process from now on is the same as the one described in the nanoslit section, starting from the second round of deposition/patterning/etching of the sacrificial layer, that in that case was the first one.
One important thing to be noticed is that the two rounds involving the sacrificial layer have to be completed in a narrow time window to limit, as far as possible, the formation of an oxide interface between the two silicon layers. This because the native oxide layer could lead to issues during the xenon difluoride releasing of the sacrificial layer.

4.4 Sealing

The sealing of the chip is performed with an anodic bonding of a glass wafer with patterned the microfluidics of interface and the vibrational cavity. The main functions of the patterned glass wafer are:

- protects the bridges from the external environment;
- acts as first interface for the fluidics: from the nanochannels toward a microchannels;
- separates the part defined for the liquids with respect to the one deputed to the vibrations.

Here I will explain the process used to model the glass wafer, based on an wet etching with hydrofluoridric acid (HF) for the microchannels and a powder blasting process for the through holes for the inlets. To start, the chosen material is Borofloat 33, a special glass material (of the family of Pyrex glass) with a composition that perfectly match the thermal expansion coefficient of silicon, which is essential for good bonding results (reference in figure 4.24). In fact, the low coefficient of linear thermal expansion allows borofloat glass wafers to easily handle elevated

temperatures and – often even more importantly - sudden thermal changes without breaking or warping. [60].

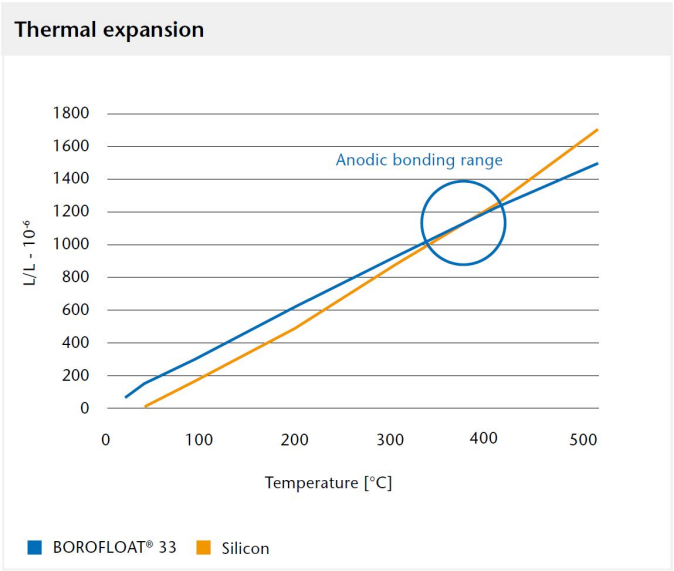

Figure 4.24: The thermal expansion coefficients of silicon and borofloat for the temperature of interest for anodic bonding. Picture from Schott Borofloat datasheet: [61].

4.4.1 Microchannels patterning

The easiest way to pattern the Pyrex is with a HF-based wet etching with a masking material reporting the wanted features. The masking could be done with a thick layer of photoresist or with a "hard mask", namely a HF-resistant metallic layer. I opted for the second option because it was the most protective toward the glass surface (a defect-free surface is fundamental for a good adhesion in the bonding process). A good material for this purpose is gold: it has a very good resistance with respect to the HF etch and can be easily removed from the glass. The drawback is that has a poor adhesion on the glass surface, to improve it a thin layer of Chrome has to be deposited between gold and glass surface (normally called "adhesion layer").

Before starting the process, a "Piranha cleaning" is done on the wafer. This solution, formed by 3 parts of concentrated sulfuric acid (H_2SO_4) and 1 part of hydrogen peroxide (H_2O_2) and heated at 100 °C, is very powerful in the removal of organics residues.

So the thin Cr-Au film is deposited on the wafer with the Alliance-Concept DP 650 (Sputter single chamber multi-target), a tool that allows to change the target in use without breaking the vacuum in the chamber and so without injecting contaminations between the two layers deposited. The used recipe is called "HTU 150 Cr-Au", that means a deposition at 150 °C with a good degree of uniformity of the layers around the wafer, with the target thicknesses of:

- Cr: 40 nm;
- Au: 250 nm.

After this, a photolithography and an etching steps are needed to draw in the metallic film the desired features. The photolithography is always done with the coating (ACS200), exposure (MLA150) and developing. A 2.0 µm layer of resist (AZ 1512 HS) has been used to help in protecting the surface. An exposition dose of 130 mJ/cm^2 has been found optimal to well-expose the resist. Then to finish, a contact time of 60 seconds during the developing step has been used.
To pattern the Cr-Au layer an ion beam etcher, the Nexus IBE350 from Veeco, has been used; this tool can etch any materials by pure physical sputtering, and so without chemistry dependence. It exploits Argon ions extracted from an ICP source, accelerated and directed to form a mono-energetic beam that hit the sample. This principle is very useful when you have to deal with an etch of a series of thin layers composed by different materials like in the case under exam.
To not stress too much the wafer, the deposited layer and the photoresist an intermediate recipe, called indeed "Medium", was used. A total time of 4 minutes and 30 seconds has been used to fully etch the metals, the parameters can be seen in the table 4.9. To avoid a self-sputtering of the materials on the edge of the resist, the wafer has been inclined of -10° with respect to the direction of the beam.

Beam Voltage	Beam Current	Angle
300 V	500 mA	-10°
Cr etching Rate	Au etching rate	Total time
42 nm/min	158 nm/min	270 s

Table 4.9: Parameters for IBE etching

At this step the wafer is now ready to be effectively structured with the microfluidic channels so it undergoes to a wet etching with HF. The process is done in a bath of HF(49%):H_2O 1:4 heated at 70 °C. The cavities should be around 20 µm in depth. A calibration has been done on a trial wafer finding an etching rate of about 1.20 µm/min. Using this number, we can estimate the duration needed to the process: 17 minutes. After that, the photoresist is removed using the Shipley

Remover 1165 (because of the presence of metals on the surface, the oxygen plasma is not advised). The metallic layer is not removed because from now on until the bonding, it will act as "protecting layer" for the surface of the wafers.

4.4.2 Through holes machining

To let an insertion of the fluids into the microchannels (and so in the nanochannels) some openings on the sealing wafer are needed. To do that four holes (called, from now on, inlets) through the all thickness of the wafer should be done; moreover an additional one has been done to be able to connect a pumping system to pump vacuum around the resonating devices. A top view of the chips, with the five holes, can be seen in Figure 4.25.

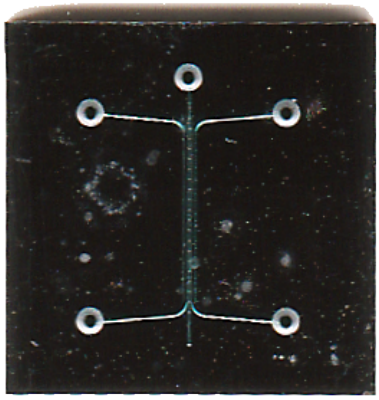

Figure 4.25: A top view of the glass chip.

Making through holes in glass, aligned with a pattern on the other side of the wafer, is not an easy task. There are mainly two ways that can be performed to achieve this result:

- A pure physical approach: powder blasting. The sand particles remove part of the base material using high pressure / velocity. The material is ablated only where the glass or silicon is not protected by a structured layer of resist.[62]
- A pure chemical approach: wet etching with hydrofluoridric acid (HF).

Both the methods were attempted, but in the end, the first one was chosen: it was cheaper, faster and safer with respect to the chemical approach, moreover also the holes were qualitatively better with the powder blasting. The only drawback, from a personally point-of-view, was that the process has been done from a company outside the CMi@EPFL cleanroom and so, for this part of the process, I does not have all the details of the process that it has been used.

Surface cleaning

All the features wanted on the wafer are present and so only the cleaning step remains before the final bonding. To remove the metals the wafer is dipped, repeatedly, in two different etching solutions: one for gold (composed by KI + I_2) and one for chromium (composed by $(NH_4)_2Ce(NO_3)_6$ + $HClO_4$).

4.4.3 Anodic bonding

To finally seal each chip, the two wafers machined with the processes for the devices and microfluidics cap have to be bonded. Considering that we have to bond a silicon wafer with a thin layer of oxide and a glass wafer, the most suitable approach is the anodic bonding. It ensure optimal sealing results also in presence of roughness on the surface [63], as in my case, due to the residual roughness of the etching and due to the nanometric steps originated from the sacrificial layer patterning. The bonding happens when a high DC voltage (400-1000 V) is established between the wafers (such that the glass is negatively biased with respect to silicon) in a high temperature environment (300-500 °C). Under these conditions, ions of the borofloat wafer are attracted toward the cathode and chemical reactions happen at the interface between the wafers causing a current flowing through the system until the bonding is completed. Layers deposited on the silicon surface have a detrimental effect on the quality of the bonding because the electrostatic pressure decreases with the increasing of oxide layers and so a smaller area of the wafers is in intimate contact. It has been found that the limit to obtain a good bond is below 600 nm of silicon oxide thickness [64]. In my case I have about 400 nm so below the limit, anyway a higher voltage with respect to the normal silicon-glass anodic bonding will be needed to compensate for the decreasing of electrostatic pressure.

Anyway, before undergo the bonding the wafers has to be well aligned: the central cavity right on the bridge, the lateral cavity (for the microfluidics) overlapped with the inlets of the channels of the bridge, as can be seen in figure 4.26. To do that a "Süss MA6/BA6", double side mask aligner and bond aligner with specific holders and chuck has been used.

The bonding is done in a "Süss SB6". The process starts with a slow heating ramp until the desired temperature of 450 °C, a "finger electrode" is placed right in the center of the wafers to create a first bonding point that immobilize the wafers and so its alignment. Then the spacers of the holder that were gripping the wafers are released and the bigger electrode can be used to complete bonding. A slow cooling ramp is then applied to come back to the environment temperature. Both the temperature ramp (warming and cooling) should be slow to not create thermal shock to the wafers. The voltages applied and the other parameters for my process can be seen in table 4.10 The optimization steps done for this part of the process are reported later in this thesis, in chapter 4.5.3

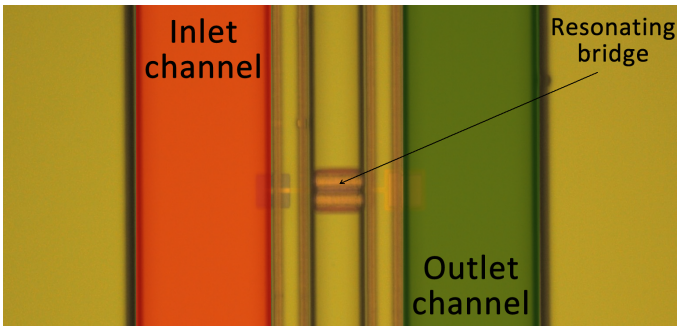

Figure 4.26: Successful alignment of sealing and devices wafers.

Voltage 1st Electrode	Voltage 2nd Electrode	Current Limit	Temperature
850 V	800 V	10 mA	450 °C

Table 4.10: Parameters for anodic bonding

To finish, the wafer is diced in chips of 10 mm x 10 mm that are ready to be characterized.

4.5 Optimization of the process

In this section all the optimizations to obtain working devices are reported: from the choice of the oxide toward the anodic bonding recipe mentioning also the tuning done in the xenon difluoride etching step.

4.5.1 Oxide material for structural layer

The first silicon oxide layer used in the process was the silicon oxide deposited via plasma enhanced chemical vapor deposition (PECVD). Its advantages were a high deposition rate and a cheap fee for the usage of the tool. A not-expensive approach is always preferable in the beginning. The oxide, anyway, revealed issues during the XeF_2 etching step: also the silicon covered by the oxide (and so theoretically unexposed to the etching agent) was attacked and removed. Apparently, the oxide was permeable to the etchant gas, this could be due to the low quality of the layer depending by the high deposition rate of the PECVD process.

Since the problem was mainly the removal of the bulk silicon during the channel releasing step, the idea to solve the problem was to use a wafer with grown wet silicon oxide (in principle of optimal quality from a point of view of density and absence of impurities) used as first oxide layer and then deposit a second layer of oxide with another technique.

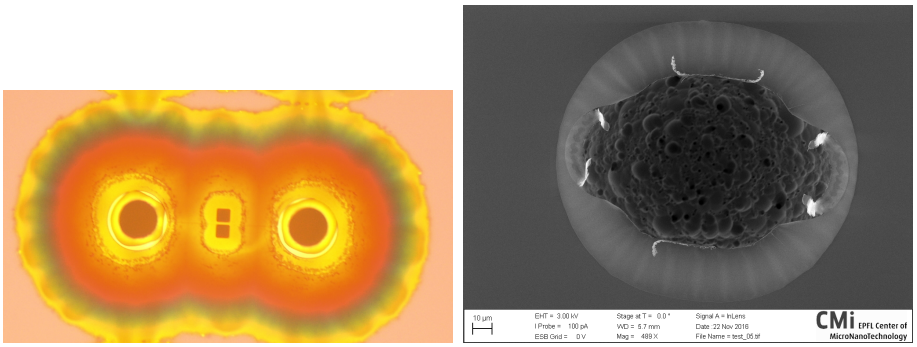

(a) Optical image (b) SEM image

Figure 4.27: Pictures of an unsuccessfully released devices with PECVD SiO_2 as structural layer

The first test in this way was done with silicon oxide deposited using a sputtering tool (Pfeiffer SPIDER 600). In principle the quality is lower with respect to PECVD oxide, but this tool was in the same clean room of all the other instrumentation and so there was a reducing of probability of injecting impurities due to the trip outside the clean environment done between the two laboratories. The sputtering, anyway, revealed itself inappropriate because of its low conformal coverage of the step. This time was the unexposed silicon of the sacrificial layer to be removed during the channel releasing step. Moreover, the sputtered silicon showed a very low consistency presenting delamination in the part interested by the channels.

The issue at this time was the solidity of the oxide, to solve it I decided to move toward the chemical vapor deposition process. This kind of processes occurs at higher temperature with respect to the previous ones and so ensure less impurities and higher compactness; the main drawback is the cost in terms of time (long process) and fee (expensive tool). The first one tested was the Low Thermal Oxide (LTO) CVD. The precursor of this process is the Silane (SiH_4) and the process happens between 400 °C and 450 °C. It was chosen a low temperature process to try to not inject too much thermal stress on the device, since it could have a detrimental effect on the overall performance of the resonator (i.e injecting compressive stress and so have a buckled beam). Also in this case, after the xenon difluoride etching step the top layer showed some delamination, although less serious than in the before case. To overcome this problem another CVD technique has been proven, this time with the tetraethoxysilane (TEOS) as precursor. This process has the advantages of a high conformal coating and a high solidity of the deposited layer. The process occurs at 700 °C with a subsequent annealing at the same temperature. In these conditions the layer get a low tensile stress that it is not detrimental for the mechanical proprieties of the resonator. This oxide layer, finally, does not show any kind of issues during the releasing step.

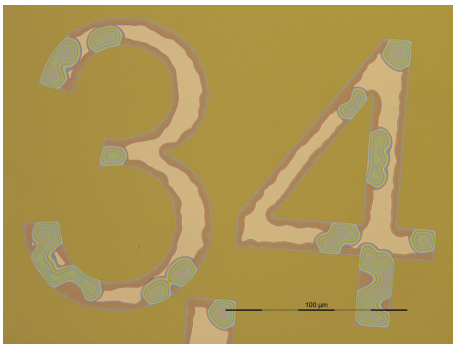

(a) Optical image of the etching in the unexposed sacrificial layer

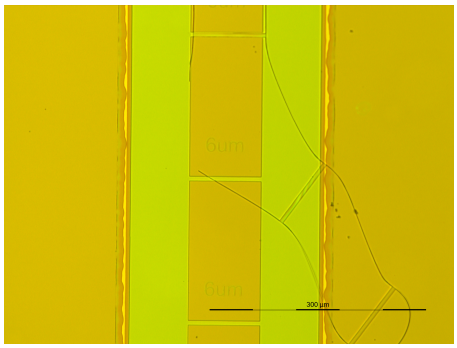

(b) Optical image of the delamination in the structural layer

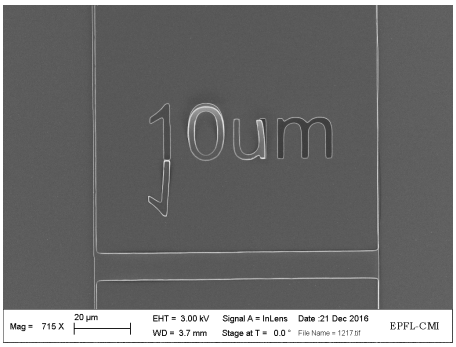

(c) SEM image of the delamination in the structural layer

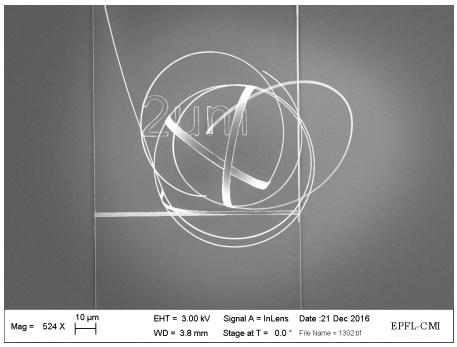

(d) SEM image of the delamination in the structural layer

Figure 4.28: Pictures of the issues met with the sputtered SiO_2 as structural layer

The first generation of the resonators was structured, as said above, with the bottom layer of thermal oxide and the top one of deposited oxide. Oxide grown by wet or dry oxidation of silicon are affected by a large compressive stress [65] causing a bending (or even a buckling) of the clamped-clamped beam having a detrimental effect on the mechanical proprieties. An example of a bent device can be seen in Figure 4.29, reporting a device from the first generation of chips with the bottom layer of grown thermal oxide and the second of TEOS CVD SiO_2.
The compressive stress causes a decreasing of the resonance frequency of the device [11] and so a lowering of the mass responsivity according to the equation 4.3, where f_r is the resonance frequency and m the mass of the resonator.

$$\Re_m = -\frac{1}{2}\frac{f_r}{m} \tag{4.3}$$

The effect of the stress on the resonance frequency can be modeled using the equation 4.4 [11]:

$$f_n = \frac{\beta_n^2}{2\pi}\sqrt{\frac{EI_y}{\rho A}}\sqrt{1+\frac{\sigma A}{EI_y\beta_n^2}} \tag{4.4}$$

where β_n represents the modal coefficient; E, I_y, A, ρ are respectively the Young's modulus, the geometric moment of inertia, the cross-section area and the density. The stress enters in account with the σ in the second square root: the tensile stress is defined positive and so increase the frequency; opposite happens when compressive stress is in play.

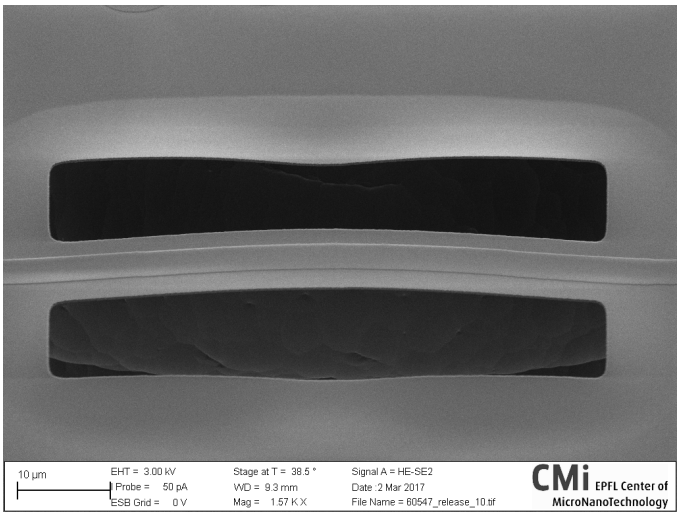

Figure 4.29: SEM pictures of a bent device of the first generation of chips with the bottom layer of grown thermal oxide and the second of TEOS CVD SiO_2.

4.5.2 XeF_2 etching process

The etching process with xenon difluoride occurs when the gas encounters the silicon and thus the following reaction happens:

$$2\,XeF_2 + Si \longrightarrow 2\,Xe + SiF_4$$

The peculiarity of this reaction is that as byproducts there are two gases and so easily movable (and removable) during a process; with liquid byproducts, considering the dimensions in play, it could takes long time to move it without using an external help as pressure or electric-based phenomena.
The quantity of etched material is directly proportional to the molecules of xenon difluoride encountering the silicon, so the etching rate depend by the number of molecules present in the chamber (so, being a gas, by the pressure) and from the area of contact between them. Not considering the contact area as limiting conditions, it is easy to understand that the etching rate is large when the XeF_2 is injected in the chamber and rapidly decrease when most of the molecules have already reacted with the silicon. This is the main reason why the most common tools adopt a pulsed etching approach: the byproducts are removed, and new etchant is

injected in the reaction chamber in each pulsed.
The available parameters are:

- Pressure in the chamber: directly linked to the number of molecules;
- Time of pulses: it must be bigger than the time needed to the gas to come into contact with the silicon;
- Number of pulses: related with the etching rate per pulse and the quantity of silicon to remove.

The usual recipe for the pulses is 2700 mtorr as pressure and duration that last between 30 s and 60 s. Several trials have been done using these parameters and the etching was not satisfying. In fact, the narrow apertures (and their low conductance) between the silicon and the chamber represent a limiting agent for the etching rate. After several tests, the optimal duration time was found to be 180 s. The number of pulses in a range between 27-30.
Another problem was represented by the fact that the edge of the wafer was not covered uniformly by silicon oxide (deposited on both sides of the wafer during steps 4.1.2 and 4.1.5) and so etched by the XeF_2 causing a decreasing of the useful etching rate and a ruined edge that can cause errors or damages to the clean room tools. A trick adopted to solve this was to cover all the edge of the wafer with Kapton tape in order to insulate it.

Since the sacrificial layer and the material to remove to suspend the beam were both silicon the process, in the beginning, was thought to have only two lithographic steps. One for the shaping of the sacrificial layer and one for the releasing. After some tests this idea has been abandoned and the two releasing steps have been separated adding a further lithographic step. It was not possible to proceed with the simultaneous releasing because the etching rate was to different because, as said above, it is strongly depended by the conductance of the apertures toward the material to remove: nanometric for the access toward the sacrificial layer and micrometric for the apertures next the beams toward the bulk silicon. In the end a further lithographic step was added, going from 2 to 3, and the final releasing of the beam has been done with the SF_6 to have a better control on the effective removed material.

4.5.3 Anodic Bonding

The bonding, in a first idea, should be performed under vacuum condition to have the vibrational cavity with a static low pressure, useful to improve the mechanical response (and the quality factor) of the beams. Some tests have been done to accomplish the process, using the standard recipe and varying some of the parameters, but each time a plasma discharging was happening in the chamber and

so a failure of the bonding. It was likely due to a combination between high voltage, low pressure and high resistance between the two wafer, causing a breakdown in the air medium.
Put aside the idea to have a static vacuum, the design had to be reinvented: a further hole on the glass wafer of sealing was added in order to allow the pumping out of the air in the vibrational cavity (bringing the number of holes on each chip from 4 to 5). In this way a low vacuum could be reached using a pump with an appropriate chip connector and some O-rings to prevent leakages.

Furthermore the anodic bonding between Pyrex and silicon induces, as side effect, a tensile stress at the bonding interface (and so on the silicon surface)[60]. As said above, in the paragraph on the optimization of the oxide material 4.5.1, this condition help to increase the mass responsivity of the resonators (as can be seen from the equation 4.4 and 4.3).

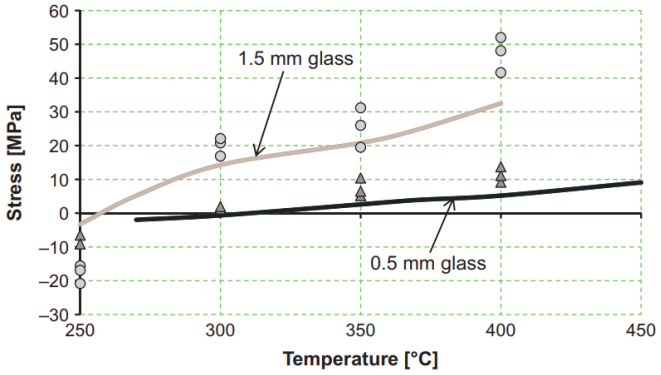

Figure 4.30: The residual stress in silicon at the bond interface as a function of the bonding temperature (bonding at 1000 V). Picture courtesy of [63]

Chapter 5

Experimental Setup

In this chapter the experimental instrumentation adopted to characterize the resonating clamped-clamped beams is described. The main tool used for this purpose has been the Polytec MSA-500 (MicroSystem Analyser). The instrument is able to measure the frequency spectrum of vibrating resonance using a Laser Doppler Vibrometer (LDV). It is usually combined with an external actuator and a pump system for vacuum. Furthermore, some measurements were performed with a lock-in amplifier (UHFLI from Zurich Instruments) to characterize the frequency noise. For the injection of liquids, a chip connector has been designed and produced to allow the linkage of the external fluidic circuit made by syringes and pipes with the inlets on the glass lid of the chips.

5.1 Mechanical Characterization: Laser Doppler Vibrometer

The LDV is a powerful instrument able to measure the frequency response of vibrating objects with a very high precision and flexibility. In this thesis the resonance frequencies were measured in a bandwidth of 2 MHz with a sampling resolution from 5 to 20 Hz (depending on the "FFT Lines" used, as explained in 3), anyway the tool can go up to 20 MHz maintaining the precision of the order of part per million. The working principle of the system is based on the Doppler effect: a frequency variation of radiation emitted by a source that occurs when the source is moving with respect to an external observer. The frequency of emission does not change, but a variation is experimented by the observer due to this effect, when the source is moving at a certain speed. An optical scheme of the detection system is reported in Figure 5.1. In the MSA-500 the light beam, generated by a laser source, is first divided into two beams by a beam splitter (the number 1 looking at the picture 5.1).
One is focused upon the resonator, while the other one is used as a reference and

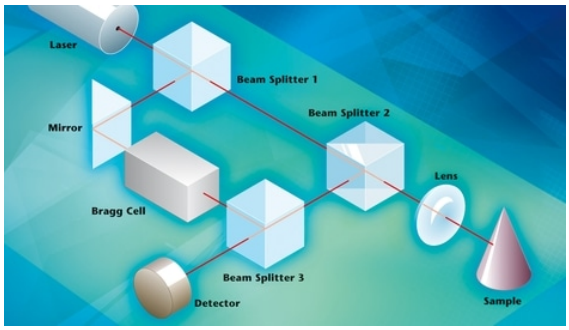

Figure 5.1: Scheme of the optical system inside the MSA-500 vibrometer, courtesy of Polytec Ltd.

it is directed towards the detector. When the first beam impinges on the resonator surface, part of the light is scattered and reflected back. Thanks to another beam splitter (the number 2 looking at the picture 5.1) this light portion is deviated towards the detector. So, the reflected light and reference beam interfere, originating a diffraction pattern. Fundamental here is the variation in the optical path length between the two beams, sensed as a frequency shift by the detector. In this way the system determines the vibration velocity of the moving part of the resonator. Moreover, a Bragg cell is introduced to add a frequency shift of 40 MHz that generates a typical interference pattern modulation frequency at the same frequency when the sample is at a standstill. Thus, if the object moves towards the interferometer the modulation frequency is increased, and if it moves far from the interferometer, the detector receives a frequency reduced with respect to 40 MHz. In this way it is possible to not only clearly detect the path length, but also the direction of movement too. The obtained signal, collected in time domain, is transferred in frequency domain using Fast Fourier Transform (FFT), so the frequency response is obtained. Measurements are handled using the software associated to the tool.

The system is completed by a mechanical actuator, a piezoelectric disk in my case, with the driving voltage generated by a signal generator integrated onto the MSA-500 tool. A pumping system is present for the characterization in vacuum, composed by the pair of rotative and turbomolecular pumps and by a vacuum chamber.

The obtained spectra are then elaborated with the help of OriginLab and/or Matlab to extract resonance frequencies and the quality factors. To obtain these two parameters, the peaks have been elaborated exploiting a Lorentzian fit approximation. In fact for slightly damped systems, the resulting power response of the resonator can be well approximated by a Lorentzian function f_L which is related to the Cauchy distribution [11].

Figure 5.2: Micro system analyzer tool (MSA-500) from Polytec Ltd.

The power response is proportional to the square of the resonator amplitude and so can be easily obtained acting on the output data of the laser Doppler vibrometer. The equation 5.1 report the Lorentzian function f_L:

$$f_L(\Omega, \omega, \Gamma, c) = c\frac{1}{4\Omega^2}\left[\frac{1}{(\Omega-\omega)^2 + (\frac{1}{2}\Gamma)^2}\right] \tag{5.1}$$

where c is a fit parameter and Γ is the full width at half maximum (FWHM) and ω the resonance frequency. The quality factor Q can be obtained dividing the resonance frequency by the -3 dB bandwidth. A comparison of the power response of a linear resonator to the corresponding Lorentzian fit is shown in Fig. 5.3.

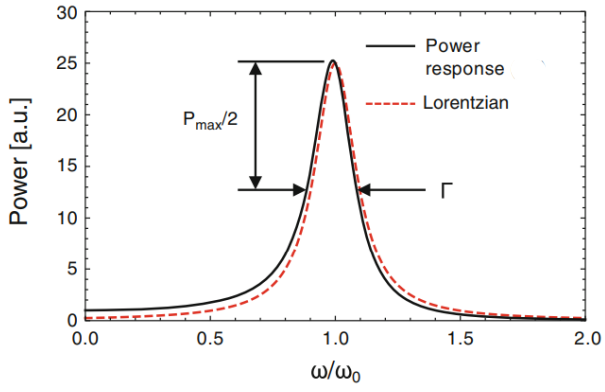

Figure 5.3: Comparison of the power response of a linear resonator to the Lorentzian function, courtesy of [11]

5.2 Microfluidic Interface

The fabricated chips, as can be seen in the picture 4.25, have five holes on the glass wafer (500 µm thick) used as inlets/outlets for the liquids and the vacuum system. Plugging in four tubes, without problems of clogging or spilling, directly on the chip were not feasible. So a chip connector, playing as interface between the holes on the chip and the external fluidic circuit, has been developed. A sketch of the connector is reported in figure 5.4a. It is composed by two different pieces: the top one with the fluidic connection and the bottom one with the housing for the piezoelectric actuation.
The top piece is characterized by five L-shaped conduits. They have on one termination a quick connector (LEGRIS 3101 04 09), used to easily plug and remove the pipes, and on the other one a groove with an O-ring, useful to avoid leakages of liquids towards the chip surface. There are also present five through holes needed for alignment with the respective inlet hole (on the chip) and a large central window to allow the optical access, essential for the characterization.
The bottom part has a round-shaped housing for the piezoelectric disk and a rectangular one for the electric cables. The depth of the piezoelectric disk housing is crucial since it is responsible of the sealing of the O-ring (and of the breakage of the ceramic actuator if too small).

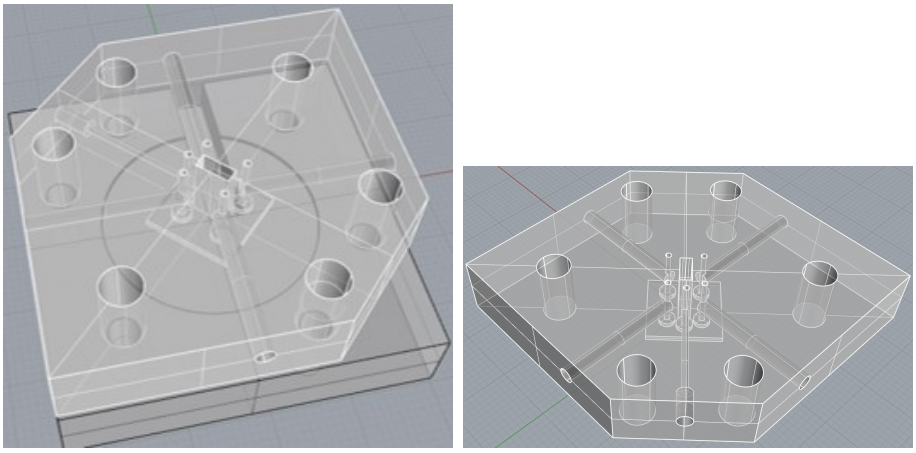

(a) (b)

Figure 5.4: a) Schematic of the chip holder b) Schematic of the top piece

The two pieces are then tight together with six screws to get the sealing of all the O-rings and to get the adherence of the chip on the actuator. Better is the adherence, cleaner is the signal obtained from the beams and higher is the signal to noise ratio.

The top piece, due to its complexity, has been produced using a 3D-printing technique (the distance between the O-ring grooves is around 300 µm), while the bottom one is fabricated with a numeric controlled milling machine.

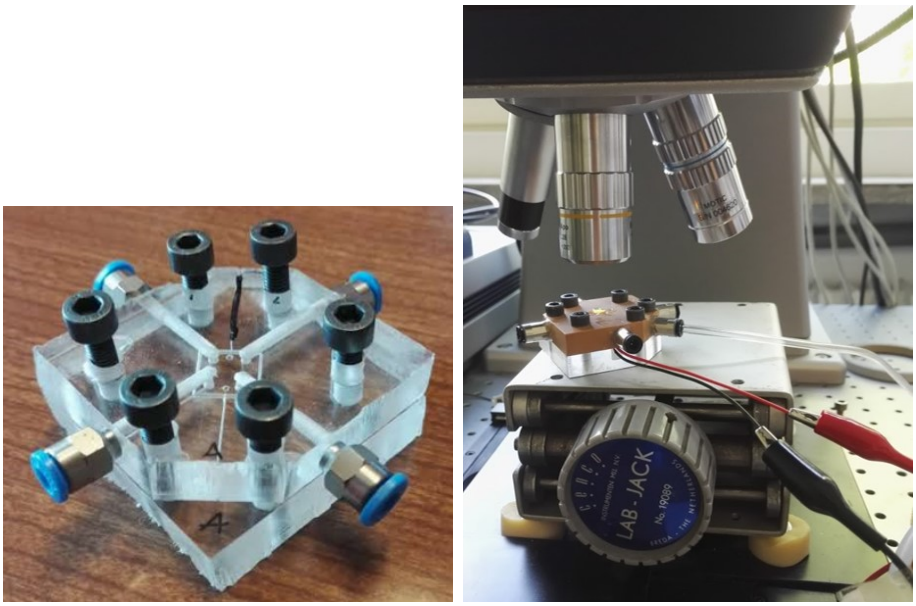

(a) Prototype done in PMMA with drill and milling machine

(b) Chip holder on the stage during a characterization

Figure 5.5: Pictures of the chip connector

5.3 Allan Deviation

The Allan deviation, named after its inventor Allan [66, 67], is an indicator used typically as a metric for the frequency noise of the sensors. In principle this calculation can be applied to any magnitude; for the oscillation frequency of an oscillator in a time period of τ is defined as 5.2:

$$\sigma_A(\tau) = \sqrt{\sigma_A^2(\tau)} \approx \sqrt{\frac{1}{2(N-1)} \sum_{k=2}^{N} \left(\frac{\bar{f}_k - \bar{f}_{k-1}}{f_0} \right)^2} \tag{5.2}$$

where $\bar{f}_k$ is the time average of the frequency measurement in the k^{th} time interval of τ within a total of N intervals, and f_0 is the mean oscillation frequency calculated over the entire duration of the noise measurement. In other words, the Allan deviation is calculated by averaging subsequent sections of the normalized frequency data of length τ, and then taking the difference between the means of contiguous segments [35]. The typical Allan deviation plot, as a function of the integration time τ, is reported in figure 5.6.

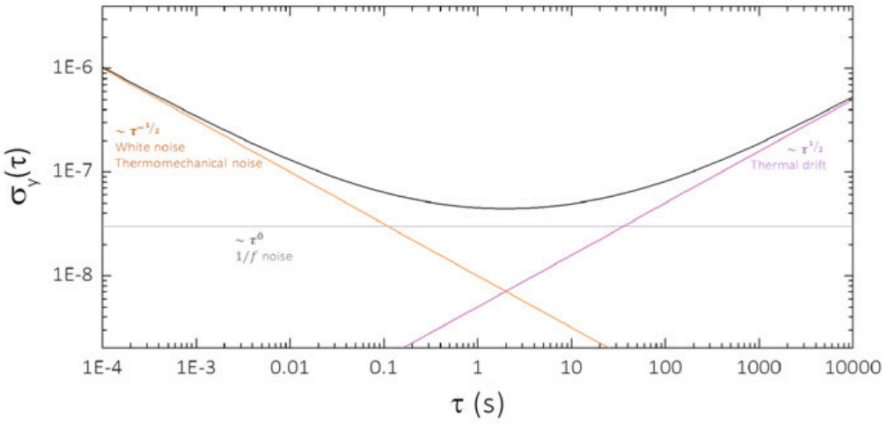

Figure 5.6: Typical Allan deviation plot as function of the integration time τ (black line), courtesy of [11]

As can be seen in the plot, the curve of the Allan deviation can be divided in three parts: a descending part, a "flat" region with a minimum and an ascending part. All the regions are characterized by a main contribution acting in that specific integration time, that define its overall behavior. The first contributors that we can find are the white noise and thermomechanical noise, which are inversely proportional to $\sqrt{\tau}$ and are represented with the orange line. The flat region is influenced mainly by the $1/f$ noise (represented with the grey line), with such noise source it is not possible to improve the measurement by averaging longer.

Then the last noise input, reported with the pink line, is the drift (or random walk) that increase proportional to $\tau^{1/2}$ or τ (in the plot is reported $\tau^{1/2}$). The minimum in the plot gives the parameter to estimate the lower limit of the frequency noise, and so the minimum achievable resolution when measuring the resonant frequency. Furthermore assuming that the minimum detectable frequency change is that one which gives a fractional change equal to the Allan deviation, we can estimate the minimum detectable mass by the resonator as [68]:

$$\frac{\partial m}{m} = 2\frac{\partial f}{f} = 2\sigma_a \rightarrow \partial m = 2\sigma_a * m \tag{5.3}$$

The tool used for the measurement of the frequency stability is the UHFLI from Zurich Instruments reported in figure 5.8, a lock-in amplifier, used in the PLL (Phase Locked Loop) configuration. A phase locked loop consists of a phase detector, voltage controlled oscillator and a loop filter as well as a reference signal source. A schematic of the circuit is reported in Figure 5.7.

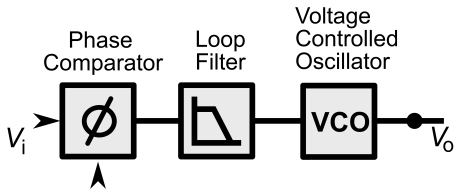

Figure 5.7: Simplest analog PLL (phase locked loop)

The oscillator generates a periodic signal, the phase detector compares the phase of that signal with the phase of the input periodic signal, adjusting the oscillator to keep the phases matched. Keeping the input and output phase in a lock step also implies keeping the input and output frequencies the same, or better be able to "follow" the frequencies within a predetermined bandwidth. In this way, giving as input of the system the phase of the oscillator at its resonance frequency, it is possible to continuously characterize the fluctuation of the resonance frequency, thus its noise (or stability) needed to calculate the Allan deviation.

Figure 5.8: UHFLI from Zurich Instruments

Chapter 6

Results

The characterizations did on the devices can be divided mainly in three parts:

1. A first mechanical characterization in which the performance of the devices is analyzed only from the point of view of the resonator to understand the values of the resonance frequencies and the limits regarding the quality factor.

2. A very rough fluidic check is performed to understand if the liquid can spill into the channels, or not. It was not possible doing this check using the visual inspection since the differences in refraction, or contrast, occurring in a 50 nm thick channels were not appreciable. Thus, it was used an electrical approach based on the injection of a conductive liquid into the channels with a subsequent I-V characterization.

3. A full characterization, combining the mechanical and fluidics parts, has been carried out injecting liquids with different densities in the chip and the respective shifts in the resonance frequency have been evaluated. At this step also a density and mass responsivities have been extrapolated from the density vs frequency resonance plot.

6.1 Mechanical Characterization

The mechanical characterization is needed in order to understand the values of the resonance frequencies and the limits regarding the quality factor. The first ones are useful to figure out the accordance between the estimation of the simulations and the output of the fabrication. The information on the quality factor, instead, give an idea of the goodness of the resonator, as said previous in this thesis 2.4.

6.1.1 Nanoslit devices

The nanoslit devices were the first to be produced, thus are the ones in which a deeper characterization has been possible. The measurements have been extensively done on different bridges belonging to different chips in order to understand the overall yield of the fabrication process. For all both the performance in air and vacuum have been investigated.

Here I report the result obtained on some chips (15 and 59) belonging to the first batch of chips fabricated. Results belonging to other chips are here omitted because do not give additional information.

Chip 15

In the plot 6.1 are reported two examples of characterization done on the first bridge (enumerated starting from the top of the chip, location of the identification number of the chip) in air and vacuum condition. It can be easily seen that, when the chip is put in high vacuum condition (a turbomolecular pump is used here), the resonance frequency increases and the broadness of the peak is strongly reduced. The first effect is due to the absence of the air acting as added mass during the vibration of the resonator, while the second one is due to the reduction of damping, resulting in a reduction of the energy lost during the vibration and thus an increase of the quality factor.

Condition	Resonance Frequency	Quality factor
Air	1.541 78 MHz	332
Vacuum	1.835 98 MHz	12352

Table 6.1: Resonance frequencies and quality factors for bridge 1 chip 15

The quality factor of the resonator is very high in vacuum condition and acceptable in air environment, giving a positive opinion on the yield of the process. It has to be noticed that the resonance frequency of the resonator is higher with respect to the expected one reported in the design section of this thesis, in the table 3.1. An explanation on this fact will be given later in this section, in 6.1.2.

Other characterizations on the same bridge of chip 15 have been done and are reported in the picture 6.3. All the characterizations reported in the figure 6.3 have been done without turn off the pump in a 24 hours temporal window. As can be seen the resonance frequency present a drift toward higher value. For the moment straight after the ignition of the vacuum pump, this variation is explainable with a transition between the air and the vacuum conditions, thus a reduction of "air added mass/damping" causing the increase of the frequency.

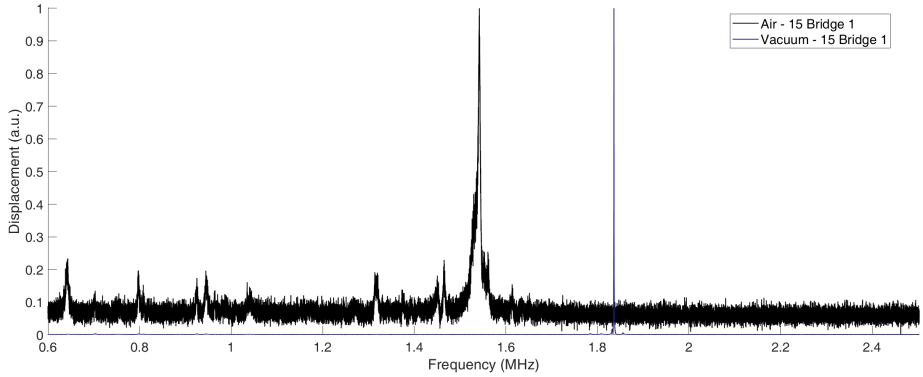

Figure 6.1: Two examples of characterizations done on chip 15 - bridge 1 (L x W x T = 50 µm x 6 µm x 450 nm: black line in air, blue line in vacuum.

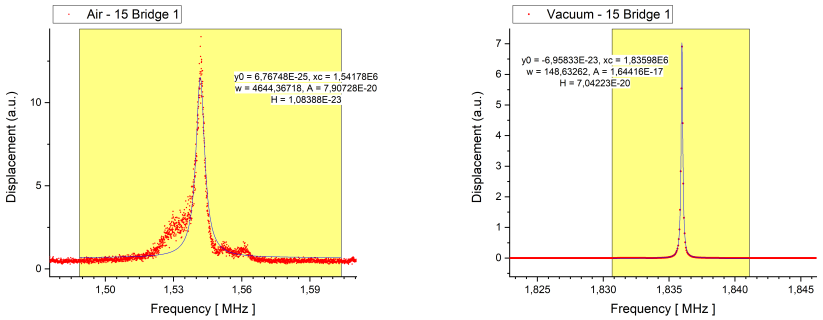

(a) Air (b) Vacuum

Figure 6.2: Lorentzian fit of the resonance peaks of the bridge 1 - chip 15. The blue line represents the fit while the yellow area the data interval of fitting.

The permanence of this drift also after some hours remains an unsolved point; different characterizations, reported later in the section 6.1.2, have been made trying to understand this phenomena.

Same characterization with analogous results are here reported for different bridges belonging to the same chip.

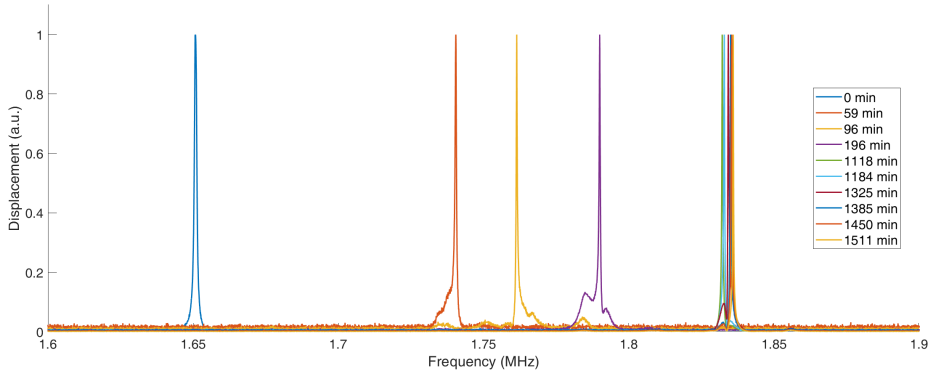

Figure 6.3: Characterizations made on the same device (Bridge 1 chip 15) in a 24-hours temporal window.

Measurement	f_r	QF	Δf_r w.r.t. Air	ΔQF w.r.t. Air
Air	1.541 780 MHz	332	0.00%	0.00%
Vac - 0 min	1.650 820 MHz	2775	7.07%	736%
Vac - 59 min	1.740 430 MHz	4734	12.88%	1326%
Vac - 96 min	1.761 430 MHz	6551	14.25%	1873%
Vac - 196 min	1.789 980 MHz	6338	16.10%	1809%
Vac - 1118 min	1.832 200 MHz	8653	18.84%	2507%
Vac - 1184 min	1.832 890 MHz	7571	18.88%	2181%
Vac - 1325 min	1.834 290 MHz	7069	18.97%	2030%
Vac - 1385 min	1.835 080 MHz	9442	19.02%	2744%
Vac - 1450 min	1.835 430 MHz	6577	19.05%	1881%
Vac - 1511 min	1.835 980 MHz	12352	19.08%	3635%

Table 6.2: Resonance frequencies (f_r) and quality factors (QF) for bridge 1 chip 15 of the characterization reported in 6.3. The variations are calculated with respect to air measurement reported in first row.

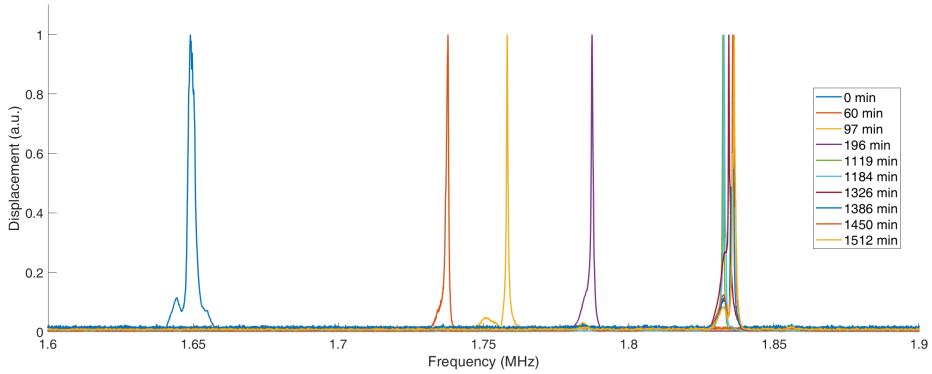

Figure 6.4: Characterizations made on bridge 2 chip 15. All the characterizations have been done without turn off the pump in a 24h temporal window.

Measurement	f_r	QF	Δf_r w.r.t. Air	ΔQF w.r.t. Air
Air	1.465 10 MHz	325	0.00%	0.00%
Vac - 0 min	1.649 32 MHz	1008	12.57%	210%
Vac - 60 min	1.737 63 MHz	3104	18.60%	855%
Vac - 97 min	1.758 15 MHz	5182	20.00%	1494%
Vac - 196 min	1.787 37 MHz	4088	22.00%	1157%
Vac - 1119 min	1.832 44 MHz	6547	25.07%	1913%
Vac - 1184 min	1.832 83 MHz	5736	25.10%	1664%
Vac - 1326 min	1.834 48 MHz	5341	25.21%	1543%
Vac - 1386 min	1.835 97 MHz	4634	25.31%	1325%
Vac - 1450 min	1.836 03 MHz	2477	25.32%	662%
Vac - 1512 min	1.836 29 MHz	3643	25.34%	1020%

Table 6.3: Resonance frequencies (f_r) and quality factors (QF) for bridge 2 chip 15 of the characterization reported in 6.4. The variations are calculated with respect to Air measurement reported in first row.

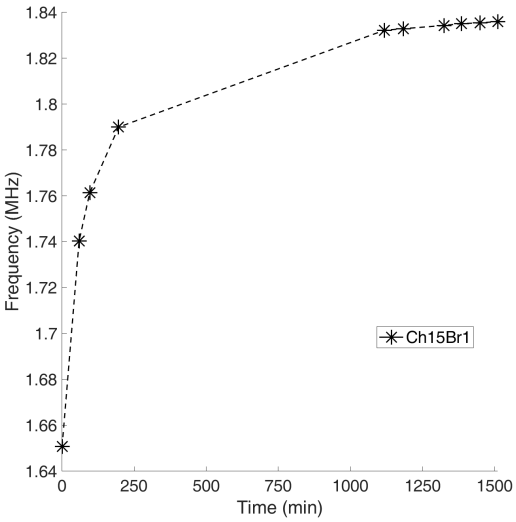

(a) Bridge 1 Chip 15

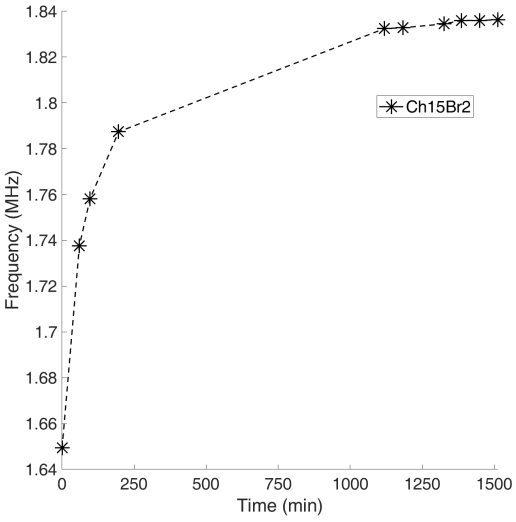

(b) Bridge 2 Chip 15

Figure 6.5: Evolution of the resonance frequencies versus time of bridges of chip 15

Chip 59

Here below are reported some characterizations done on another chip, identified with the number 59, showing the same behavior belonging to the chip 15, above explained. The first example of results are the measurements did on bridge 4 (L x W x T = 50 µm x 6 µm x 450 nm) and then the one on bridge 8 (L x W x T = 50 µm x 7 µm x 450 nm).

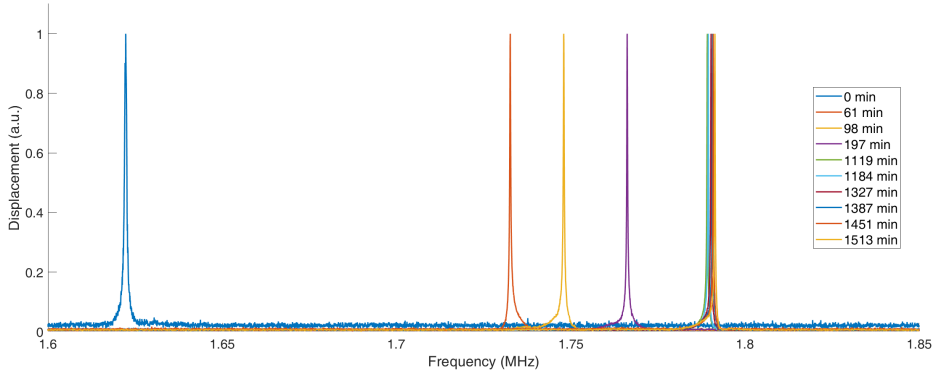

Figure 6.6: Characterizations made on bridge 4 chip 59. All the characterizations have been done without turn off the pump in a 24h temporal window.

Measurement	f_r	QF	Δf_r w.r.t. Air	ΔQF w.r.t. Air
Air	1.410 61 MHz	152	0.00 %	0.00 %
Vac - 0 min	1.622 30 MHz	3141	15.01 %	1964 %
Vac - 61 min	1.732 65 MHz	8110	22.83 %	5228 %
Vac - 98 min	1.748 02 MHz	8429	23.92 %	5438 %
Vac - 197 min	1.766 22 MHz	9494	25.21 %	6137 %
Vac - 1119 min	1.789 19 MHz	12614	26.84 %	8188 %
Vac - 1184 min	1.789 49 MHz	13734	26.86 %	8923 %
Vac - 1327 min	1.790 27 MHz	13601	26.91 %	8836 %
Vac - 1387 min	1.790 72 MHz	13749	26.95 %	8933 %
Vac - 1451 min	1.790 92 MHz	13242	26.96 %	8600 %
Vac - 1513 min	1.791 41 MHz	13053	27.00 %	8476 %

Table 6.4: Resonance frequencies (f_r) and quality factors (QF) for bridge 4 chip 59 of the characterization reported in 6.6. The variations are calculated with respect to Air measurement reported in first row.

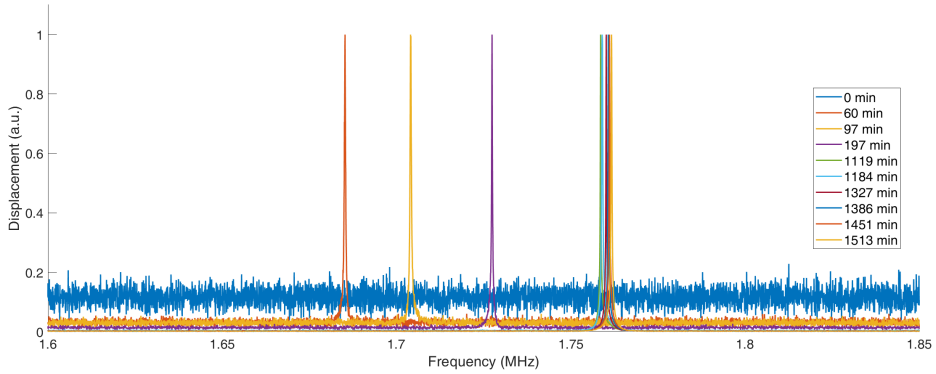

Figure 6.7: Characterizations made on bridge 8 chip 59. All the characterizations have been done without turn off the pump in a 24h temporal window.

Measurement	f_r	QF	Δf_r w.r.t. Air	ΔQF w.r.t. Air
Air	1.465 37 MHz	219	0,00 %	0 %
Vac - 0 min	1.570 33 MHz	3181	7,16 %	1352 %
Vac - 60 min	1.685 23 MHz	6135	15,00 %	2699 %
Vac - 97 min	1.704 09 MHz	5976	16,29 %	2627 %
Vac - 197 min	1.727 44 MHz	10315	17,88 %	4607 %
Vac - 1119 min	1.758 59 MHz	13374	20,01 %	6002 %
Vac - 1184 min	1.759 06 MHz	7355	20,04 %	3256 %
Vac - 1327 min	1.760 21 MHz	13588	20,12 %	6100 %
Vac - 1386 min	1.760 79 MHz	13739	20,16 %	6169 %
Vac - 1451 min	1.761 13 MHz	12006	20,18 %	5378 %
Vac - 1513 min	1.761 72 MHz	8626	20,22 %	3836 %

Table 6.5: Resonance frequencies (f_r) and quality factors (QF) for bridge 8 chip 59 of the characterization reported in 6.6. The variations are calculated with respect to Air measurement reported in first row.

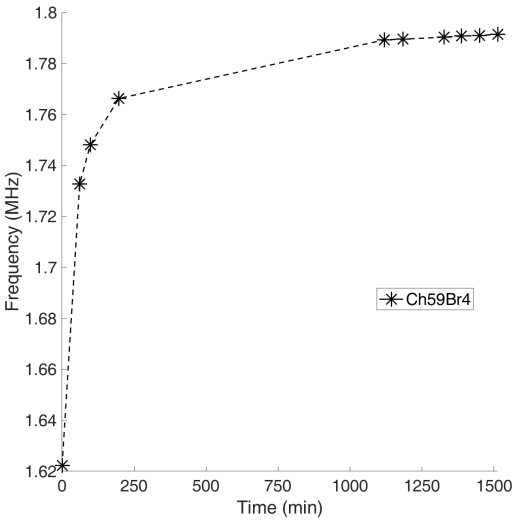

(a) Bridge 4 Chip 59

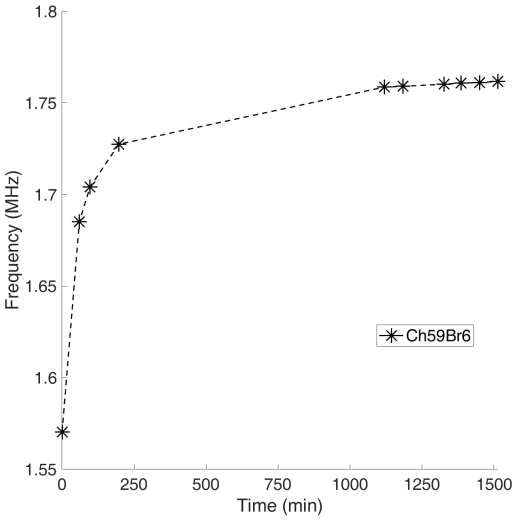

(b) Bridge 8 Chip 59

Figure 6.8: Evolution of the resonance frequencies versus time of bridges of chip 59

6.1.2 Drift of the resonance frequency under vacuum condition

A common issue found in every characterization made on the chips is the drift of the resonance frequency toward higher values when put and kept under vacuum. As said above, for the increase that occurs on the moment straight after the ignition of the vacuum pump the explanation can be a transition between the air and the vacuum conditions, thus a reduction of "air added mass/damping" and the consequent increase in resonance frequency. In fact, the turbomolecular pump reach the full speed after a couple of minutes thanks to the small volume of the vacuum chamber in which the tests are performed (about 5 L). Values of the vacuum pressure are not available due to the absence of a sensor, but it can be estimated that the pressure reach the high vacuum regime (about 10^{-5} mbar–10^{-6} mbar) at the full speed of the pump.
The unexpected fact is that the increase in the resonance frequency was not stopping, rather it was lasting for several hours. To better understand the phenomena, long duration (2 days) characterizations have been set up, helped by a macro on the tool that was able to repetitively start a measurement on prefixed points after an interval of time. These characterizations were meant to be useful to find the bandwidth of variation and, if present, a saturation time in which the drift was stopping.

Here are reported the figures of merit of one of these characterizations, lasted 41 hours with measurements about every 30 minutes. Since the measurement were done in absence of the operator the system was not continuously optimized to get the best signal (the XY stage of the tool was slowly moving due the pumping system, the prefixed points should have been adapted). In the picture 6.9 is reported the evolution of the resonance frequency versus the elapsed time, the overall variation is of 252.970 kHz (more than 15% with respect to the initial frequency). A so big shift in resonance frequency it is not easy to explain. The expected shift due to the removal of the air and some layers of adsorbed water on the surface would be much lower than 1 kHz (about 0.05 kHz), even considering the channel full of water the shift would be only some tens of kilohertz. The picture 6.10 reports the value of quality factor along the characterization, here can be seen that the evolution walk along a not-monotonic path.

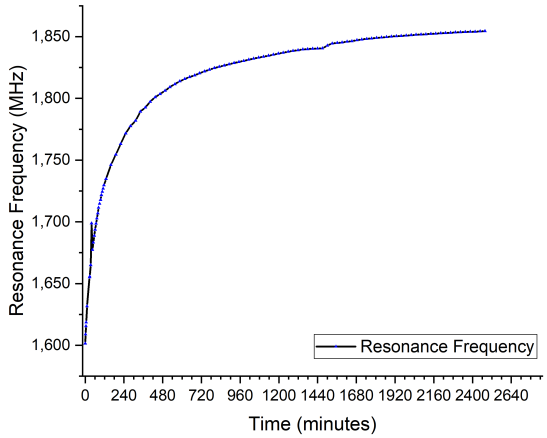

Figure 6.9: Resonance frequencies of a clamped-clamped beam put under vacuum versus the elapsed time. As can be seen the values of resonance frequency are increasing along the time: a high slope at the beginning and a saturation region in the end can be seen.

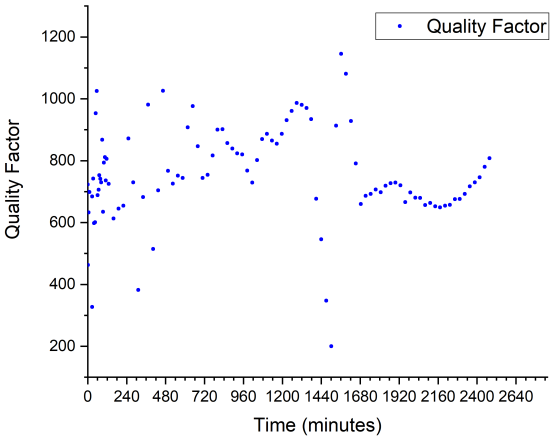

Figure 6.10: Quality Factor of the resonance frequency a clamped-clamped beam put under vacuum versus the elapsed time. As can be seen the evolution of the QF walk along a not-monotonic path.

The trend of the resonance frequency in picture 6.9 suggests that, after a certain interval of time, it occurs a saturation. The plot in picture 6.11 reports in detail the variation of the drifting velocity in absolute terms in Hz/s, i.e. the ratio of the differences of resonance frequency/time of the k-th measurement and the initial one $V_k = (f_k - f_0)/(t_k - t_0)$. The velocity, anyway, has been considered too high to be neglected for the fluidic characterizations. Moreover, the settling time had a timescale of tens of hours, too much to allow reproducible and repeatable characterizations.
Several hypothesis have been formulated trying to understand and to explain this phenomena. The most probable one was to consider the fact that during the deposition of silicon oxide via TEOS CVD some ethanol-derived molecules are formed as byproduct on the active surface of deposition [69]. If the reaction occurs too fast some of this molecules could be encapsulated by the oxide. In environment atmosphere these molecules can evaporate and then be substituted by water ones present in the air, creating a sort of "nanoporous oxide" humidity-susceptible. Hence, when put under vacuum environment the water is slowly released, affecting the proprieties of the material over the time and so influencing the overall resonance frequency. A good way to assess this hypothesis could have been a test under different humidity conditions in air, however in our laboratory the instrumentation to perform this kind of characterization was not available. Another way could have been trying with another process of deposition, however also in this case it was not possible because the other available processes in the CMi@EPFL showed issues as reported in 4.5.1. Thus, we did not succeed in demonstrating it.

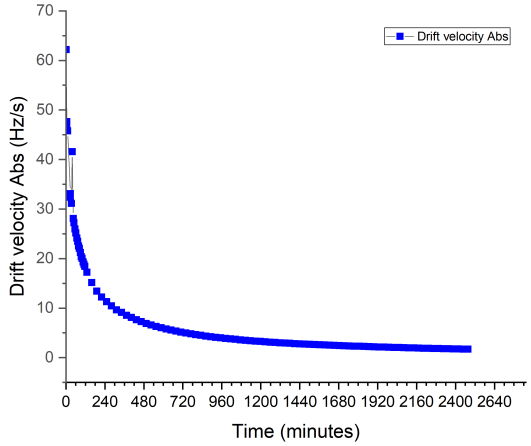

Figure 6.11: Absolute drift velocity versus the elapsed time. As can be seen, the drift velocity tends to saturate after a certain interval of time.

6.1.3 Effect of the residual stress on the resonance frequency

In all the characterizations performed, the measured resonance frequency was higher with respect to the theoretical one calculated with the formula described in the Theory section 2 and here reported 6.1.

$$f_n^0 = \frac{\beta^2}{2\pi}\sqrt{\frac{EI_y}{\rho A}} \tag{6.1}$$

where β_n represent the modal coefficient, E, I_y, A, ρ are respectively the Young's modulus, the geometric moment of inertia, the cross-section area and the density. To better visualize the difference, an example is reported in table 6.6 extrapolated from the Table 6.7.

Theoretical f_r	FEM f_r	Experimental f_r
0.9377 MHz	1.064 MHz	1.6003 MHz

Table 6.6: Differences between theoretical and experimental resonance frequency. Row extrapolated from table 6.7

The calculations done using the above formula 6.1 and the FEM simulations, during the design process (described in 3), had one limitation: residual stress, that could be present in the material, was not taken in account. Looking at the discrepancy present between the expected value and the experimental one, thus, it can be supposed that residual stress is present in the fabricated devices.
Analyzing the proposed fabrication process, the injection of residual stress is most probable in two crucial steps (as already highlighted in the fabrication part 4): the oxide deposition and the anodic bonding.
As reported in the theory section 2, the stress has the effect to change the resonance frequency with respect to the unstressed condition: when the stress is tensile the value increases, while if it is compressive the frequency have a reduction. The equation that take in account also the residual stress, explained in the 2.1.1, is here reported 6.2:

$$f_n = \frac{\beta_n^2}{2\pi}\sqrt{\frac{EI_y}{\rho A}}\sqrt{1+\frac{\sigma A}{EI_y\beta_n^2}} \rightarrow f_n = f_n^0\sqrt{1+\frac{\sigma A}{EI_y\beta_n^2}} \tag{6.2}$$

This equation presents a corrective term that take in account the residual stress with the term σ. The stress is conventionally set as positive when tensile and negative when compressive. Looking at equation 6.2 is easy to understand the effect of the corrective term on the frequency with respect to the unstressed condition (f_n^0).

Using the above formula 6.2 it was possible to extrapolate a value for the stress present on the presented devices. To calculate it, a Matlab cose has been wrote to solve equations with respect to σ on a series of characterization made on different bridges/chips. In table 6.7 a sample of them is reported.
The mean value obtained by the different characterizations is $\sigma = (11.27 \pm 0.82)\,\mathrm{MPa}$ referring to the expected resonance frequency obtained from FEM simulations, while $\sigma = (16.97 \pm 0.98)\,\mathrm{MPa}$ if referring to the theoretical resonance frequency. As can be seen in pictures 6.12 both the obtained values are consistent with the values found in literature for the stress due to anodic bonding and TEOS deposition.

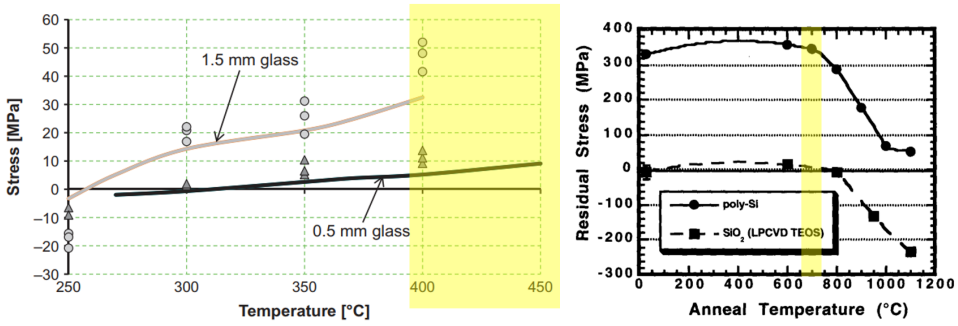

(a) (b)

Figure 6.12: (a) The residual stress in silicon at the bond interface as a function of the bonding temperature (bonding at 1000 V). Picture courtesy of [63] (b) Post anneal residual stress for 2.0 µm poly-Si and TEOS. Picture courtesy of [70].
In both the plots the highlighted the part is referring to the conditions applied in the process flow.

Identifier	$f_{Analytic}$	f_{FEM}	f_{real}	σ w.r.t. $f_{Analytic}$	σ w.r.t. f_{FEM}
1-0	0.9377 MHz	1.064 MHz	1.6003 MHz	16.17 MPa	10.65 MPa
2-a	0.9377 MHz	1.064 MHz	1.6365 MHz	17.30 MPa	11.52 MPa
3-b	0.9377 MHz	1.064 MHz	1.6381 MHz	17.35 MPa	11.56 MPa
4-c	0.9377 MHz	1.064 MHz	1.5789 MHz	15.52 MPa	10.14 MPa
5-d	0.9377 MHz	1.066 MHz	1.5925 MHz	15.93 MPa	10.39 MPa
6-e	0.9377 MHz	1.066 MHz	1.5884 MHz	15.81 MPa	10.29 MPa
22-10	0.9377 MHz	1.065 MHz	1.6747 MHz	18.51 MPa	12.44 MPa
d.pvd	0.9377 MHz	1.066 MHz	1.5727 MHz	15.33 MPa	9.923 MPa
e.pvd	0.9377 MHz	1.066 MHz	1.5932 MHz	15.95 MPa	10.40 MPa
e.pvd	0.9377 MHz	1.066 MHz	1.6156 MHz	16.65 MPa	10.94 MPa
f-01.pvd	0.9377 MHz	1.065 MHz	1.6421 MHz	17.48 MPa	11.63 MPa
f.pvd	0.9377 MHz	1.065 MHz	1.6479 MHz	17.66 MPa	11.78 MPa
f	0.9377 MHz	1.065 MHz	1.6595 MHz	18.03 MPa	12.06 MPa
g-01.pvd	0.9377 MHz	1.060 MHz	1.6341 MHz	17.22 MPa	11.61 MPa
g-01.pvd	0.9377 MHz	1.060 MHz	1.6636 MHz	18.16 MPa	12.34 MPa
h-01.pvd	0.9377 MHz	1.060 MHz	1.6530 MHz	17.82 MPa	12.08 MPa
br7-ch32	0.9377 MHz	1.064 MHz	1.6503 MHz	17.73 MPa	11.86 MPa
			Expected value	(16.97 ± 0.98) MPa	(11.27 ± 0.82) MPa

Table 6.7: Resonance frequencies and extrapolated residual stress (σ)

6.1.4 Allan deviation

The Allan deviation, as explained in section 5.3, is a useful indicator for resonator since it measure its frequency stability. Furthermore it can be used to estimate the minimum detectable mass by the resonator, assuming that the minimum detectable frequency change is that which gives a fractional change in frequency equal to the Allan variance: [68]:

$$\frac{\partial m}{m} = 2\frac{\partial f}{f} = 2\sigma_a \rightarrow \partial m = 2\sigma_a * m \tag{6.3}$$

The Allan deviation, measured in an open-loop condition, has been investigated with the help of the UHFLI lock-in amplifier from Zurich instruments. The characterization has been made only in air because of the drift of the resonance frequency in vacuum, explained in the above paragraph 6.1.2, was too high.

Chip 32 - Bridge 12

Below one example of the characterizations made on Chip 32 - Bridge 12 (Dimension Length x Width x Thickness = 50 µm x 7 µm x 450 nm) can be seen on picture 6.13. The plot can be divided in a descending and an ascending part (as better explained in the experimental chapter 5.3), that exhibit exponential behaviors of power ± 0.5. The dashed lines represent the fit of those two parts, with -0.509 and +0.489 as fitted exponent, giving an idea of the accuracy of the characterization. The minimum is at τ = 543.66 ms with a value on the y-axis of $\sigma(t)$=9.11 × 10^{-7}. According to equation 6.3 a minimum detectable mass of 595 ag can be estimated. Characterizations on bridge 12 are reported in table 6.8 and in Figure 6.14.

$\sigma(t)_{min}$	τ	Minimum detectable mass
9.75×10^{-7}	512.80 ms	638 ag
9.11×10^{-7}	543.66 ms	596 ag
9.25×10^{-7}	344.93 ms	605 ag
1.31×10^{-6}	446.93 ms	855 ag
1.01×10^{-6}	772.13 ms	660 ag
8.43×10^{-7}	811.59 ms	551 ag

Table 6.8: Allan deviation measurements made on Bridge 12 - Chip 32

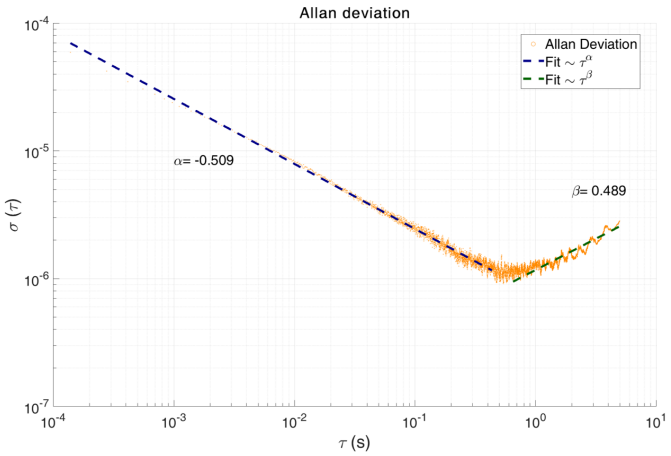

Figure 6.13: Allan deviation on bridge 13 - chip 32. The minimum is at $\tau = 543.66$ ms with a value on the y-axis of $\sigma(t)$=9.11 $\times$ 10^{-7}

.

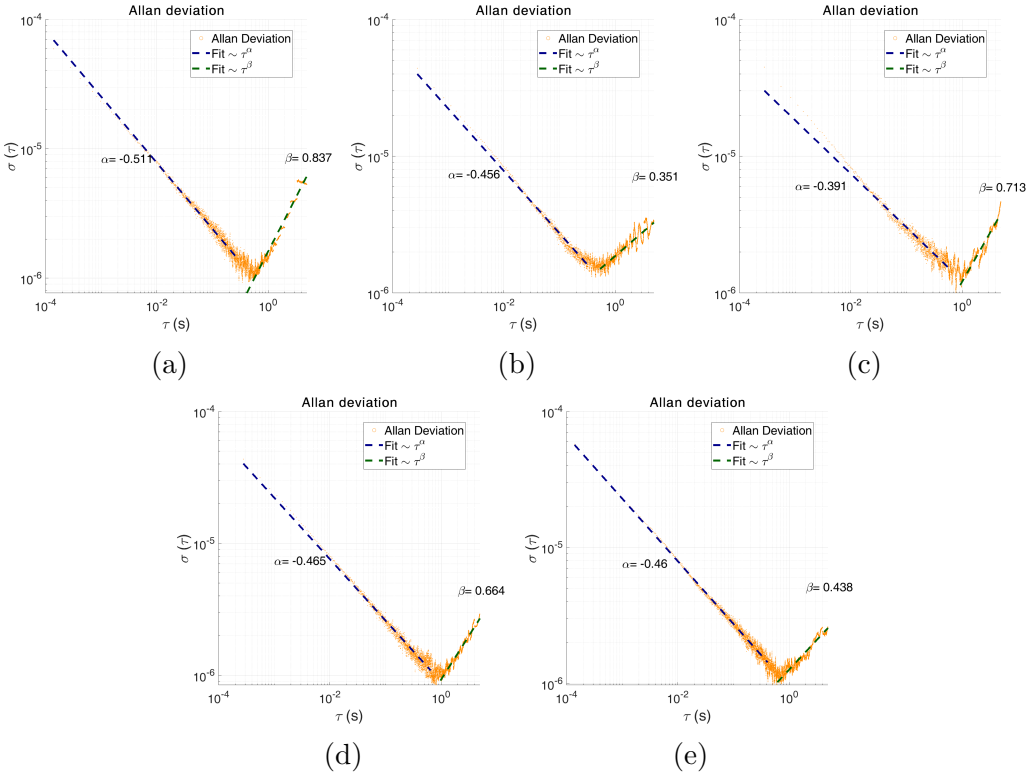

Figure 6.14: Plot of the Allan deviation characterizations reported in table 6.8

Chip 52 Bridge 6

Here is reported another example of Allan Deviation done on a different chip: Chip 52 Bridge 6 (Dimension Length x Width x Thickness = 50 µm x 6 µm x 450 nm) 6.15. The minimum is at τ = 505.16 ms with a value on the y-axis of $\sigma(t)$=1.68 × 10^{-6}. According to equation 6.3 a minimum detectable mass of 843 ag can be estimated. Characterizations on bridge 6 are reported in table 6.9 and in Figure 6.16.

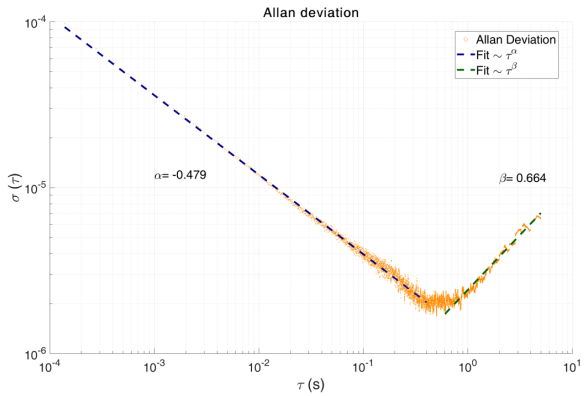

Figure 6.15: Allan deviation on bridge 6 - chip 52. The minimum is at τ = 505.16 ms with a value on the y-axis of $\sigma(t)$=1.68 × 10^{-6}

.

$\sigma(t)_{min}$	τ	Minimum detectable mass
1.68 × 10^{-6}	505.16 ms	843 ag
1.75 × 10^{-6}	529.34 ms	878 ag
2.49 × 10^{-6}	845.50 ms	1248 ag
2.13 × 10^{-6}	573.95 ms	1069 ag

Table 6.9: Allan deviation measurements made on Bridge 6 - Chip 52

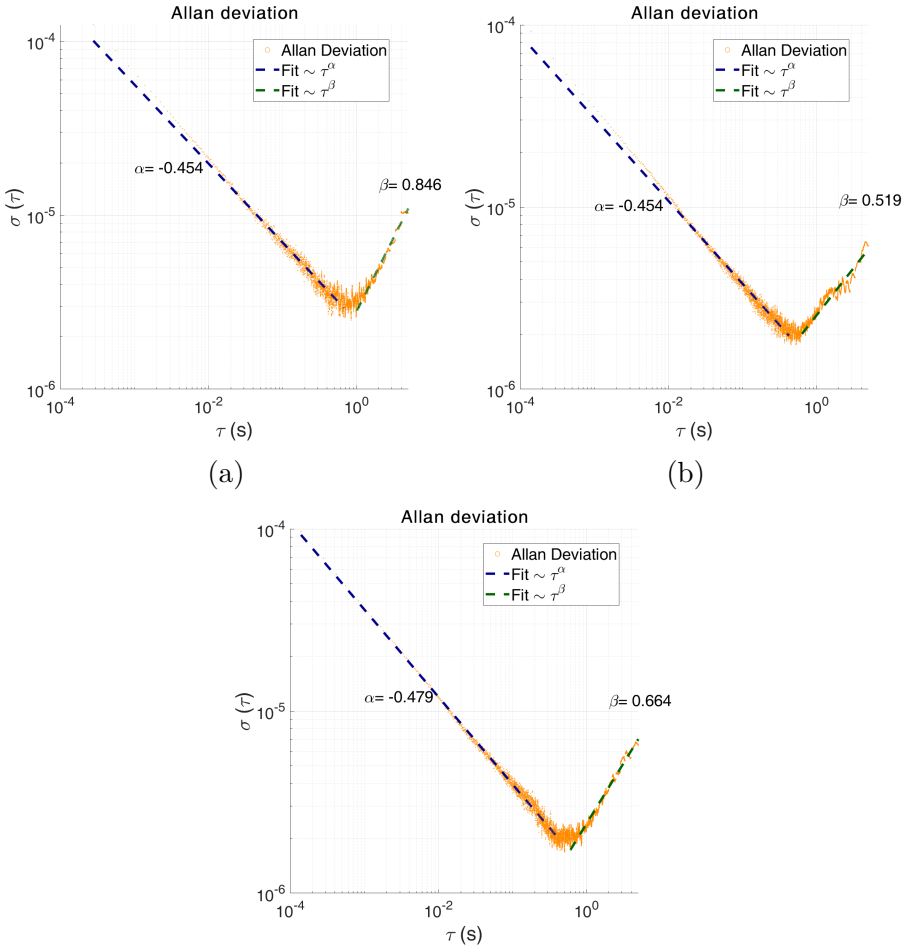

Figure 6.16: Plot of the Allan deviation characterizations reported in table 6.9

6.1.5 Nanochannel devices

The characterization on Nanochannel devices was carried out in a less thorough manner than the analysis performed on the nanoslit devices because the process has taken more time to be optimized, and hence to have working devices. The very small dimensions of the bridges (described in section Design 3.2) made it difficult the characterizations of the resonator, as the signal read from the MSA-500 was very noisy and the alignment of the laser spot was trickier. Especially for the 20 µm-long bridge was impossible to have a good signal and so to obtain a resonance spectrum. The 40 µm clamped-clamped beams have been "sacrificed" to put the test pads, described in 4.2.2. Below are reported two samples of the obtained results for these devices.

Chip 16

The characterizations have been performed in vacuum condition.
An example of obtained spectrum can be seen in Figure 6.17, Bridge 6 - chip 16 (Dimension (Length x Width x Thickness) = 30 µm x 5 µm x 450 nm). A Lorentzian

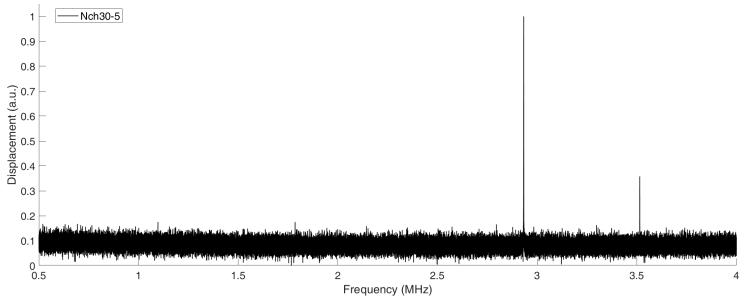

Figure 6.17: Spectra of nanochannel device - Bridge 6 - Chip 16

.

fit on the resonance peak, reported in Figure 6.17, allows to evaluate the resonance frequency and the quality factor:

- F_0 =2.932 59 MHz;
- Q =7006

Also in this case the experimental resonance frequency is higher with respect to the estimated one.

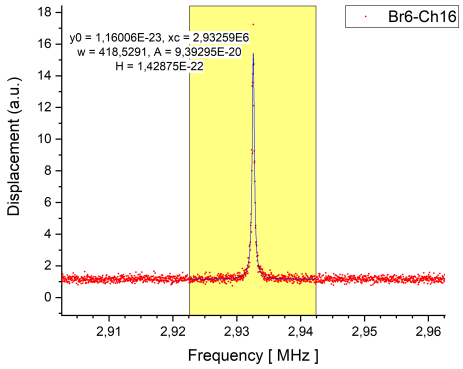

Figure 6.18: Lorentzian fit of the resonance peaks of the bridge 6 - chip 16. The blue line represents the fit while the yellow area the data interval of fitting.

Chip 45

In table 6.10 are reported the results obtained by the characterization of the 30 µm bridges on the chip 45. This chip have the peculiarity of be in a not (well) bonded region of the wafer. As can be seen, here that the tensile stress induced by the anodic bonding is not present, the resonance frequency is very close to the expected one $f_r^{theo} = 2.605\,\text{MHz}$, reported in the design section 3. These results consolidates the hypothesis made in 6.1.3.

Device	f_r^{exp}	QF
Br2	2.471 22 MHz	1673
Br5	2.542 89 MHz	2878
Br5	2.544 07 MHz	2852
Br8	2.544 77 MHz	2768
Br8	2.545 58 MHz	2929
Br11	2.471 22 MHz	1673
Br11	2.487 70 MHz	2352
Br11	2.488 78 MHz	2853
Br14	2.490 73 MHz	2542
Br14	2.497 14 MHz	3015

Table 6.10: Resonance frequencies of 30 µm clamped-clamped beams from chip 45.

6.2 Fluidics check

A fluidic check has been made on the devices in order to investigate if also the "fluidic path" of the devices, beyond the mechanical one, was working in the right way. The aim of this characterization is to evaluate if, on the fabricated chips, the nanometric channels is totally released and the interfaces between them and the microfluidic channels of bypass are well-opened. The best way to do that would have been by visual inspection, sadly it was not possible because the height of the channel (50 nm) was limiting too much every kind of signal that could be used to directly see the filling of the devices with some liquid. To overcome this problem I decided to proceed with an electric approach, sketched in picture 6.19a. All the channels have been filled with a conductive liquid solution (KCl - Potassium chloride - 1 M) using two opposite inlets as input ones. The microfluidic channels of bypass are linked only through the nanochannels; thus the idea is that a current can be seen only if the conductive path is continuous and so the liquid is filling also the nanochannel inside the bridges.

Below is reported one of the tests done as exemplification 6.19b. The red line represents the current present when the conductive solution is present (and the orange dashed line is its fit). The green line is the signal coming by the electric readout from the chip without the conductive solution. This measure has been made to ensure that the chip was not conductive by itself, but the conduction occurs only thanks the ions of the conductive solution.

Several trials have been made on different chips and all the tested chips were reporting a current when the conductive solution was injected, giving the idea that also the fluidic part of the chips was working.

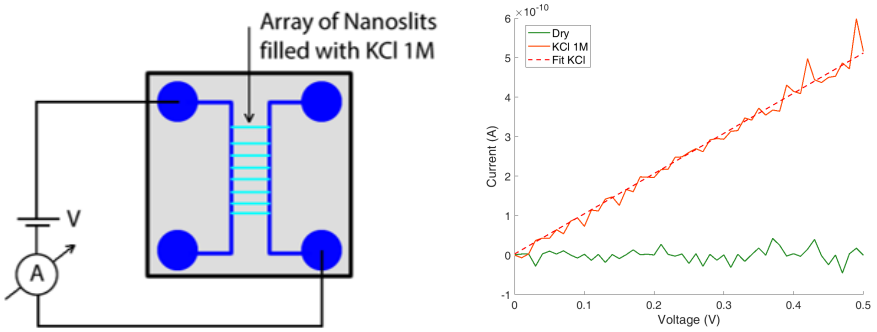

(a) (b)

Figure 6.19: (a) Sketch of the electric set-up for the fluidics check.
(b) IV plot of a fluidic check on a Chip (13).

6.3 Fluidics and mechanical characterization

In this part is described the characterization did joining the mechanical and the fluidic parts of the devices. The aim of this investigation is to see the behavior of the devices when liquids of different densities are injected in the system and, later, estimate a mass and density responsivities. The resonance frequency is firstly detected with the empty channel, and then the mechanical response is characterized with the channel filled with water ($999\,\mathrm{kg/m^3}$) and Ethanol ($789\,\mathrm{kg/m^3}$). These liquids were injected with the help of two syringes and pipes going through the chip holder (described in 5.2). The shifts of the resonance frequency calculated with respect to the empty case (and normalized by their maximum value) are expected to be dependent on the added mass according to the equation 6.4.

$$\Re_m = -\frac{1}{2}\frac{f_r}{m} \tag{6.4}$$

From the density vs frequency resonance plot the density and mass responsivity can be extrapolated A common issue found in every characterization of this type was the very slow filling of the channel; in some cases it took also some hours before seeing an appreciable shift on the resonance frequency. This is the main reason because, recalling the drift of resonance frequency under vacuum described above in 6.1.2, all the measurements on the devices used as density sensor have been done in air instead of vacuum.

Below some of the obtained results are reported.

Chip 32 - Bridge 12

The normalized resonance peaks for the bridge 12 (Dimension - Length x Width x Thickness = 50 µm x 7 µm x 450 nm) with 3 µm wide channel are shown in Figure 6.20. The scattered points, in transparency, are the measured data, while the line draw their Lorentzian fit. As can be seen denser is the liquid, bigger is the shift with respect to the empty case.

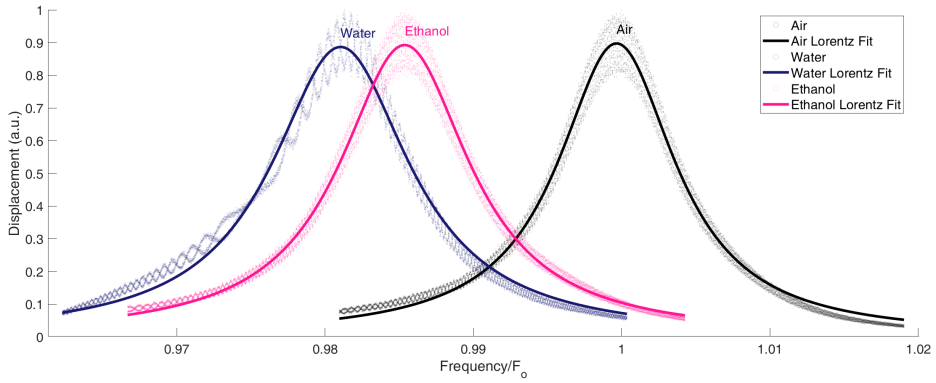

Figure 6.20: Resonance curves of the bridge 12 filled with different fluids: the shift increases with the fluid density.

The resonance frequency in empty condition is of 1.673 MHz ± 0.002 MHz with a quality factor of 114 ± 5 (90 ÷ 114 with liquids).

These shifts are plotted in function of the mass in Figure 6.21. The dashed line represents the fit of the experimental data according to equation 6.4: from its slope, it is possible to extrapolate the mass responsivity of the resonator as $\Re_m$=(3.85 ± 0.05) mHz/ag for the bridge under analysis. The density responsivity is $\Re_{density}$=(28.84 ± 0.37) Hz/[kg/m^3].

Resonance Frequency	(1.673 ± 0.002) MHz (empty)
Quality factor	114 ± 5 empty (90 ÷ 114 liquids)
Theoretical Responsivity	$\Re_m$=4.97 mHz/ag
Mass Responsivity	$\Re_m$ =(3.85 ± 0.05) mHz/ag
Minimum detectable Mass (Allan)	595 ag (551 ag ÷ 854 ag)
Density Responsivity	$\Re_{density}$ =(28.84 ± 0.37) Hz/[kg/m^3]

Table 6.11: Figures of merit for bridge 12-32.

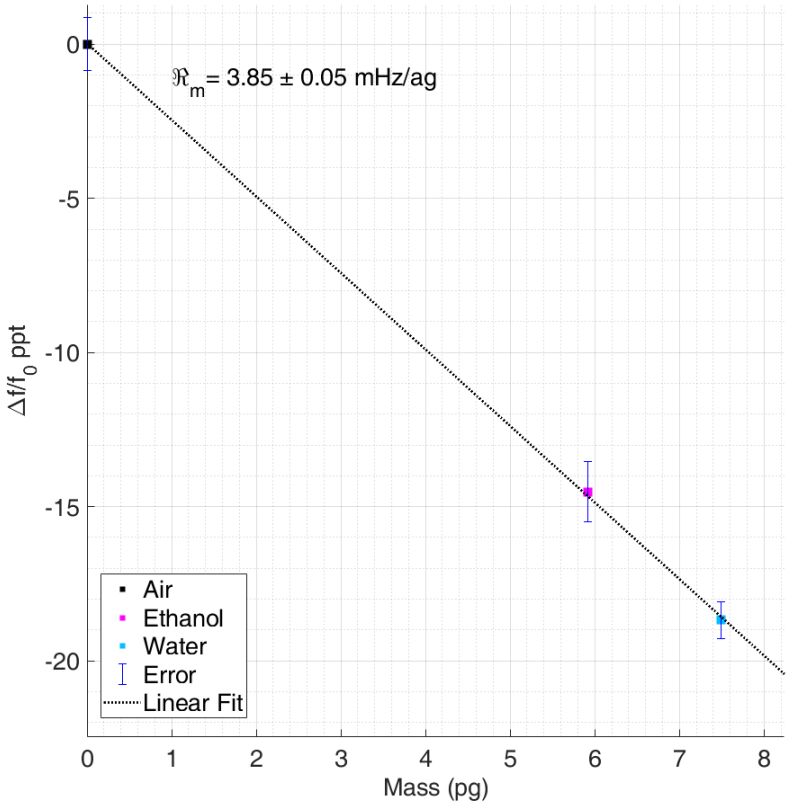

Figure 6.21: Plot of the frequency shifts as function of the mass of the medium inside the channel for the evaluation of the mass responsivity (slope of the linear fit, black dashed line) - Chip 12 Bridge 32.

Chip 32 - Bridge 8

The normalized resonance peaks for the bridge 8 (Dimension - Length x Width x Thickness = 50 µm x 7 µm x 450 nm) with 3 µm wide channel are shown in Figure 6.22

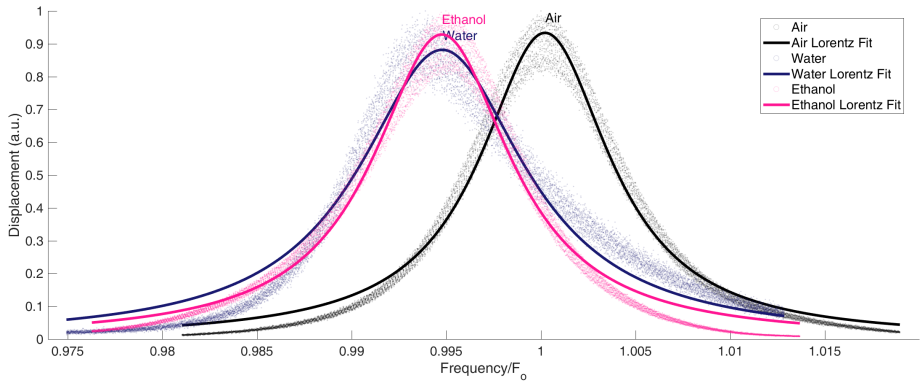

Figure 6.22: Resonance curves of the bridge 8 filled with different fluids: the shift increases with the fluid density.

The resonance frequency in empty condition is of (1.546 ± 0.003) MHz with a quality factor of 113 ± 15 ($50 \div 113$ with liquids).

These shifts are plotted in function of the mass in Figure 6.23. The mass responsivity of the resonator is $\Re_m$=(1.28 ± 0.04) mHz/ag for the bridge under analysis. The density responsivity is $\Re_{density}$=(9.32 ± 0.32) Hz/[kg/m^3].

In table 6.12 are resumed the figures of merit for the bridge under investigation (Chip 32 - Bridge 12).

Resonance Frequency	(1.546 ± 0.003) MHz (empty)
Quality factor	113 ± 15 ($50 \div 113$ with liquids)
Theoretical Responsivity	$\Re_m$=4.70 mHz/ag
Mass Responsivity	$\Re_m$=(1.28 ± 0.04) mHz/ag
Density Responsivity	$\Re_{density}$=(9.32 ± 0.32) Hz/[kg/m^3]

Table 6.12: Figures of merit for bridge 8-32.

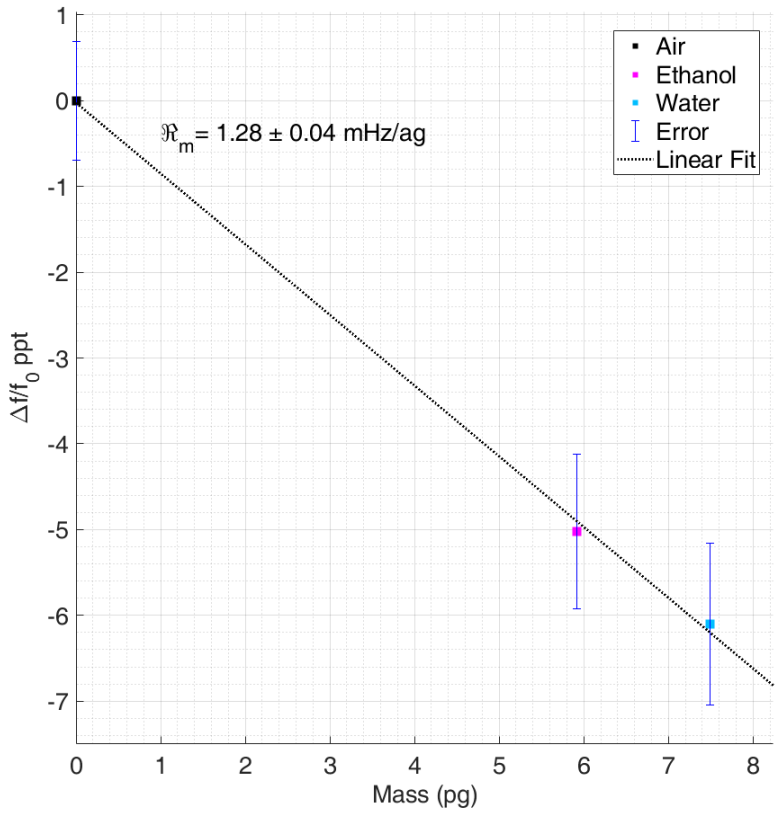

Figure 6.23: Plot of the frequency shifts as function of the mass for Bridge 8 - Chip 32.

Chip 56 - Bridge 13

The normalized resonance peaks for the bridge 13 (Dimension - Length x Width x Thickness = 50 µm x 8 µm x 450 nm) with 4 µm wide channel are shown in Figure 6.24.

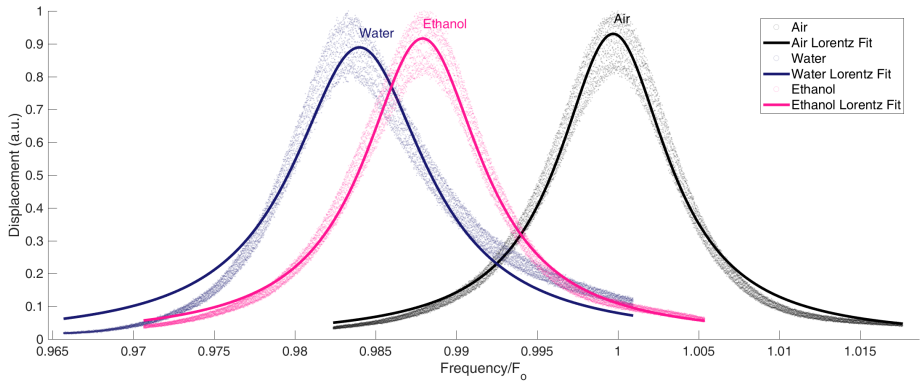

Figure 6.24: Resonance curves of the bridge 13 filled with different fluids: the shift increases with the fluid density.

The resonance frequency in empty condition is of (1.538 ± 0.008) MHz with a quality factor of 103 ± 8 ($80 \div 110$ with liquids).

These shifts are plotted in function of the mass in Figure 6.25. The mass responsivity of the resonator is $\Re_m$=(2.73 ± 0.21) mHz/ag for the bridge under analysis. The density responsivity is $\Re_{density}$=(27.27 ± 2.06) Hz/[kg/m^3].

In table 6.13 are resumed the figures of merit for the bridge under investigation (Chip 56 - Bridge 13).

Resonance Frequency	(1.538 ± 0.008) MHz (empty)
Quality factor	103 ± 8 ($80 \div 110$ with liquids)
Theoretical Responsivity	$\Re_m$=4.15 mHz/ag
Mass Responsivity	$\Re_m$=(2.73 ± 0.21) mHz/ag
Density Responsivity	$\Re_{density}$=(27.27 ± 2.06) Hz/[kg/m^3]

Table 6.13: Figures of merit for bridge 13-56.

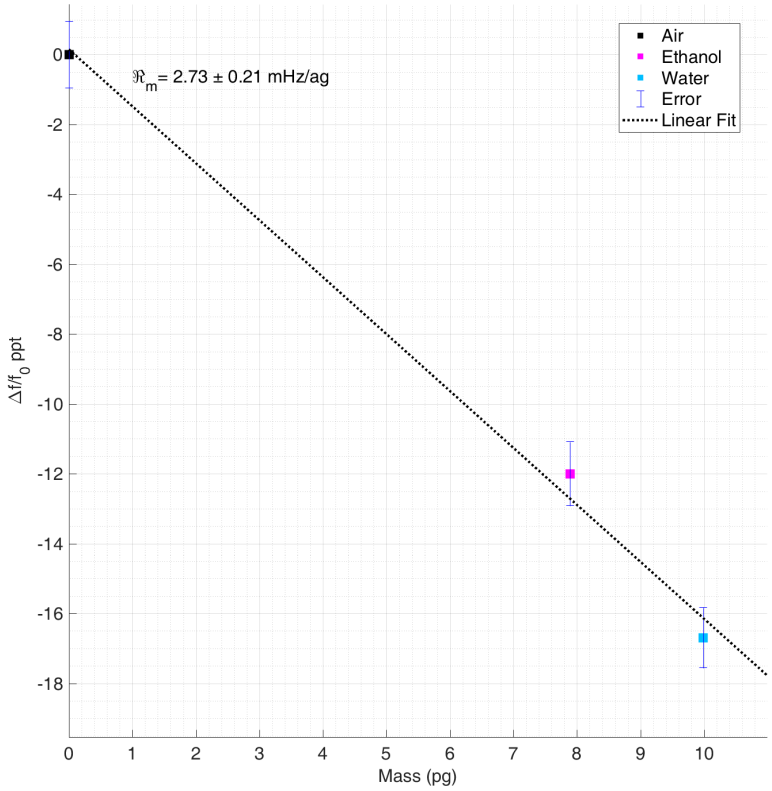

Figure 6.25: Plot of the frequency shifts as function of the mass for Bridge 13 - Chip 56.

Chip 56 - Bridge 18

The normalized resonance peaks for the bridge 18 (Dimension - Length x Width x Thickness = 50 µm x 8 µm x 450 nm) with 4 µm wide channel are shown in Figure 6.26.

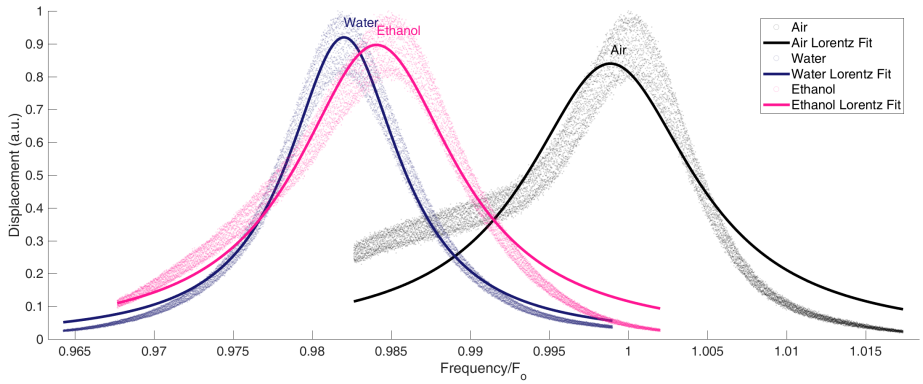

Figure 6.26: Resonance curves of the bridge 18 filled with different fluids: the shift increases with the fluid density.

The resonance frequency in empty condition is of (1.684 ± 0.006) MHz with a quality factor of 71 ± 18 ($70 \div 100$ with liquids).

These shifts are plotted in function of the mass in Figure 6.27. The mass responsivity of the resonator is $\Re_m$=(3.16 ± 0.11) mHz/ag for the bridge under analysis. The density responsivity is $\Re_{density}$=(31.59 ± 1.14) Hz/[kg/m^3].

In table 6.14 are resumed the figures of merit for the bridge under investigation (Chip 56 - Bridge 18).

Resonance Frequency	(1.684 ± 0.006) MHz (empty)
Quality factor	71 ± 18 ($70 \div 100$ with liquids)
Theoretical Responsivity	$\Re_m$=4.46 mHz/ag
Mass Responsivity	$\Re_m$=(3.16 ± 0.11) mHz/ag
Density Responsivity	$\Re_{density}$=(31.59 ± 1.14) Hz/[kg/m^3]

Table 6.14: Figures of merit for bridge 18-56.

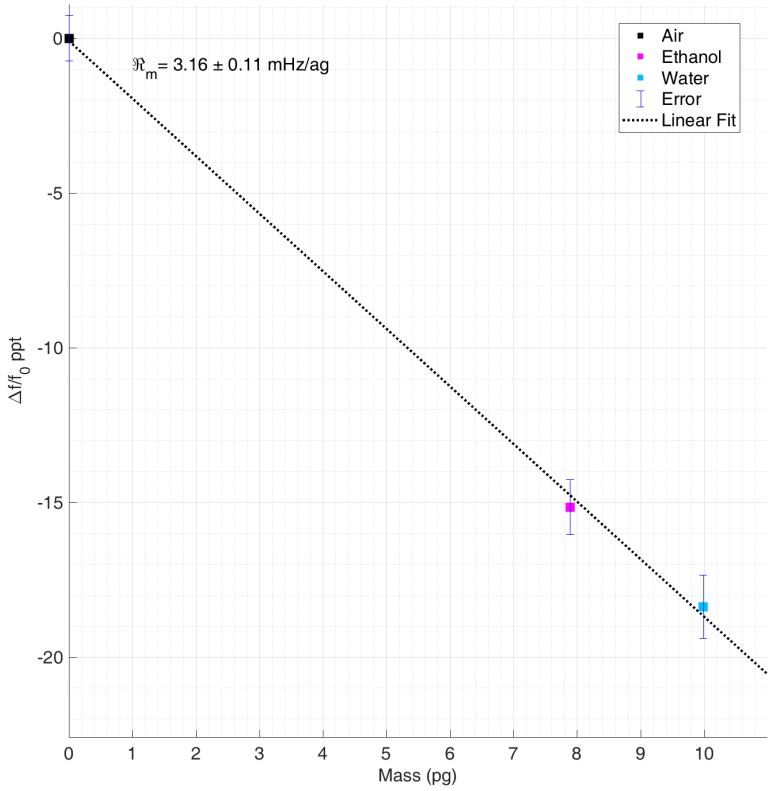

Figure 6.27: Plot of the frequency shifts as function of the mass for Bridge 18 - Chip 56.

6.3.1 Figures of merit

In table 6.15 are resumed the figures of merit for the previous presented bridges. Looking at them and comparing the mass responsivities obtained by theoretical calculations $\Re_m^{theo}$ and the experimental ones $\Re_m^{exp}$ is possible to see that the last one, in each case, is considerably lower with respect to the expected one. This result is not surprising because the theoretical calculations does not take in account all the non-idealities of the devices and the signal losses occurring during the characterizations that contribute to lower the values of the mass responsivity.

Device	f_r	QF	Re_{mass}^{theo}	$\Re_{mass}^{exp}$	$\Re_{density}$
Ch32-Br12	1.673 MHz	114	4.97 mHz/ag	3.85 mHz/ag	28.84 Hz/[kg/m^3]
Ch32-Br08	1.546 MHz	113	4.70 mHz/ag	1.28 mHz/ag	9.32 Hz/[kg/m^3]
Ch56-Br13	1.538 MHz	103	4.15 mHz/ag	2.73 mHz/ag	27.27 Hz/[kg/m^3]
Ch56-Br18	1.684 MHz	71	4.46 mHz/ag	3.16 mHz/ag	31.59 Hz/[kg/m^3]

Table 6.15: Figures of merit of the nanoslit devices.

Chapter 7

Conclusions

In this thesis a complete process for the realization of suspended nanochannel resonators is presented. A flexible fabrication process has been developed thanks to which it is possible to make different types of SNRs just by varying some steps during the fabrication: nanoslit (4.1), nanochannel (4.2) and the so called "2-step nanoslit device" (4.3). The yield of the process flow, for the nanoslit devices, can be assessed around 50%.

The mechanical characterizations performed on the devices gave very good and promising results: quality factor values of the order of thousands have been obtained in vacuum for nanoslit and nanochannel devices. Values of resonance frequency higher with respect to the theoretically calculated ones have been measured. This discrepancy has been attributed to the residual tensile stress induced by the anodic bonding performed to seal the chips, as analyzed and explained in chapter 6.1.3. Anyway, the rising of the resonance frequency is not a disadvantage because it cooperates in the increase of the performance of the devices as mass sensors.

In fact, fabricated nanoslit devices show an experimental mass responsivity up to (3.90 ± 0.72) mHz/ag and an estimated minimum detectable mass up to 595 ag, with measurement performed in air. These devices have been also tested with liquids having different densities showing a responsivity up to (28.84 ± 0.37) Hz/[kg/m^3].

The process flow for the fabrication of the "2-step nanoslit" devices has been developed and a proof of concept of the working principle has been given, even though the effective characterization of these devices suffered the low priority imposed by the measurements on the other devices.

For the nanochannel devices only characterization on the mechanical proprieties has been done, showing an expected mass responsivity up to 19.97 mHz/ag.

In conclusion it has been reported, for the first time, a top-down fabrication approach for a SNR [10, 34, 41] in which the critical dimension of the channel was as small as 50 nm. Moreover, a set-up for the characterization of devices combining micromechanics and nanofluidics has been assembled giving promising results toward their application for the detection of nanoparticles.

Bibliography

1. Salata, O. V. Applications of nanoparticles in biology and medicine. *J. Nanobiotechnology* **2,** 3. ISSN: 1477-3155 (Apr. 2004).
2. Lan, Y., Lu, Y. & Ren, Z. Mini review on photocatalysis of titanium dioxide nanoparticles and their solar applications. *Nano Energy* **2,** 1031–1045. ISSN: 2211-2855 (2013).
3. Zhang, W.-x. Nanoscale Iron Particles for Environmental Remediation: An Overview. *J. Nanoparticle Res.* **5,** 323–332. ISSN: 1572-896X (2003).
4. Lu, P.-J., Huang, S.-C., Chen, Y.-P., Chiueh, L.-C. & Shih, D. Y.-C. Analysis of titanium dioxide and zinc oxide nanoparticles in cosmetics. *J. Food Drug Anal.* **23,** 587–594. ISSN: 1021-9498 (2015).
5. Dickinson, E. Use of nanoparticles and microparticles in the formation and stabilization of food emulsions. *Trends Food Sci. Technol.* **24,** 4–12. ISSN: 0924-2244 (2012).
6. Suh, W. H., Suslick, K. S., Stucky, G. D. & Suh, Y.-H. Nanotechnology, nanotoxicology, and neuroscience. *Prog. Neurobiol.* **87,** 133–170. ISSN: 0301-0082 (2009).
7. Michen, B. *et al.* Avoiding drying-artifacts in transmission electron microscopy: Characterizing the size and colloidal state of nanoparticles. *Sci. Rep.* **5,** 9793 (May 2015).
8. Hoo, C. M., Starostin, N., West, P. & Mecartney, M. L. A comparison of atomic force microscopy (AFM) and dynamic light scattering (DLS) methods to characterize nanoparticle size distributions. *J. Nanoparticle Res.* **10,** 89–96. ISSN: 1572-896X (2008).
9. Donovan, A. R. *et al.* Single particle ICP-MS characterization of titanium dioxide, silver, and gold nanoparticles during drinking water treatment. *Chemosphere* **144,** 148–153. ISSN: 0045-6535 (2016).
10. Lee, J., Shen, W., Payer, K., Burg, T. P. & Manalis, S. R. Toward attogram mass measurements in solution with suspended nanochannel resonators. *Nano Lett.* **10,** 2537–2542. ISSN: 1530-6984 (2010).

11. Schmid, S., Villanueva, L. G. & Roukes, M. L. *Fundamentals of nanomechanical resonators* 1–175. ISBN: 9783319286914. doi:10.1007/978-3-319-28691-4 (2016).

12. Burg, T. P. & Manalis, S. R. Suspended microchannel resonators for biomolecular detection. *Appl. Phys. Lett.* **83,** 2698–2700. ISSN: 0003-6951 (2003).

13. Arlett, J. L., Myers, E. B. & Roukes, M. L. Comparative advantages of mechanical biosensors. *Nat. Nanotechnol.* **6,** 203. ISSN: 17483395 (Mar. 2011).

14. Tamayo, J., Kosaka, P. M., Ruz, J. J., San Paulo, Á. & Calleja, M. Biosensors based on nanomechanical systems. *Chem. Soc. Rev.* **42,** 1287–1311. ISSN: 0306-0012 (2013).

15. Braun, T. *et al.* Quantitative time-resolved measurement of membrane protein–ligand interactions using microcantilever array sensors. *Nat. Nanotechnol.* **4,** 179 (Jan. 2009).

16. Maloney, N., Lukacs, G., Ball, S. L. & Hegner, M. Device for filamentous fungi growth monitoring using the multimodal frequency response of cantilevers. *Rev. Sci. Instrum.* **85,** 15003. ISSN: 0034-6748 (Jan. 2014).

17. Yue, M. *et al.* A 2-D microcantilever array for multiplexed biomolecular analysis. *J. Microelectromechanical Syst.* **13,** 290–299. ISSN: 1057-7157 VO - 13 (2004).

18. Gupta, A., Akin, D. & Bashir, R. Single virus particle mass detection using microresonators with nanoscale thickness. *Appl. Phys. Lett.* **84,** 1976–1978. ISSN: 0003-6951 (Mar. 2004).

19. Lin, Y.-C., Jen, C.-M., Huang, M.-Y., Wu, C.-Y. & Lin, X.-Z. Electroporation microchips for continuous gene transfection. *Sensors Actuators B Chem.* **79,** 137–143. ISSN: 0925-4005 (2001).

20. Ilic, B., Yang, Y. & Craighead, H. G. Virus detection using nanoelectromechanical devices. *Appl. Phys. Lett.* **85,** 2604–2606. ISSN: 0003-6951 (Sept. 2004).

21. SUN, Y. U. & NELSON, B. J. MEMS FOR CELLULAR FORCE MEASUREMENTS AND MOLECULAR DETECTION. *Int. J. Inf. Acquis.* **01,** 23–32. ISSN: 0219-8789 (Mar. 2004).

22. Ricciardi, C. *et al.* Microcantilever resonator arrays for immunodetection of β-lactoglobulin milk allergen. *Sensors Actuators B Chem.* **254,** 613–617. ISSN: 0925-4005 (2018).

23. Su, M., Li, S. & Dravid, V. P. Microcantilever resonance-based DNA detection with nanoparticle probes. *Appl. Phys. Lett.* **82,** 3562–3564. ISSN: 0003-6951 (May 2003).

24. Naik, A. K., Hanay, M. S., Hiebert, W. K., Feng, X. L. & Roukes, M. L. Towards single-molecule nanomechanical mass spectrometry. *Nat. Nanotechnol.* **4,** 445. ISSN: 17483395 (June 2009).

25. Wasisto, H. S. *et al. A resonant cantilever sensor for monitoring airborne nanoparticles* in *2011 16th Int. Solid-State Sensors, Actuators Microsystems Conf.* (2011), 1116–1119. ISBN: 2164-1641 VO -. doi:10.1109/TRANSDUCERS.2011.5969233.

26. Chaste, J. *et al.* A nanomechanical mass sensor with yoctogram resolution. *Nat. Nanotechnol.* **7,** 301. ISSN: 17483395 (Apr. 2012).

27. *Affinity Biosensor - LifeScale* http://www.affinitybio.com/technology/resonant%7B%5C_%7Dmass%7B%5C_%7Dmeasurement.php.

28. Ekinci, K. L., Yang, Y. T. & Roukes, M. L. Ultimate limits to inertial mass sensing based upon nanoelectromechanical systems. *J. Appl. Phys.* **95,** 2682–2689. ISSN: 00218979 (2004).

29. Burg, T. P. *et al.* Weighing of biomolecules, single cells and single nanoparticles in fluid. *Nature* **446,** 1066. ISSN: 14764687 (Apr. 2007).

30. Burg, T. P. *et al.* Vacuum-Packaged Suspended Microchannel Resonant Mass Sensor for Biomolecular Detection. *J. Microelectromechanical Syst.* **15,** 1466–1476. ISSN: 1057-7157 VO - 15 (2006).

31. Dextras, P. *et al.* Fabrication and characterization of an integrated microsystem for protein preconcentration and sensing. *J. Microelectromechanical Syst.* **20,** 221–230. ISSN: 10577157 (2011).

32. Corman, T., Enoksson, P., Norén, K. & Stemme, G. A low-pressure encapsulated resonant fluid density sensor with feedback control electronics. *Meas. Sci. Technol.* **11,** 205–211. ISSN: 09570233 (2000).

33. Enoksson, P., Stemme, G. & Stemme, E. Fluid density sensor based on resonance vibration. *Sensors Actuators A Phys.* **47,** 327–331. ISSN: 0924-4247 (1995).

34. Barton, R. A. *et al.* Fabrication of a Nanomechanical Mass Sensor Containing a Nanofluidic Channel. *Nano Lett.* **10,** 2058–2063. ISSN: 1530-6984 (June 2010).

35. Olcum, S. *et al.* Weighing nanoparticles in solution at the attogram scale. *Proc. Natl. Acad. Sci.* **111,** 1310–1315. ISSN: 0027-8424 (2014).

36. Khan, M. F., Schmid, S., Davis, Z. J., Dohn, S. & Boisen, A. Fabrication of resonant micro cantilevers with integrated transparent fluidic channel. *Microelectron. Eng.* **88,** 2300–2303. ISSN: 0167-9317 (Aug. 2011).

37. Vidal-Álvarez, G., Marigó, E., Torres, F. & Barniol, N. Fabrication and measurement of a suspended nanochannel microbridge resonator monolithically integrated with CMOS readout circuitry. *Micromachines* **7,** 40. ISSN: 2072666X (Mar. 2016).

38. Marquez, S. *et al.* Array of Microfluidic Beam Resonators for Density and Viscosity Analysis of Liquids. *J. Microelectromechanical Syst.* **26,** 749–757. ISSN: 1057-7157 VO - 26 (2017).

39. De Pastina, A., Maillard, D. & Villanueva, L. G. Fabrication of suspended microchannel resonators with integrated piezoelectric transduction. *Microelectron. Eng.* **192,** 83–87. ISSN: 01679317 (2018).

40. Lee, J. *et al.* Suspended microchannel resonators with piezoresistive sensors. *Lab Chip* **11,** 645–651. ISSN: 1473-0197 (2011).

41. Kim, J. *et al.* Hollow Microtube Resonators via Silicon Self-Assembly toward Subattogram Mass Sensing Applications. *Nano Lett.* **16,** 1537–1545. ISSN: 1530-6984 (Mar. 2016).

42. Sudoh, K., Iwasaki, H., Hiruta, R., Kuribayashi, H. & Shimizu, R. Void shape evolution and formation of silicon-on-nothing structures during hydrogen annealing of hole arrays on Si(001). *J. Appl. Phys.* **105,** 83536. ISSN: 0021-8979 (Apr. 2009).

43. Calmo, R. *et al.* Monolithic glass suspended microchannel resonators for enhanced mass sensing of liquids. *Sensors Actuators B Chem.* **283,** 298–303. ISSN: 0925-4005 (2019).

44. Sugioka, K. *et al.* Femtosecond laser 3D micromachining: a powerful tool for the fabrication of microfluidic, optofluidic, and electrofluidic devices based on glass. *Lab Chip* **14,** 3447–3458. ISSN: 1473-0197 (2014).

45. Bauchau, O. A. & Craig, J. I. in *Euler-Bernoulli beam theory* 173–221 (Springer, Dordrecht, 2009). doi:10.1007/978-90-481-2516-6_5.

46. Boisen, A., Dohn, S., Keller, S. S., Schmid, S. & Tenje, M. Cantilever-like micromechanical sensors. *Reports Prog. Phys.* **74.** ISSN: 00344885. doi:10.1088/0034-4885/74/3/036101 (2011).

47. Hennemeyer, M., Burghardt, S. & Stark, R. W. Cantilever Micro-rheometer for the Characterization of Sugar Solutions. *Sensors* **8,** 10–22. ISSN: 1424-8220 (2008).

48. Green, E. I. The Story of Q. *Am. Sci.* **43,** 584–594. ISSN: 00030996 (1955).

49. Yang, Y. T., Callegari, C., Feng, X. L., Ekinci, K. L. & Roukes, M. L. Zeptogram-Scale Nanomechanical Mass Sensing. *Nano Lett.* **6,** 583–586. ISSN: 1530-6984 (Apr. 2006).

50. Armbruster, D. A. & Pry, T. Limit of blank, limit of detection and limit of quantitation. *Clin. Biochem. Rev.* **29 Suppl 1,** S49–52. ISSN: 0159-8090 (Aug. 2008).

51. Nelissen, K., Misko, V. R. & Peeters, F. M. Single-file diffusion of interacting particles in a one-dimensional channel. *Europhys. Lett.* **80,** 56004 (Nov. 2007).

52. Carlotti, G. *et al.* Measurement of the elastic and viscoelastic properties of dielectric films used in microelectronics. *Thin Solid Films* **414,** 99–104. ISSN: 00406090 (2002).

53. Krishnan, M., Mojarad, N., Kukura, P. & Sandoghdar, V. Geometry-induced electrostatic trapping of nanometric objects in a fluid. *Nature* **467,** 692–695. ISSN: 14764687 (2010).

54. Larryisgood [CC BY-SA 3.0] from Wikimedia Commons. *Double Layer.png*

55. Chang, C., Abe, T. & Esashi, M. Trench filling characteristics of low stress TEOS/ozone oxide deposited by PECVD and SACVD. *Microsyst. Technol.* **10,** 97–102. ISSN: 09467076 (2004).

56. Tramšek, M. & Žemva, B. Synthesis, properties and chemistry of xenon (II) fluoride. *Acta Chim. Slov.* **53,** 105–116. ISSN: 13180207 (2006).

57. Brazzle, J., Doheci, M. & Mastrangelo, C. Modeling and characterization of sacrificial polysilicon etching using vapor-phase xenon difluoride. *17th Int. Conf. MEMS. IEEE,* 1–4. ISSN: 10846999 (2004).

58. Winters, H. F. & Coburn, J. W. The etching of silicon with XeF2 vapor. *Appl. Phys. Lett.* **34,** 70–73. ISSN: 00036951 (1979).

59. Chang, F. I. *et al.* Gas-phase silicon micromachining with xenon difluoride. *Int. Soc. Opt. Photonics* **2641,** 117. ISSN: 0277786X (Sept. 1995).

60. Cozma, A. & Puers, B. Characterization of the electrostatic bonding of silicon and Pyrex glass. *J. Micromechanics Microengineering* **5,** 98–102 (June 1995).

61. *BOROFLOAT ® 33 & Glass Wafers : A Union of Inspiration & Quality* https://www.schott.com/d/borofloat/b8e85c79-374f-460b-a0e2-1cd2f4a41974/1.0/borofloat%7B%5C_%7Dwafer%7B%5C_%7Ddb%7B%5C_%7Drow.pdf.

62. Wensink, H., Berenschot, J., Jansen, H. & Elwenspoek, M. High resolution powder blast micromachining. *Proc. IEEE Thirteen. Annu. Int. Conf. Micro Electro Mech. Syst. (Cat. No.00CH36308),* 769–774. ISSN: 1084-6999 (2000).

63. Tilli, M. *et al. Handbook of Silicon Based MEMS Materials and Technologies* ISBN: 9780815515777 (2015).

64. Plaza, J. A., Esteve, J. & Lora-Tamayo, E. Effect of silicon oxide, silicon nitride and polysilicon layers on the electrostatic pressure during anodic bonding. *Sensors And Actuators* **67,** 181–184. ISSN: 0924-4247 (May 1998).

65. Priest, J., Caswell, H. L. & Budo, Y. Mechanical stresses in silicon oxide films. *Vacuum* **12,** 301–306. ISSN: 0042207X (1962).

66. Allan, D. W., Gray, J. E. & Machlan, H. E. The National Bureau of Standards Atomic Time Scales: Generation, Dissemination, Stability, and Accuracy. *IEEE Trans. Instrum. Meas.* **21,** 388–391. ISSN: 0018-9456 (1972).

67. Walls, F. L. & Allan, D. W. Measurements of Frequency Stability. *Proc. IEEE* **74,** 162–168. ISSN: 15582256 (1986).

68. Cleland, A. N. Thermomechanical noise limits on parametric sensing with nanomechanical resonators. *New J. Phys.* **7.** ISSN: 13672630. doi:10.1088/1367-2630/7/1/235 (2005).

69. Crowell, J. E., Tedder, L. L., Cho, H.-C., Cascarano, F. M. & Logan, M. A. The chemical vapor deposition of SiO2 from teos. *J. Electron Spectros. Relat. Phenomena* **54-55,** 1097–1104. ISSN: 0368-2048 (1990).

70. Habermehl, S., Glenzinski, A. K., Halliburton, W. M. & Sniegowski, J. J. *Properties of Low Residual Stress Silicon Oxynitrides Used as a Sacrificial Layer* in *MRS Proc.* **605** (Cambridge University Press, Jan. 2000), 49–54. doi:10.1557/PROC-605-49. http://journals.cambridge.org/abstract%7B%5C_%7DS1946427400190773.

Appendix A

Picture Gallery

A.1 Nanoslit Devices - SEM

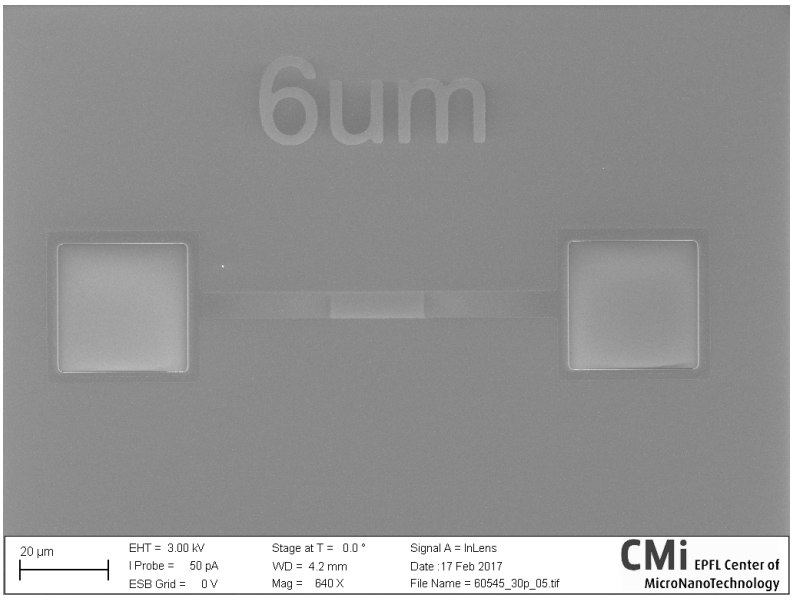

Figure A.1: Picture of a channel in which failed the releasing.

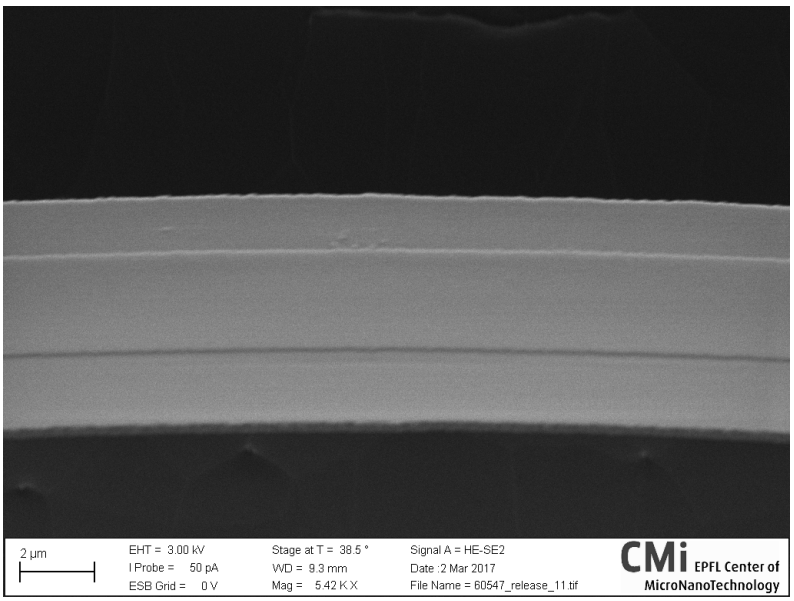

Figure A.2: Detail of a clamped-clamped beam, bended.

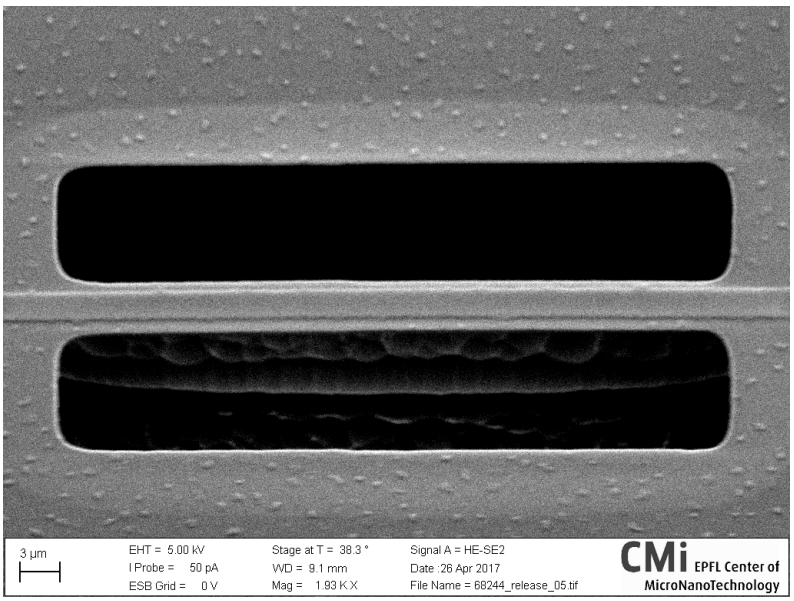

Figure A.3: Detail of a clamped-clamped beam. It worth to see here the absence of bending.

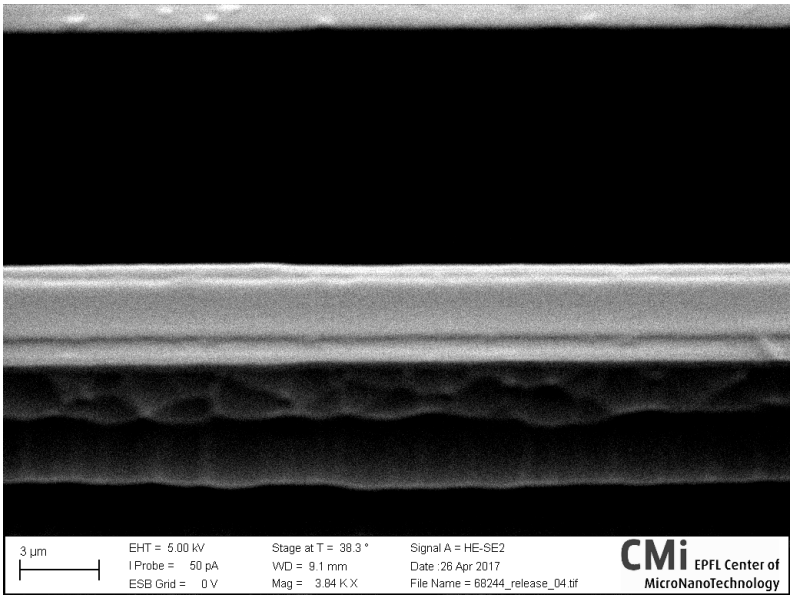

Figure A.4: Detail of a nanoslit device highlighting the few lateral space that can be used for the alignment tolerance.

A.2 Nanochannel Devices - SEM

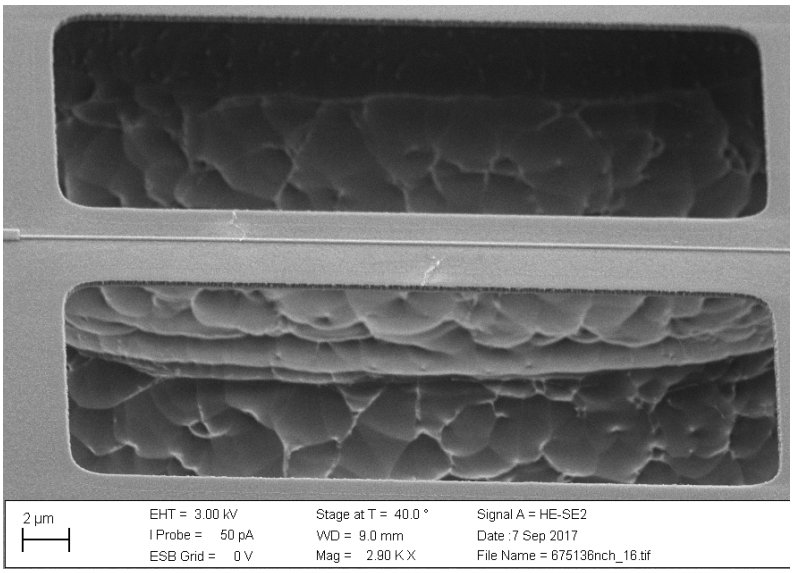

Figure A.5: Detail of a nanochannel device.

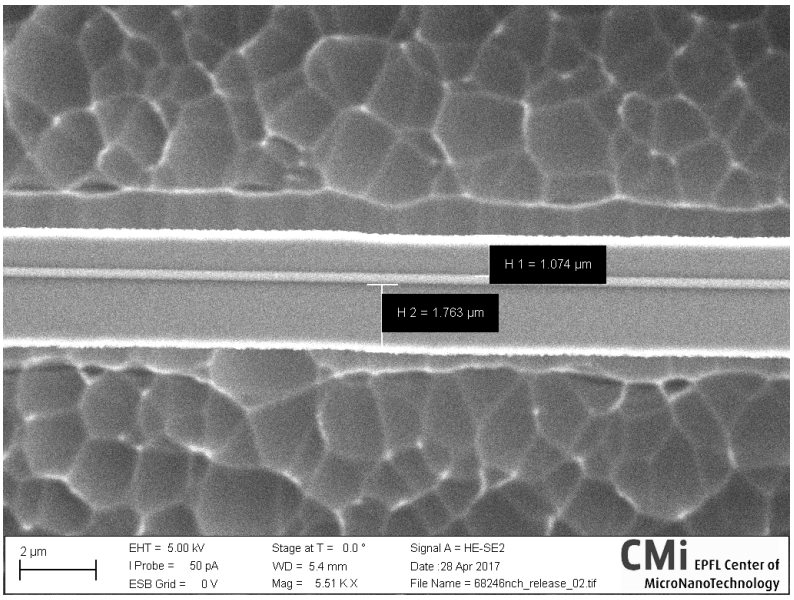

Figure A.6: Detail of a nanochannel device highlighting a mismatching in the alignment between the channel and the beam.

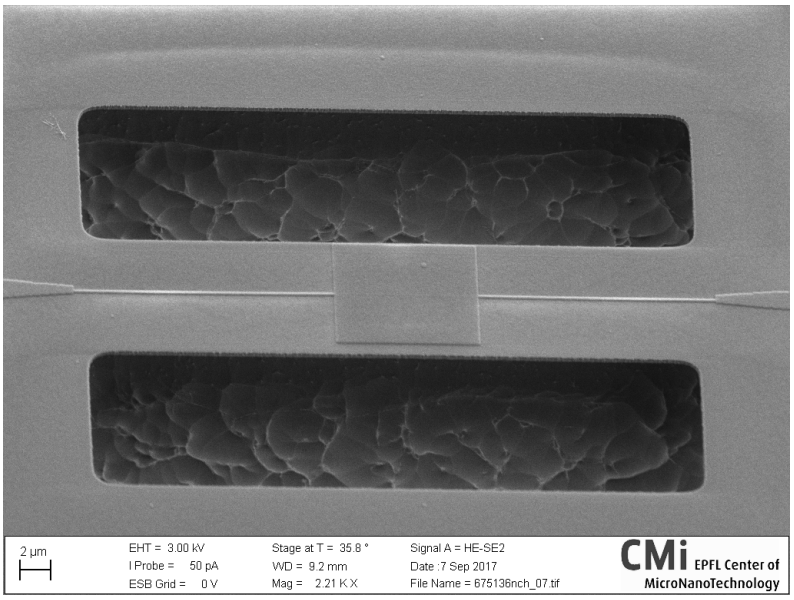

Figure A.7: Nanochannel device with the test pad.

A.3 Nanochannel Devices - Optical Microscope

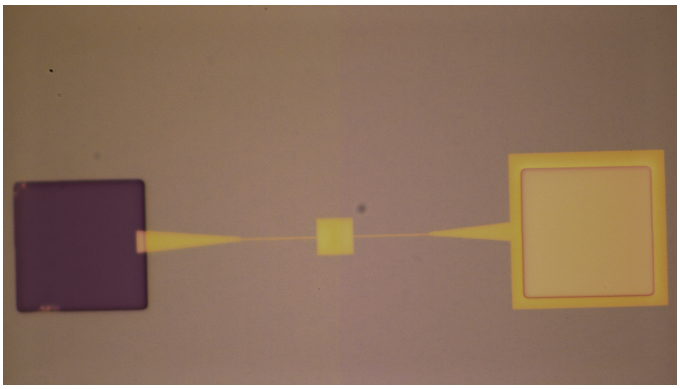

Figure A.8: Released nanochannel (width = 100 nm) device with the test pad.

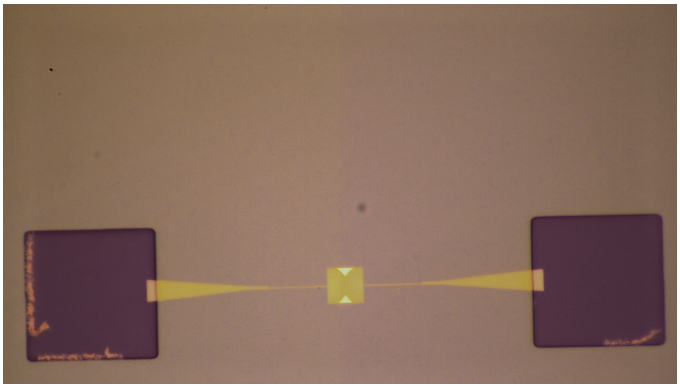

Figure A.9: Released nanochannel (width = 80 nm) device with the test pad.

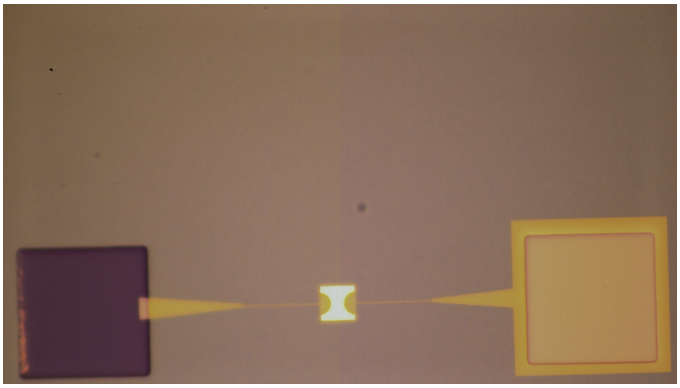

Figure A.10: Released nanochannel (width = 50 nm) device with the test pad.

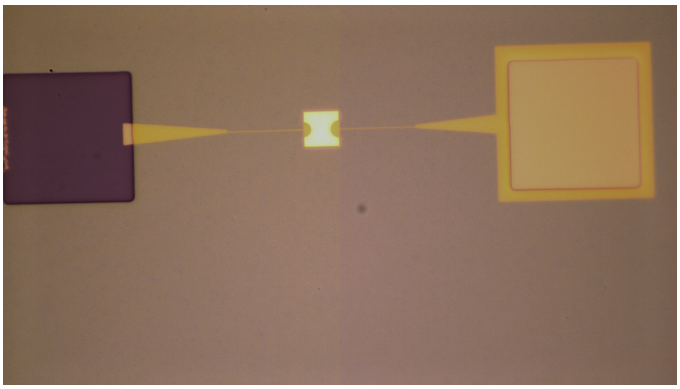

Figure A.11: Released nanochannel (width = 40 nm) device with the test pad.

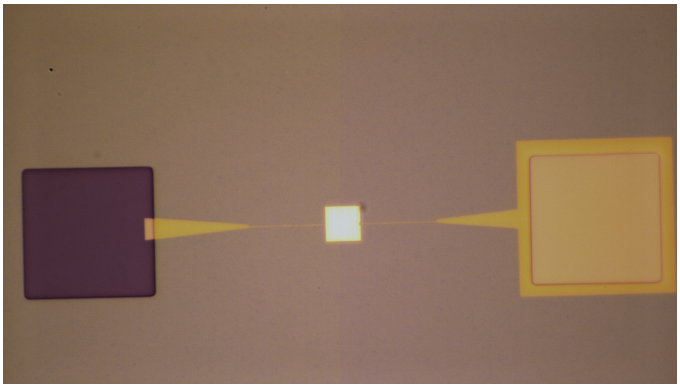

Figure A.12: Nanochannel (width = 30 nm) device with the test pad.

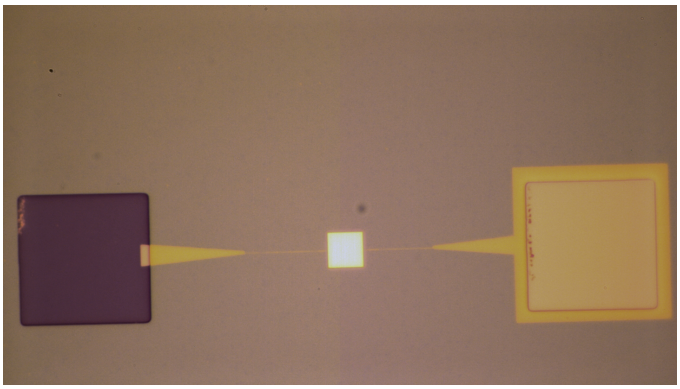

Figure A.13: Nanochannel (width = 20 nm) device with the test pad.

Appendix B

Process flow for glass sealing wafer

1. Hard Mask Deposition on Borofloat B.1a
   (a) Borofloat 33 as starting wafer
   (b) Cr/Au deposition with Sputtering DP650 – Recipe HTU_E_300_Cr-Au-Cr-Au for 2 x 20 nm Cr + 2 x 20 nm Au
2. Photolithography on hard mask B.1b
   (a) Coating with ACS200 - AZ 1512HS, 2 µm
   (b) Exposition with MLA150
   (c) Develop with ACS200 - AZ 1512HS, 2 µm
   (d) SRD Rinse, wet bench
3. Pattern Transfer on hard mask B.1c
   (a) IBE to etch 440 nm of hard mask layer
4. Microchannel structuration B.1d
   (a) HF wet etch – 15 µm deep on Pyrex
5. Inlet structuration by Powder Blasting @ IcoFlex Sàrl
6. PR and Cr/Au removal
   (a) PR Removal - Tepla oxygen plasma, High power 2 min
   (b) acid wet bench (Au wet etch + Cr wet etch)
7. Anodic Bonding B.1e
   (a) Standard recipe: A_T350_480

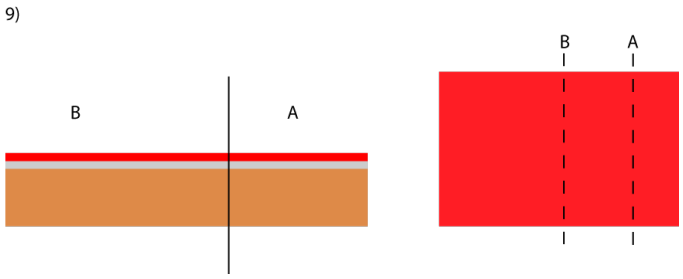

(a) Step 1

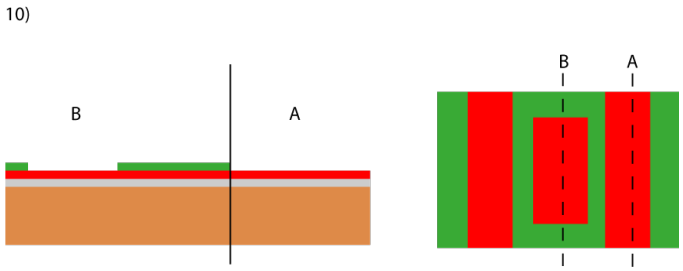

(b) Step 2

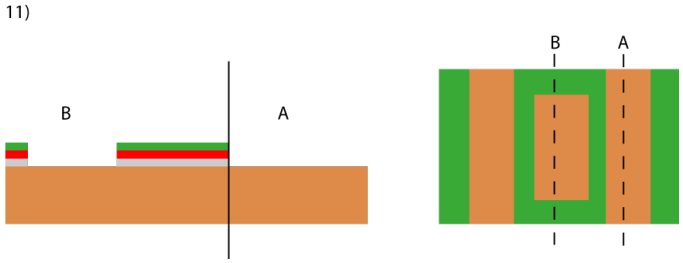

(c) Step 3

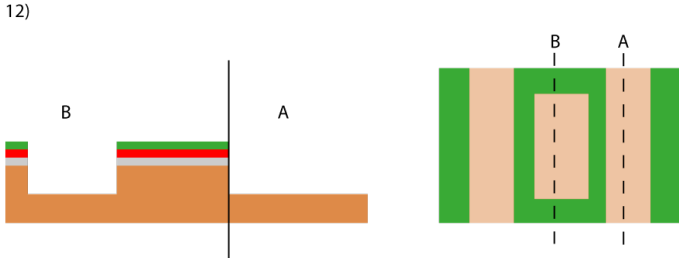

(d) Step 4

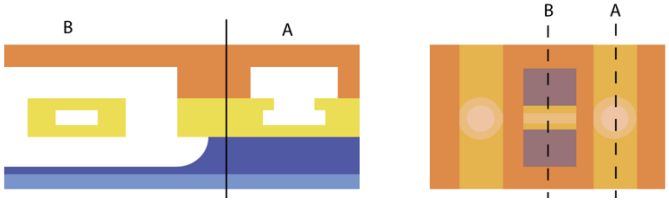

(e) Step 7

Figure B.1: Process flow for glass sealing wafer. Brown-glass, Red-Gold, Grey-Chromium, Green-Photoresist, Yellow-Silicon oxide device layer

This Ph.D. thesis has been typeset by means of the TEX-system facilities. The typesetting engine was pdfLATEX. The document class was `toptesi`, by Claudio Beccari, with option `tipotesi=scudo`. This class is available in every up-to-date and complete TEX-system installation.